A Performance Characterization of an Interactive Robot

by

Craig Foster

Submitted to the Department of Mechanical Engineering
in partial fulfillment of the requirements for the degree of

Master of Science in Mechanical Engineering

at the

MASSACHUSETTS INSTITUTE OF TECHNOLOGY

September 1999

Author ....
Department of Mechanical Engineering
August 18, 1999

Certified by ....
Neville Hogan
Professor
Thesis Supervisor

Accepted by ....
Ain Sonin
Chairman, Department Committee on Graduate Students

A Performance Characterization of an Interactive Robot

by

Craig Foster

Submitted to the Department of Mechanical Engineering
on August 18, 1999, in partial fulfillment of the
requirements for the degree of
Master of Science in Mechanical Engineering

Abstract

In this thesis, the impedance limits of a two degree of freedom robot are investigated. As the robot is designed for interactive use with human subjects, stability is of utmost importance. The system is first described and calibrated. Then experiments are performed to determine the range of achieveable endpoint impedance. Finally, the major factors limiting the endpoint impedance are brought to light.

Thesis Supervisor: Neville Hogan
Title: Professor

Acknowledgments

My experiences in the Newman Lab for Biomechanics and Rehabilitation at Massachusetts Intitute of Technology, have left me with a great deal to be thankful for.

I would first like to thank my advisor, Neville Hogan, for his guidance in my research. I am thankful for the opportunity to pursue an education at MIT. Neville has a unique understanding of physical systems and physical sytem interaction which has made him an expert in his field. Igo Krebs also gave valuable input toward my research through his hands-on experience with MANUS (an earlier version of the robot studied in this thesis).

I am also greatful to my wife, Alexandrea, for all her support during our stay here in the Boston area. She has been a great friend, a wonderful wife, and an even better mother. A thanks also goes out to my parents, Robert and Ingrid, as well as the rest of my family for their support.

The friends I have made in the Newman Lab have been great. Justin Won has assisted me in more ways than I can remember. Justin's knowledge of control systems is incredible, and his help using lab resources will not be forgotten. Justin is also a great friend and I enjoyed our times at the Bruins and Red Sox games. Also Lori Humphrey was a great person to have around the lab. Aside from keeping me smiling, she was a great help in finding references for my research. Brandon Rohrer was also a great friend to have around the lab. He helped me on several aspects of my research as well as with the courses we took together. Michel Lemay and Joe Doeringer were a great help to me in getting the software for the robot working. Peter Madden and Luke Sosnowski generously shared their machining knowledge and resources. Aside from being a good hockey player, John Madden was a great friend who would bend over backwards to help out in any way he could. I must not forget to thank Justin Verdirame for that handy m-file for plotting ellipses, and for being my sailing partner. To all the members of the Newman Lab hockey team; Thanks for the great season!

Contents

List of Figures

List of Tables

Chapter 1

Introduction

The goal of this thesis is to determine and understand the impedance limits of the beta prototype MIT-MANUS. MANUS-2, as it has become known, is a robot-aided rehabilitation facility for use with patients who have suffered a stroke. A physical description of MANUS-2 as well as a discussion of how the robot operates are covered in chapter 2. The intention of this chapter is to give the motivation for developing this type of technology as well as to explain the validity of using impedance as a measure of robot performance.

1.1 Motivation

The leading cause of disability in the United States is cerebral vascular accident, more commonly known as stroke. According to the National Stroke Association (NSA), 730,000 Americans suffer a new or recurrent stroke every year. Of these stroke victims, 570,000 survive and require rehabilitation. The estimated annual cost of the care for these survivors is $30 billion [2]. The neurorehabilitation process is labor-intensive, relying on a clinician working with a single patient. Labor-intensive procedures are a primary application field of robotics. Research by Krebs et. al. [13] has shown that robotics and information technology can be used to improve quality, enhance documentation, and increase productivity of rehabilitation. The research by Krebs et.al. has also shown that the excercise provided by the robot does indeed influence the recovery of stroke patients. Furthermore, the use of robots has the potential of decreasing the cost of care by increasing the efficiency of the clinician.

1.2 Impedance as a Performance Measure

MANUS-2 is designed for safe stable interaction with humans. Therefore, the dynamics of the environment that the robot interacts with are unknown. The performance of a robot interacting with an unknown environment is heavily reliant on the controller. Research has shown (Hogan [10]) that impedance control can be used to achieve stable interaction with unknown environments.

1.2.1 Impedance Control

This section is designed to give an overview of impedance control. The information in this section is taken from Hogan's research, and the reader can refer to [10] for a more in-depth understanding of this topic.

The first step in understanding impedance control is to view the point of interaction between the manipulator and its environment as a mechanical interaction port. In general, the interaction point between any two or more physical systems can be viewed as an interaction port. In addition, the power flow between two or more physical systems can always be defined as the product of two conjugate variables, an effort (e.g., a force), and a flow (e.g., a velocity). One should keep in mind that no one system may determine both variables.

Equally important in understanding interaction are the definitions of impedance and admittance. Physical system interaction port behavior may be described as an impedance, which accepts flow (e.g., motion) inputs, and yields effort (e.g., force) outputs, or an admittance which accepts effort (e.g., force) inputs, and yields flow (e.g., motion) outputs. These two representations are interchangeable for linear systems, but in general not interchangeable for nonlinear systems. As manipulation of the environment by the robot is fundamentally nonlinear, these representations should be interchanged only with care. Another point to be made about impedance and admittance is that if one of two phsyical systems on one side of an interaction port is described as an admittance, the other physical system must be described as an impedance and vice versa.

Next, it is important to understand that the environment almost always takes on the form of an admittance as viewed by the manipulator. For all manipulatory tasks that MANUS-2 will encounter, the environment will contain inertias and/or kinematic constraints. These types of environments will accept forces and determine their own motion in response to those forces. Therefore, these environments can properly be viewed as admittances. Thus, the manipulator should assume the behavior of an impedance. Because the mechanical interaction with the environment will change with different tasks, the manipulator should be adaptable. Therefore, the controller should be capable of modulating the impedance of the manipulator as the task changes.

The general strategy for controlling the manipulator is to control its motion and to give it an impedance which is capable of dealing with deviations from that motion. The desired impedance changes depending on the task at hand. Thus the larger the range of achievable impedances, the wider the range of tasks/environments the manipulator may safely and stably interact with.

Although the information presented to this point illustrates that impedance is important for stable interaction between a manipulator and its environment, it does not promote a physical understanding of impedance. Many prefer to think of mechanical impedance as a dynamic generalization of stiffness. This is similar to viewing electrical impedance as a dynamic generalization of resistance.

Finally, the main distinction of impedance control is that it attempts to govern the interactive behavior of a manipulator that is unaffected by contact with other physical systems. Again, consider impedance as a generalized form of stiffness. Stiffness (at the point of interaction) is a property of the manipulator which is independent of contact with the environment. On the other hand, the force at that point is largely dependent on contact with the environment. Therefore, force control (as well as motion control) is sensitive to contact with the environment; impedance control need not be.

1.2.2 An Impedance Control Example

A simple example of an impedance controller can be demonstrated using a single degree of fredom linear actuator. This system can also be viewed as a one degree of freedom manipulator. First, the actuator is assumed to be capable of producing a force F_a. Also, the actuator has inherent mass (m) and inherent damping (b). A model of this actuator is found in figure 1-1a. The simplest form of impedance control which can be implemented is that which uses position feedback alone. This controller consists of the following control law:

$$F_a = k(x_d - x) \tag{1.1}$$

Where x_d is the desired position, x is the actual position, and k is the controller gain. This gain can be viewed as a stiffness for this control law. A block diagram representation of this closed loop system is found in 1-1b.

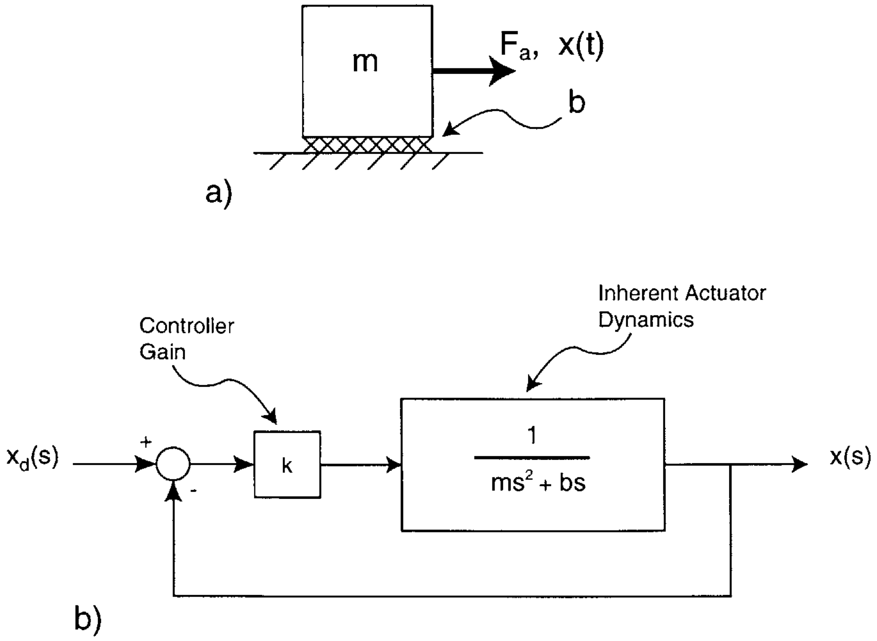

Figure 1-1: a) Model of a 1 degree of freedom manipulator with inherent mass and damping. b) Block Diagram of the same manipulator controlled using an impedance controller with position feedback only.

Assuming that this system can come into contact with another physical system, the force of interaction F_{int} would also be applied directly to the mass m. The mechanical impedance of the closed loop system in the Laplace domain is then defined as $\frac{F_{int}(s)}{v(s)}$. This relation shows that the manipulator accepts velocity v as its input and yeilds force F_{int} as its output. Setting the desired position equal to zero ($x_d = 0$), and using the control law above allows us to solve for the impedance.

$$\frac{F_{int}(s)}{v(s)} = ms + b + \frac{k}{s} \tag{1.2}$$

Equation 1.2, illustrates that the controller gain k shows up explicitly in the impedance of the manipulator allowing for limited modulation of the impedance. If velocity is fed back along with the position, then the controller would be capable of a more complete modulation of the manipulator impedance. One form for the manipulator impedance of this one degree of freedom manipulator with position and velocity feedback is given by the following equation.

$$\frac{F_{int}(s)}{v(s)} = ms + (b + b_c) + \frac{k}{s} \tag{1.3}$$

Where b_c is the controller's velocity gain.

This allows for two of the three impedance terms to be modulated via the controller. Additional schemes, using force feedback to modulate the mass term, have also been succesfully implemented.

It is important to keep in mind, that the environment that the robot interacts with can affect the stability of the system. This idea of coupled stability will be discussed further in chapter 4.

Chapter 2

System Basics

The purpose of this chapter is to give the reader the basic information necessary to understand the robotic system used in this thesis. Each component of the system will be briefly described and the types of signals each component can generate and receive will be discussed. The photograph in figure 2-1 shows the major components of the system. The robot itself is composed of a four-bar-linkage and two actuator/encoder packages. This construction allows for two degree of freedom motion in a plane. Viewing the four-bar-linkage as an arm, the elbow motion is controlled by the upper actuator, and the shoulder motion by lower actuator. This system is nonlinear as the inertia of the four-bar-linkage (realized at the actuators) changes with configuration. This nonlinearity is the most obvious, but others do exist. For example, the position information is recorded using optical encoders that have a finite resolution. This means that changes in endpoint position are recorded as small steps rather than a continuous motion. Later in this thesis, the effect of such nonlinearities on robot performance will be discussed.

The reader can gain a better understanding of how the robot is used by examining figure 2-2. This figure illustrates a typical use of the robot. Through studies conducted by the Newman Lab and Burke Rehabilitation Hospital in White Plains New York, this type of robot has been implemented in the neuro-rehabilitation of patients who have suffered a stroke.

Figure 2-1: Photo of the System

2.1 How the System Works

Figure 2-3 shows a block diagram of the system components and their connections to one another. For simplicity sake, the diagram includes just one of the actuator packages rather than two. This block diagram is a good reference for understanding how the system works. This section is designed to give the reader an overview of the basic operation of the system while the remaining sections of this chapter go into detail about each component of the system.

First, the computer is used as the real-time controller for the robot. Using the computer, many different control laws may be implemented with relative ease. Based on an experimental task and a control law, the computer calculates the desired Cartesian forces. Then, the computer transforms these forces into the actual torque commands to be sent to the actuators. These torque commands leave the computer through a digital to analog (D/A) converter in the form of voltages. The voltages travel to servo amplifiers and are converted into currents. Finally the actuator receives the current and transforms it into mechanical torque. For an open loop system, this is the end of the story, but the concern here is to have a stably controlled closed loop system.

The feedback for this system is in the form of the two actuator angles. Optical encoders allow for the measurement of these angles, and the computer can use this

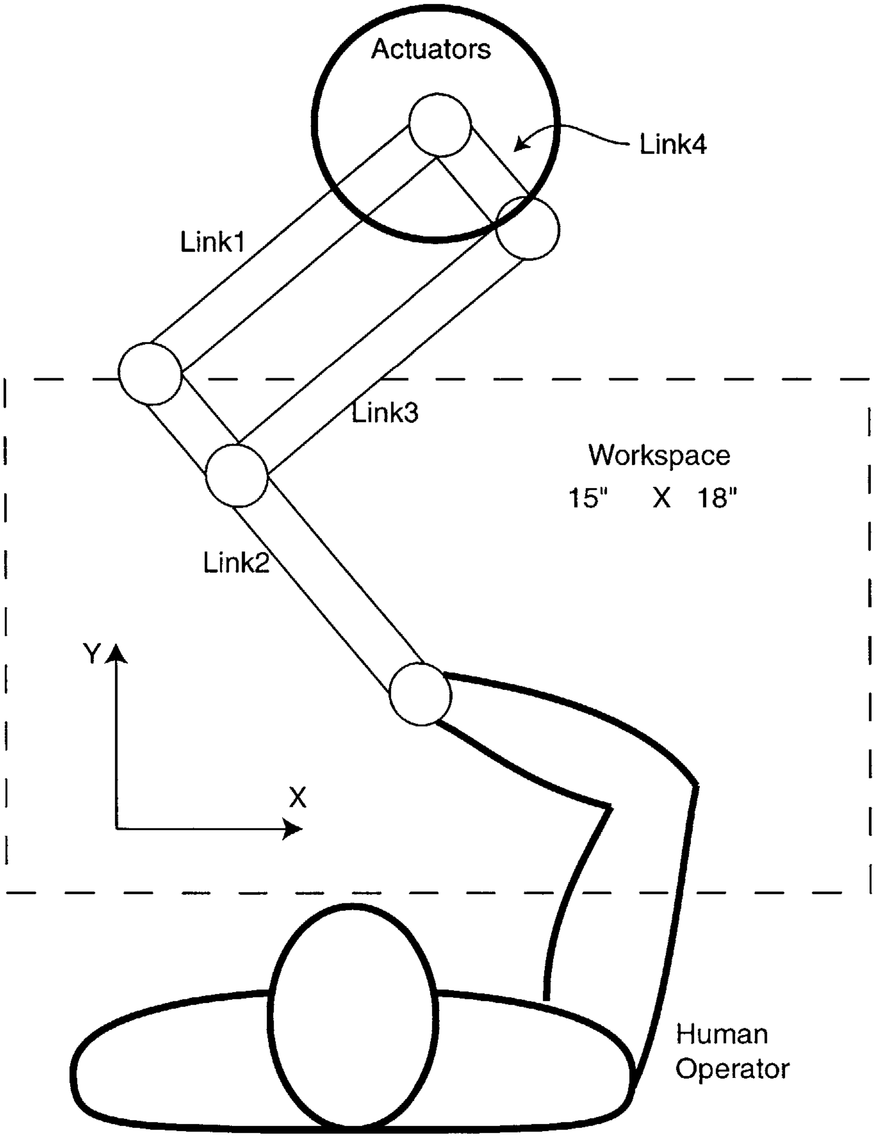

Figure 2-2: Overhead Sketch of the Robot and an Operator Note: drawing not to scale

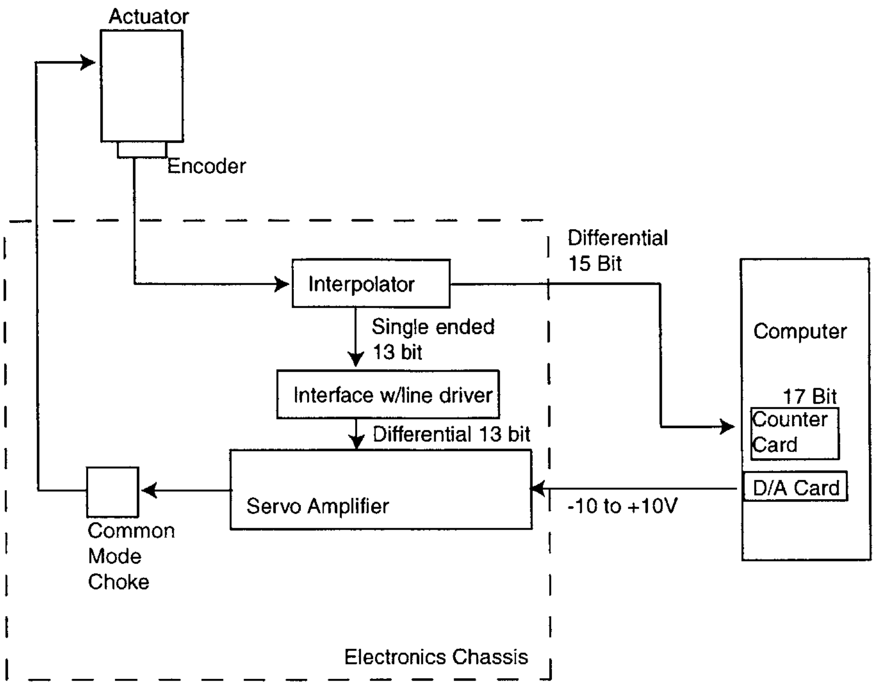

Figure 2-3: Block Diagram of System Components

information to calculate the x-y position of the endpoint of the robot. The endpoint positions are then used by the controller to calculate the desired Cartesian forces thus closing the loop.

2.2 Computer

The computer being used is equipped with a Pentium II 200 MHz processor and 128 Mbytes of RAM. QNX version 4.24 is installed as the real-time operating system, and C++ is the programming language used in the control software.

2.2.1 Input/Output

A ComputerBoards CIO-DAS1602/16 input/output board is installed in the computer. Although the board is capable of digital input/output (DIO), analog to digital (A/D) and digital to analog (D/A), only the D/A feature is used in this application. The D/A converter on this board is setup for output of -10 to +10 volts, and has a resolution of 12 bits.

2.2.2 Counter Card

The USDigital PC7266 PC to Incremental Encoder Interface Card was chosen to record information from the encoders. The card is capable of increasing the resolution of the input signal by a factor of four. This results in a final resolution of 131072 cycles/revolution (17bit). The resolution will be addresed again in the section titled Encoders and Interpolators.

2.3 Amplifiers

Figure 2-3 shows the output of the D/A card leading to a servo amplifier. This block actually represents a servo amplifier along with its power supply. The Kollmorgen PA08 power supply is used to supply the Kollmorgen SE06 Servo Amplifier. The SE06 is a three phase pulse width modulation (PWM) amplifier designed for use with three phase brushless motors. The amplifier uses position information from the encoder in the actuator package to ensure proper commutation. The amplifier is capable of taking in voltage signals from the D/A card and converting them into corresponding current signals to be applied to the actuator.

2.4 Common Mode Choke

A common mode choke was used to suppress noise from the pulse width modulation in the amplifiers. The noise was corrupting position information and its magnitude was attenuated using this choke. This choke is designed to create a large electrical impedance to any signals that are common on all three phases of the amplifiers output while imposing very low impedance to the intended three phase signal. This is possible because the noise is at the same frequency and phase angle on all three lines, and the intended three phase signals are at phase angles of 120° relative to one another. The noise problem and the common mode choke are covered in more detail in Appendix A of this thesis.

2.5 Actuators

The actuators used in this system are Kollmorgen RBE 03013-C brushless three-phase DC motors. These motors have linear torque constants on the order of 3.7 $\frac{\mathrm{Nm}}{\mathrm{amp}}$ as will be seen in more detail in the Characterization and Calibration chapter of this thesis.

2.6 Encoders and Interpolators

Each actuator is outfitted with an optical encoder (Gurley Precision Instruments: 8235H-8192-CBQC-1000E). The output of the encoder leads to an interpolator (Gurley Precision Instruments: HR2-4WC-BRD-PF). These encoder and interpolator packages are shipped from Gurley Precision Instruments as a matched and calibrated pair. The normal output from the encoder is 8192 cycles per revolution. The interpolator is used to create signals at 4 times this resolution to give 32768 cyles/rev (15 bit). Unfortunately, the amplifier can accept no higher than 25000 cycles/rev for its commutation feedback loop. Therefore, the interpolators were custom built with extra outputs at 8192 cycles/rev. These extra signals were fed to the amplifiers via an interface card which is explained in the next section.

The 15 bit signal which leaves the interpolator travels to the counter card in the computer. The counter card then uses its own quadrature interpolation scheme to increase the resolution by a factor of 4. Thus the final resolution used in the feedback loop is 17 bit or 131072 $\frac{counts}{rev}$.

2.7 Interface Card

Due to a limitation on the number of available connections on the interpolator, the lower resolution signals were output as single ended rather than differential signals. The single ended signals needed to be converted to differential using a line driver. This conversion is the basic function of the interface card, it takes the 13 bit single ended signals from the interpolator, turns them into 13 bit differential signals and sends them to the amplifier.

This concludes the description and function of the individual components of the system. The remainder of the thesis will focus on the characterization of the performance of the robot.

Chapter 3

Characterization and Calibration

This chapter is devoted to the characterization of the system. The amplifiers and actuators are the major components of the system which require calibration and characterization. Although the position sensors themselves do not require calibration, the geometry of the robot requires that the 2 degree of freedom (d.o.f.) position measurements be calibrated.

Once the amplifiers, the actuators, and the 2 d.o.f. position were characterized, a system identification (ID) was performed to obtain estimates of the physical parameters of the manipulator linkage.

3.1 Data Acquisition Calibration

The first step taken in the calibration procedure was to check the operation of the data acquisition board in the computer. Two functions of this board were tested; digital to analog (D/A), and analog to digital (A/D). The purpose of these tests was twofold. The first objective was to calibrate the voltages being measured and output by the card. The second objective was to understand the sequence in which the output and measurement events took place relative to one another.

A digital multi-meter was used to adjust the dc offset of the cards input and output channels to 0 ± 5 mV. Then full-scale voltages were checked for all channels. The results showed that all channels were within 5 mV of their set point (± 10V) at full scale.

Next, a simple experiment was completed to verify the proper sequencing of input and output signals from the card. The data acquisition software was written in the following chronological order: First, read the data, then compute the desired output, and finally, output the desired voltage. For the calibration tests in this chapter, the system was operated open loop (i.e. the output is not based on what is being read). This means that the input in response to a given output was actually recorded one time step after the output. An example will better illustrate this idea. Assume the sampling rate is 1000 Hz. Now assume the predetermined output voltage to be applied to the system is 2.0 Volts and is to occur at $t = 1.000sec$. Therefore at $t = 1.000$, the output will step from 0 to 2.0 Volts. Recall that the output is the final event in the data acquisition sequence. Thus the response of the system to the step change can not be recorded until the next time step ($t = 1.001$). The sampling sequence was verified through a very simple experiment. One of the output (D/A) channels was connected directly to one of the input (A/D) channels and this same test involving a step of 2.0 Volts at $t = 1.000$ was completed. Figure 3-1 shows that the data acquisition process is indeed functioning as expected.

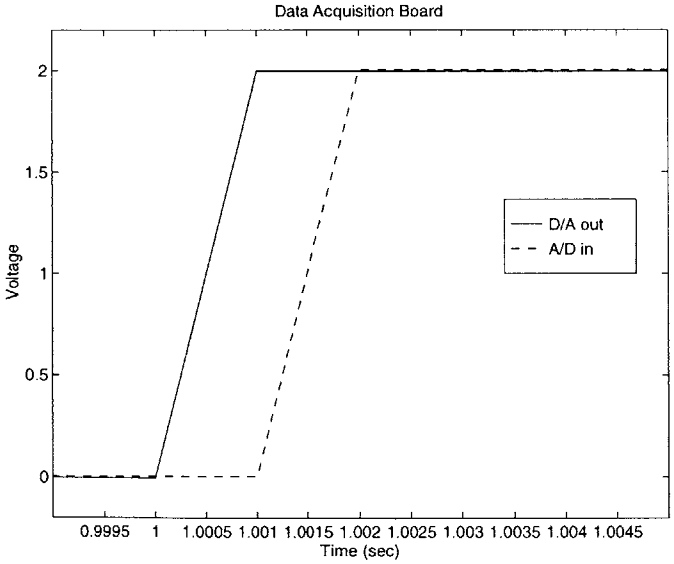

Figure 3-1: Data Acquisition sequence: This plot shows that there is a one sample difference between the output of the D/A and the input of the A/D.

3.2 Amplifier Characterization

The amplifiers, as mentioned earlier, are three phase servo amplifiers. These units receive voltages and output current proportionally. The constant of proportionality from voltage to current is configurable using software. The constant has been set to $0.6\ \frac{amps}{Volt}$. Although this value was not verified directly, any discrepancy in its value has been accounted for in the actuator torque calibration.

The frequency response of the amplifier was also characterized. Because the amplifiers are three phase, a custom three phase current sensor was designed and fabricated. The current sensor is an analog device, and its output was sampled by an A/D card in the computer.

The output from the current sensor was the output signal for this experiment. The input was the command voltage coming from the computer's D/A card. This input was set as a sine wave with amplitude 2 volts which corresponds to 1.8 amps. The frequency of the wave was swept from 2 to 50 Hz. The data in this experiment was recorded at a frequency of 1000 Hz. Figures 3-2 and 3-3 are Bode plots summarizing the results of this experiment. Note that the amplitudes of these plots have been scaled. This is because the measured current signal was that of a single phase of the amplifiers output. The single phase measurement was used because only one out of the three individual phase signals is guaranteed to be in phase with the command signal. The magnitude of any one phase signal is dependent on position, and therefore its actual amplitude has little meaning. However, the relative change in its amplitude compared to that of the command signal as the frequency is swept gives a very accurate measure of the amplifiers frequency response.

In examining figures 3-2 and 3-3 there is a rapid decrease in phase with an increase in frequency. At the same time, there is no apparent decrease in amplitude. This is strong evidence of a pure time delay. To verify that the phenomenon being observed in these plots was indeed a pure delay, plots of phase versus frequency on a linear scale were created. Pure delay follows equation 3.1 which is a straight line on a linear plot.

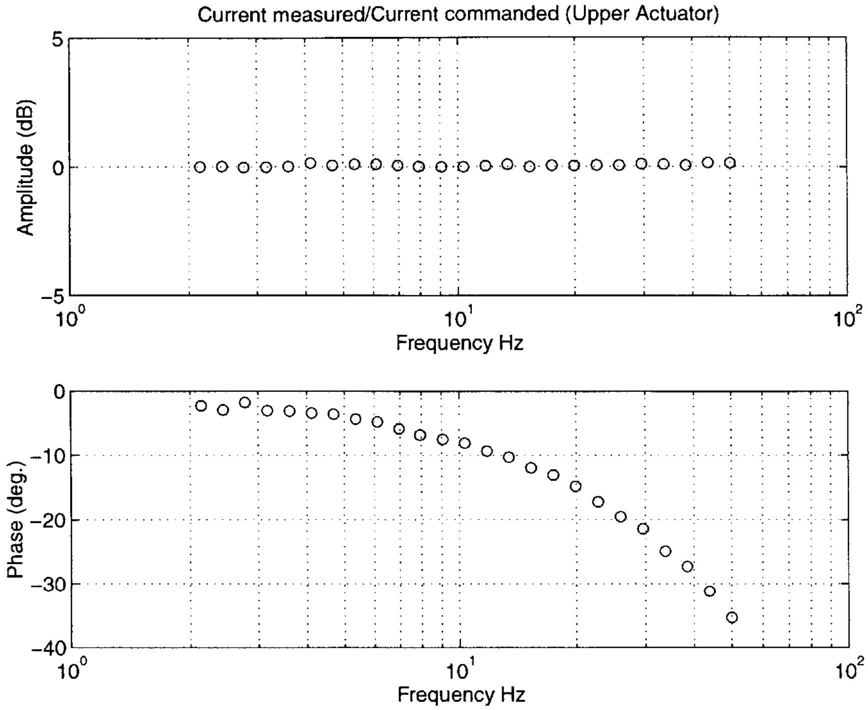

Figure 3-2: Bode plot of the upper amplifier frequency response; Actual current level: 1.8 amps; Amplitude scaled to 0 dB at 2 Hz

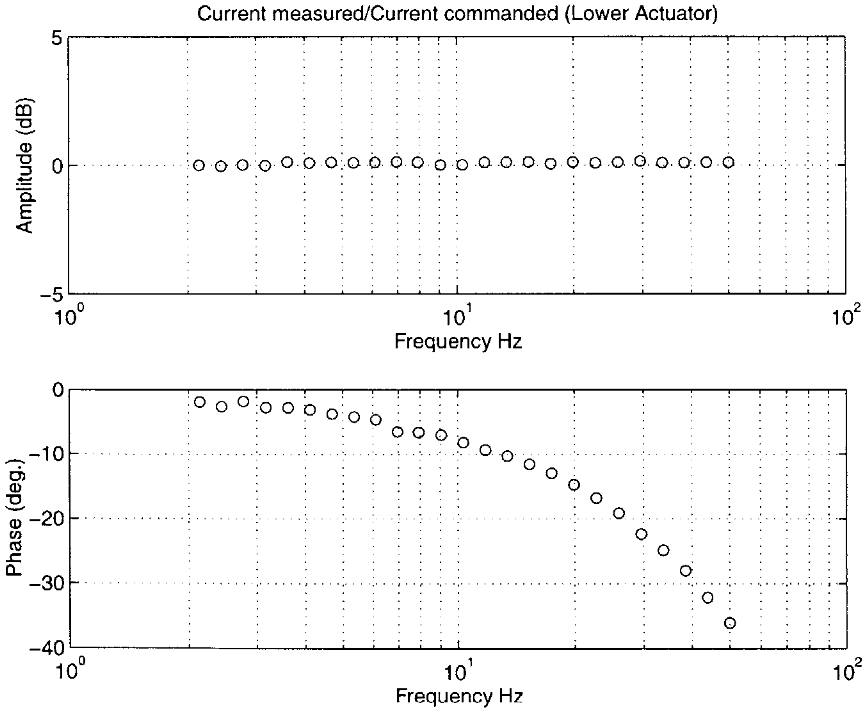

Figure 3-3: Bode plot of the lower amplifier frequency response; Actual current level: 1.8 amps; Amplitude scaled to 0 dB at 2 Hz

$$\phi = T\omega \tag{3.1}$$

Where ϕ is the phase lag, T is the time delay and ω is the frequency.

Figures 3-4 and 3-5 illustrate that the phase lag in the amplifiers can be characterized as a pure time delay. In these figures the frequency is in $\frac{rad}{sec}$ and the angle is in rad, thus the slope of the line is in seconds. This is convenient as the slope of the line is the time delay as noted in equation 3.1. Due to the order in which the data is sampled, there is a one sample difference between the input and output signals as they are recorded. This means that 1 $msec$ of delay can be accounted for by the sampling order, and the additional 1 $msec$ is attributed to a pure time delay in the amplifier.

The solid lines in figures 3-4 and 3-5 are not the best fit lines to the data pictured. The best fit lines have slightly larger bias and better correlation coefficients. The lines in the figures were determined by weighting the desired DC bias of zero with artificial data points. The best fit line was then drawn in, and the correlation coefficient was determined by checking the fit of all real data points to this new line.

3.3 Actuator Characterization and Calibration

The following three sections are focused on characterizing the actuators used in this system. First, a static torque calibration was completed, and then a torque frequency response. Finally, a position frequency response was determined. Note that because the actuator is controlled via the amplifier, the amplifier is involved in the following characterization of the actuators.

3.3.1 Static Torque Calibration

One important bit of information for any motor is its torque constant K_T. In this calibration, the K_T's will be determined in metric units $(\frac{Nm}{amp})$.

The device used to measure torques for this experiment was the ATI Gamma

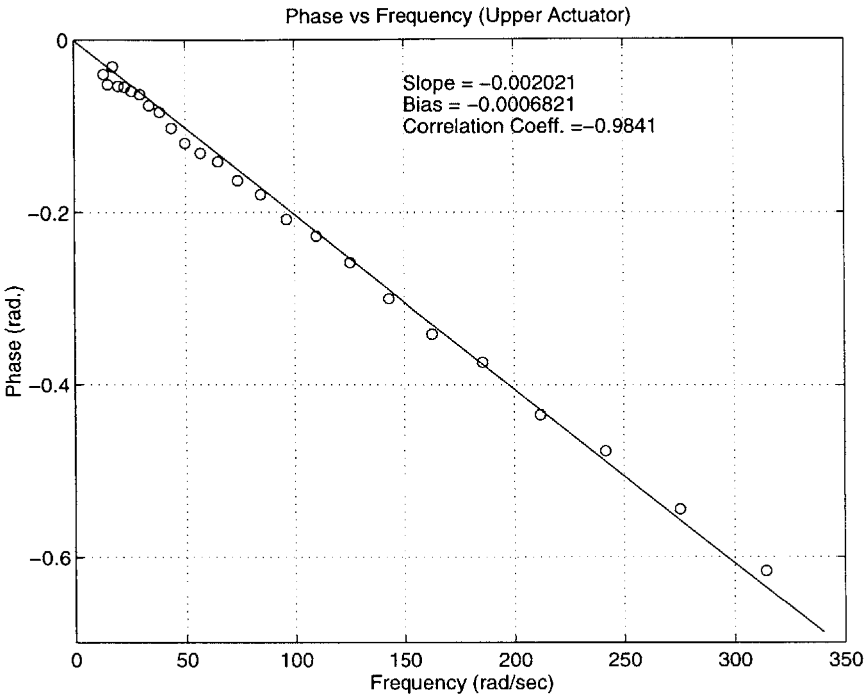

Figure 3-4: Linear phase lag versus frequency for the upper amplifier: This plot demonstrates that the phase lag is created by a pure time delay

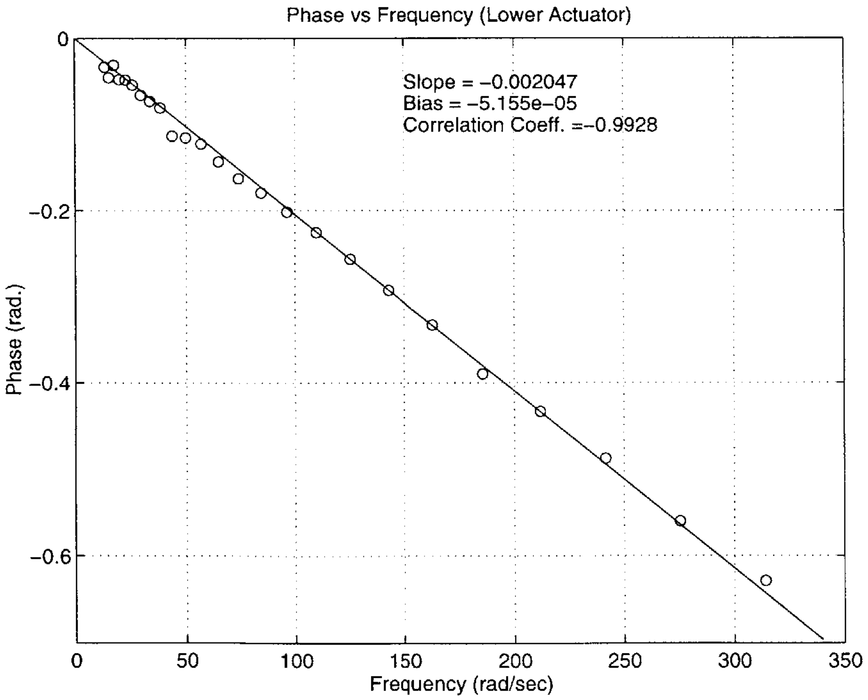

Figure 3-5: Linear phase lag versus frequency for the lower amplifier: This plot demonstrates that the phase lag is created by a pure time delay

six axis force transducer. The calibration for this transducer can be found in the appendix of this thesis.

These tests were actually performed in a quasi static manner. This is to say that the current was being applied to the actuator in a continuously varying manner at a low frequency. In this case, the low frequency was 2.42 Hz for the lower actuator and 0.4 Hz for the upper actuator. The data for the lower actuator was taken first and a problem was noticed, thus the frequency was lowered for the test on the upper actuator. This problem arose from the test being quasi static, and is more appropriately addressed in the section where the data is presented. The data for this test was also sampled at 1000Hz.

Figures 3-6 and 3-7 show the data taken for this experiment. The reader should note some oddities within these plots. First, the data forms an ellipse rather than the expected straight line. This is due to the fact that the two signals being plotted are sine waves at slightly different phase angles. From the amplifier characterization, it is known that there exists 2 *msec* of delay between the input signal and the output signal during the sampling. This 2 *msec* delay does create some phase difference at the frequencies of 2.42Hz and 0.4Hz; 0.030 *rad* and 0.005 *rad* respectively. These differences are not large enough to account for the magnitude of the minor axes of the ellipses in these plots. In fact the magnitudes of the minor axes of the ellipses (including the 2 *msec* delay) correspond to 0.072*rad* and 0.043 *rad* respectively for the lower and upper actuators. The remainder of the phase difference comes from an offset in phase angle which does not vary with frequency. The magnitude of this offset angle has been estimated at 0.04 *rad* using the frequency response information presented in the next section. When this offset is added to the phase differences resulting from delay, the total amounts of phase difference are 0.070 *rad* for the lower actuator and 0.045 *rad* for the upper actuator. These total phase differences correspond well with what was actually observed during the experiment (0.072 and 0.043 *rad*). Because each of the ellipses are symmetric about their major axis, and the phase differences are small, these phase difference cause no observable distortion of the measured K_Ts.

The offset in phase was an artifact of the setup of the force transducer software and has since been corrected. Appendix B provides evidence that there is no time offset between the input force and the ATI transducer's response. The offset phase angle will be more clearly illustrated in the next section where the frequency responses of the actuators are presented.

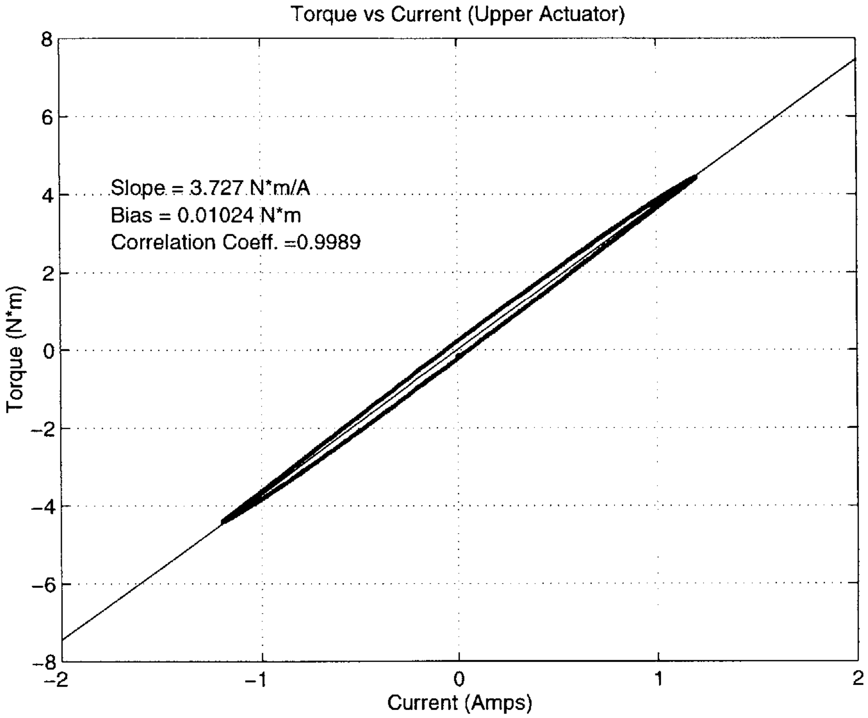

Figure 3-6: The slope of this line is the K_T for the upper actuator

3.3.2 Torque Frequency Response

A second experiment was conducted with the commanded current as the input and the torque measured at the actuator as the output. This experiment was set up in much the same way as the frequency response experiment for the amplifiers. Again, the torque was measured using the ATI Gamma force transducer. The frequency was swept from 2 to 50 Hz, and data was sampled at 1000Hz.

The results of this characterization experiment can be viewed in figures 3-8 and 3-9. Again there is evidence of a pure delay, but this time it is expected. The amplifiers are used to send the current commands to the actuators, and therefore any delay in

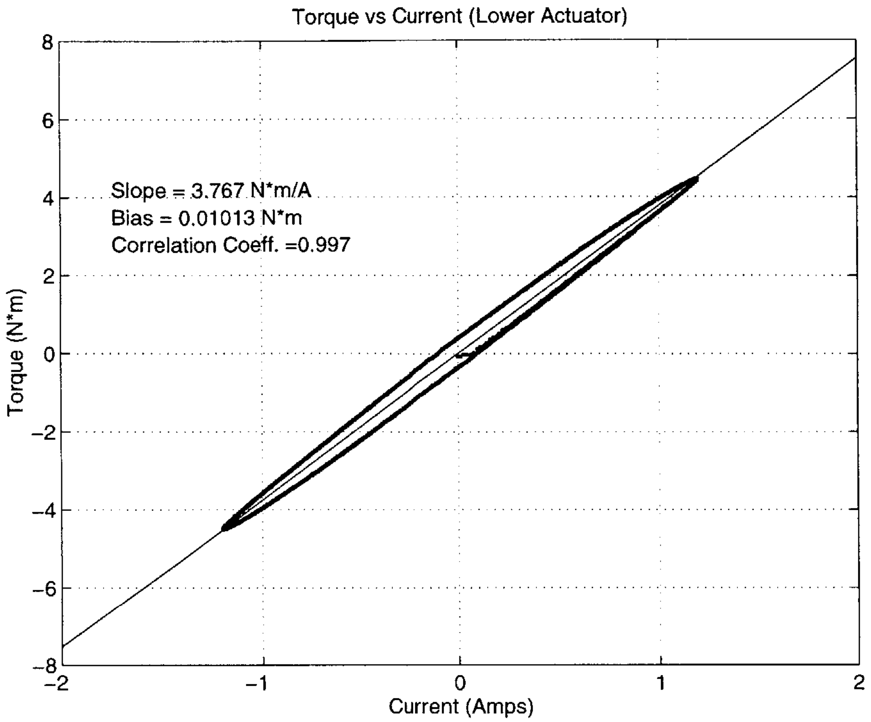

Figure 3-7: The slope of this line is the K_T for the lower actuator

the amplifiers will show up in this experiment as well. To verify that the pure delay is still 2 *msec*, the same technique used in the case of the amplifiers was employed again. Refer to equation 3.1 and to figures 3-10 and 3-11 to see that the 2 *msec* delay is verified. Again, note that 1 *msec* of delay is attributed to the sampling order used in the experiment, and the other 1 *msec* is a pure delay exhibited by the amplifier.

As mentioned before, the lines in these linear phase versus frequency plots have non-zero intercepts. This offset in phase is more clear in these plots than the elliptical plots of figures 3-6 and 3-7. Again, this offset was due to an error in software setup for the force transducer and has been corrected.

3.3.3 Position Frequency Response

For a complete characterization of the actuator packages, a frequency response using commanded current as the input and position as the output was completed. This experiment was performed in a similar manner to the torque frequency response test. The major difference was that the rotor of the actuator was free to move in this

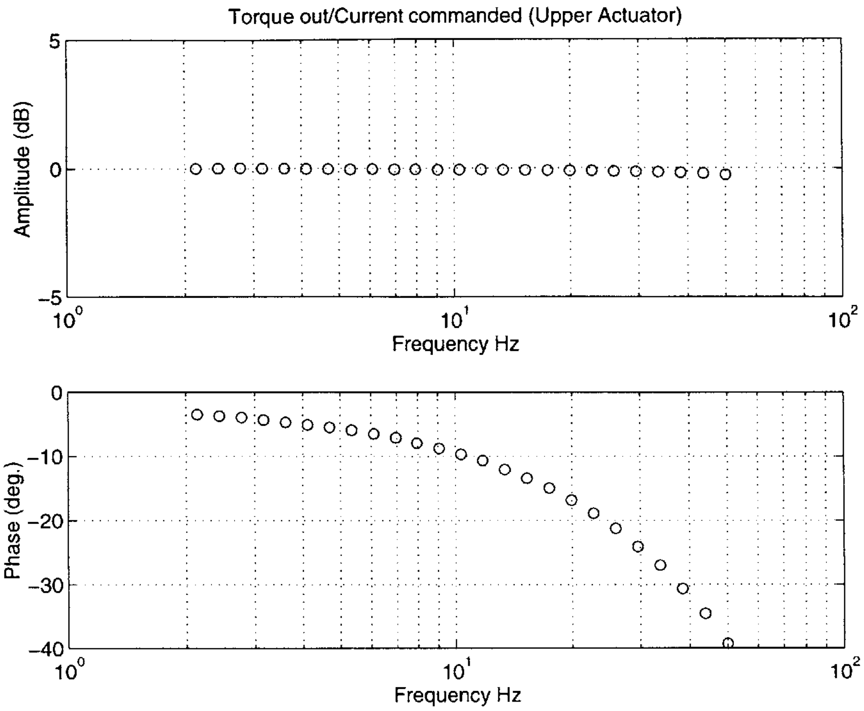

Figure 3-8: Upper actuator frequency response; Actual current level: 1.8 amps; Actual torque level: 6.71 Nm; Amplitude scaled to 0 dB at 2 Hz for easy comparison to amplifier frequency response

experiment rather than being tied to ground through the force transducer as in the last experiment. Of course this means that the output is no longer force, but rather position. Another difference is that the frequency was swept from 2 to 100 Hz rather than 2 to 50 Hz like the previous experiments. The reason for this change becomes evident when the data is presented.

Viewing figures 3-12 and 3-13 allows the reader to become familiar with the frequency response of the actuators using position as the output signal. These plots show more interesting behavior than any of the frequency response plots presented to this point. This behavior is to be expected as the actuator exhibits the dynamic behavior of a mass being driven by a torque source. In addition, the actuator has some friction and damping that must be accounted for.

As demonstrated by the torque frequency response, there is a 2 *msec* delay which should be present on top of any dynamics that the actuator itself exhibits. This is evident when looking at figures 3-12 and 3-13. From the magnitude plots, the corner

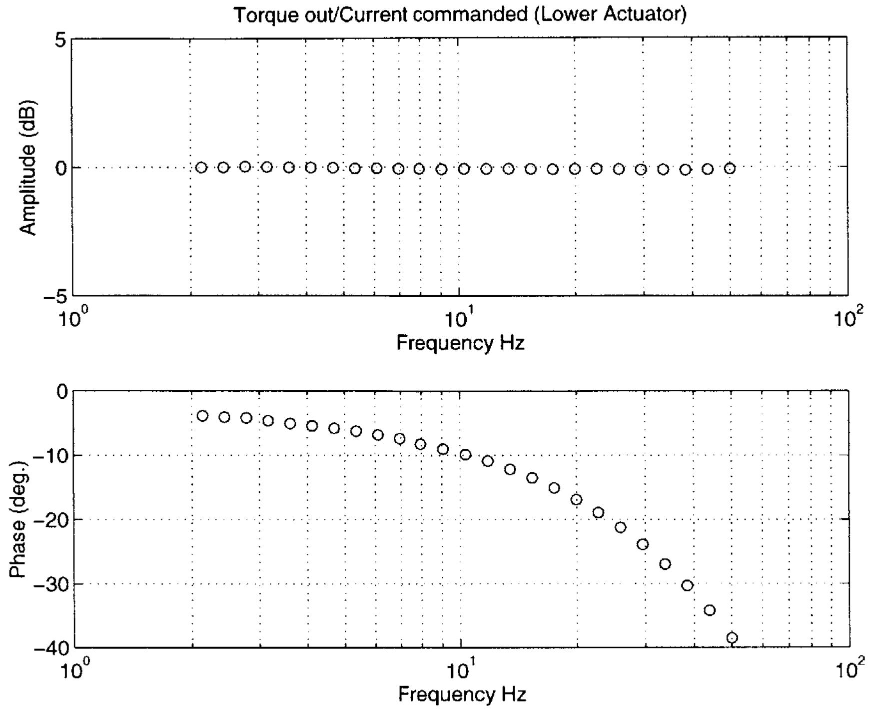

Figure 3-9: Lower actuator frequency response Actual current level: 1.8 amps; Actual torque level: 6.78 Nm; Amplitude scaled to 0 dB at 2 Hz for easy comparison to amplifier frequency response

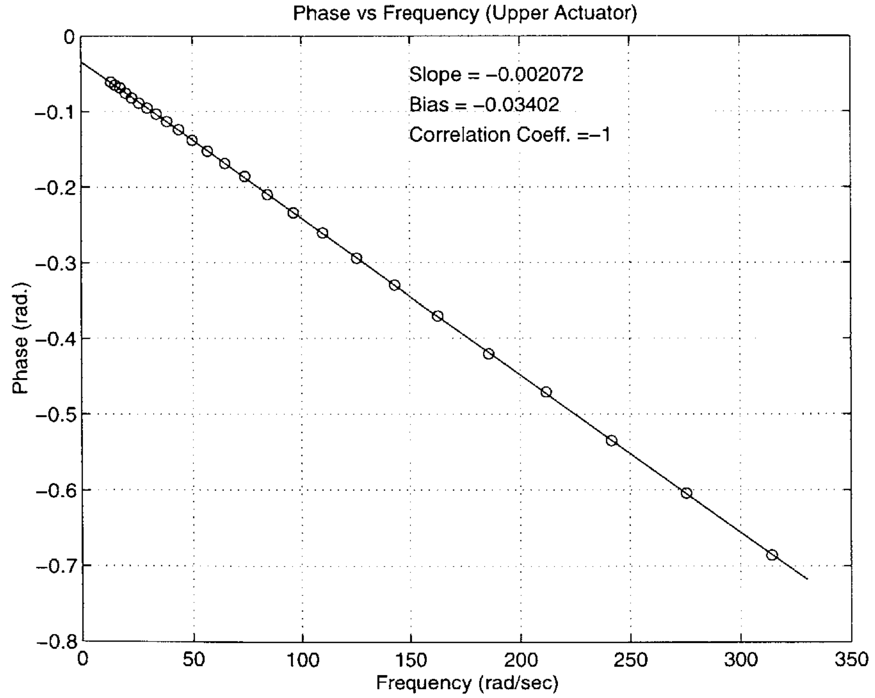

Figure 3-10: Linear phase versus frequency of the upper actuator torque response; The slope of this line is the delay in seconds.

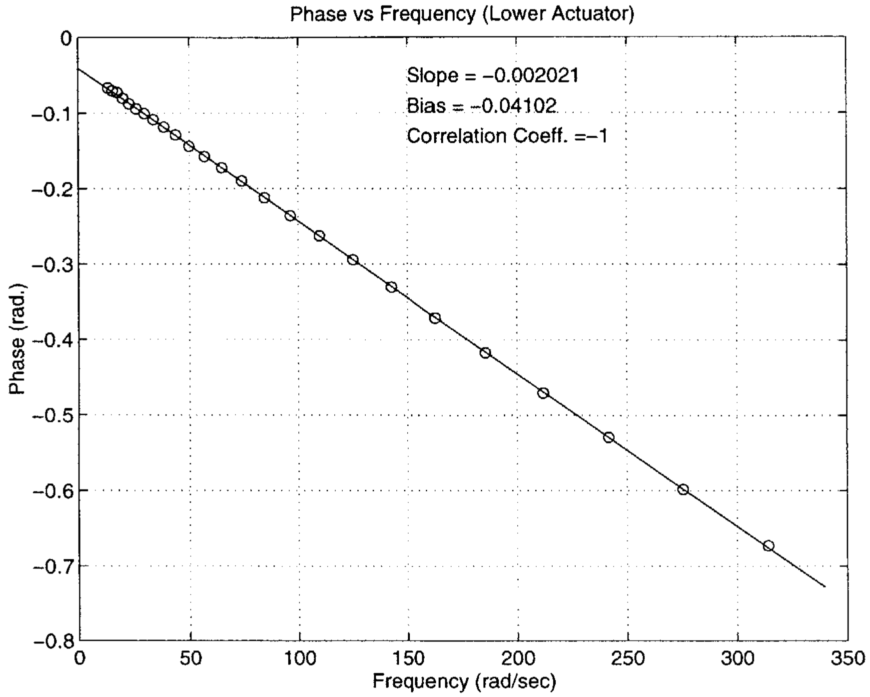

Figure 3-11: Linear phase versus frequency of the lower actuator torque response; The slope of this line is the delay in seconds

frequency of the actuator is observed to be less than 5 Hz. The data at more than one decade above 5Hz (50 - 100 Hz) should ideally show no phase lag due to dynamics of the actuator. Thus the delay must account for any additional phase lag above the 50 Hz point.

When viewing the phase in the 50 to 100 Hz region, a definite decrease in phase with increasing frequency is observed. Again, this is expected because of the known 2 *msec* delay. This delay can again be verified using a similar technique to that described in previous sections. In this case, care must be taken to avoid the section of data where the actuator dynamics are creating phase lag. Therefore, just the last five points (50 to 100 Hz) will be plotted on a linear phase vs. frequency plot. These linear phase plots for each actuator are found in figures 3-14 and 3-15. Note the bias of -3.142 in both of these plots; this is the expected value of the DC bias. From the amplitude plot, a -40 dB/decade slope is observed from 5 Hz through 100 Hz. From this information, the phase plot should be expected to asymptote to $-180°$ or $-\pi$ *rad*. The fact that the phase does not asymptote to $-\pi$ is due to the time

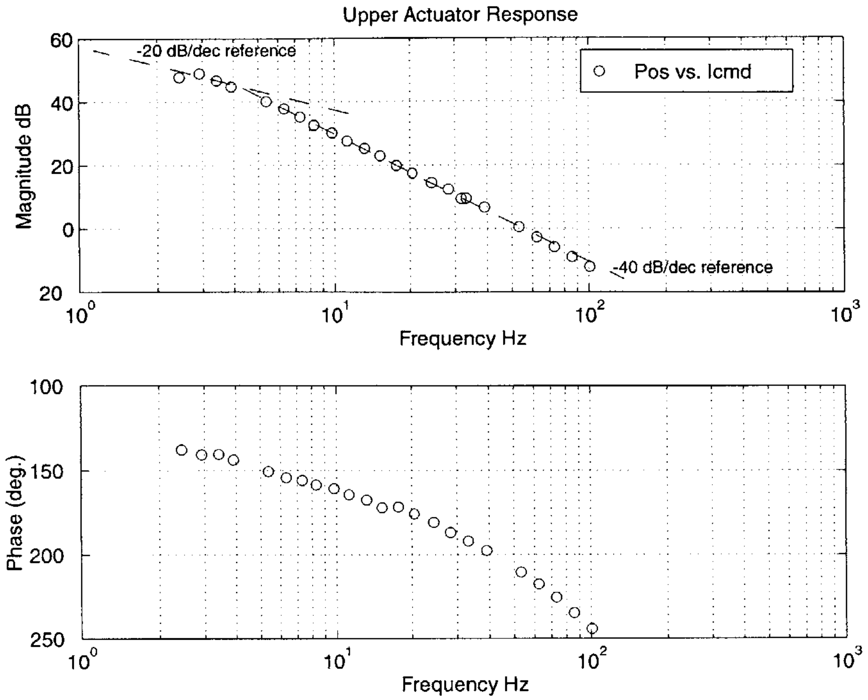

Figure 3-12: Bode plot of the upper actuator frequency response with position as the output

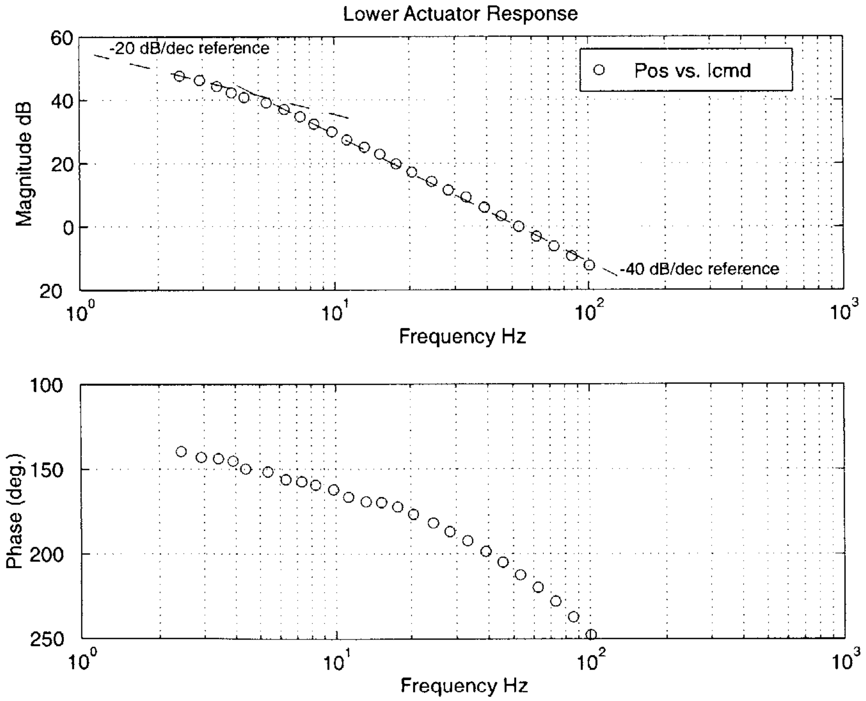

Figure 3-13: Bode plot of the lower actuator frequency response with position as the output

delay in the system. Thus the best fit lines on a linear plot of phase versus frequency should have a slope corresponding to the delay, and a bias of $-\pi$ *rad*. In this case, the best fit lines did not pass exactly through this point, so the lines were forced through the intercept of $-\pi$ using the weighting technique described in section 3.2. The correlation coefficients of the actual data to these forced lines were then checked, and the results are reported in figures 3-14 and 3-15 . The correlation is above 0.98 which for this experiment is considered satisfactory. On the other hand, the slope of the forced lines indicates a delay on the order of 1.8 *msec* rather than 2.0 *msec*. By forcing the line to have the proper intercept, the slope was changed by about 10%. With more care in data collection and more refined processing, this 10% could be reduced.

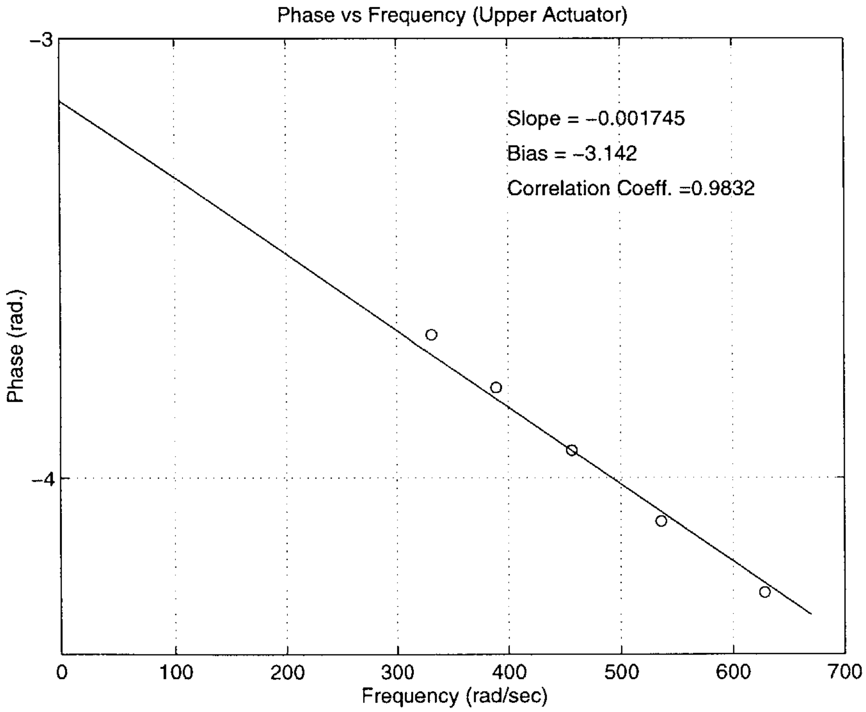

Figure 3-14: Linear phase versus frequency for the position response of the upper actuator; The slope of this plot is the time delay in seconds

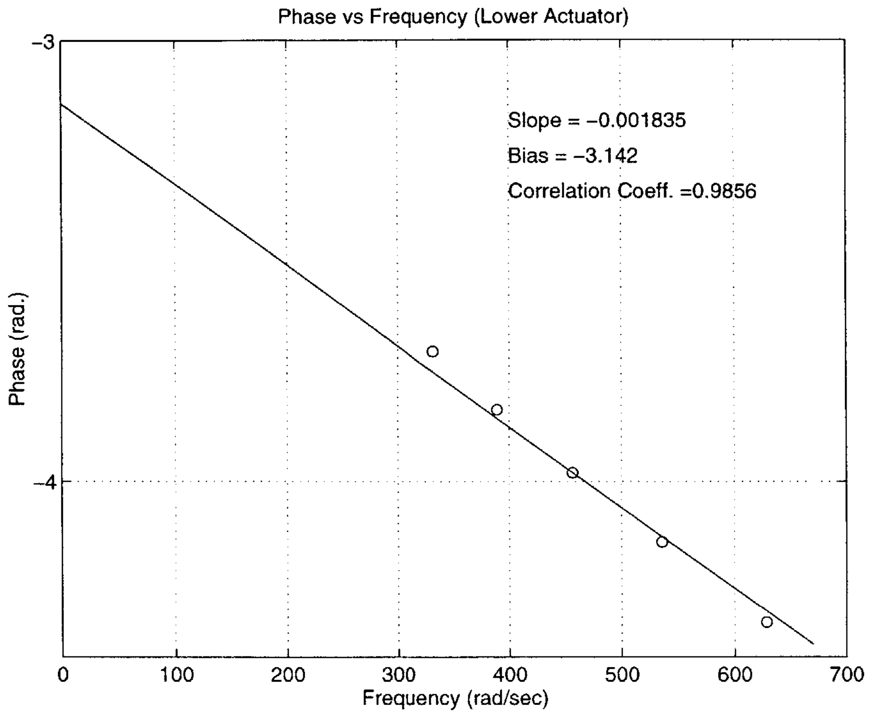

Figure 3-15: Linear phase versus frequency for the position response of the lower actuator; The slope of this line is the time delay in seconds

3.4 Two Degree of Freedom Position Calibration

Although the high resolution optical encoders used in this design required no calibration, the geometry of the system required that a two degree of freedom position calibration be completed. The object of this experiment was to determine the actual lengths of links 1 and 2. Figure 2-2 illustrates the dimensions of the robot which are in question for this experiment.

This calibration was completed with the use of an aluminum plate with a grid of holes drilled through it. This grid of holes was created on a CNC mill and the distance between centers of the holes is 1.000 inch and the distance between any two holes on the plate is known within ± 0.005 inches. The end effector of the robot was outfitted with a pointer which fit into the holes. This pointer fit into the holes with no more than ± 0.004 inches of play.

An array of 28 holes was selected in the area of the workspace. This array of holes is represented by the small circles in figure 3-16. The distance between any two of these holes is known because of the precise layout of the grid. Next, the end point of the robot was moved to each hole and the joint angles were recorded for each position. Because the pointer does not fit exactly into the holes, the distance between any two pointer positions is known only to within 0.013 inches (this the tolerance between centers plus two times the clearance between the pointer and the hole). Using the the known distances, and the measured angles, an unconstrained optimization was used to solve for the two link lengths.

The results of this experiment are summarized in figure 3-16. The circles on the plot represent the holes in the plate (the actual location), and the x's represent the position measured by the robot. The two link lengths are $405.33mm$ and $487.93mm$ respectively. These results demonstrate that the relative distance as measured by the robot is known to within 0.015 inches. Recall that the total error in the calibration fixturing is 0.013 inches. Thus with a more carefully designed calibration setup, the accuracy of the robot could be shown to be much better.

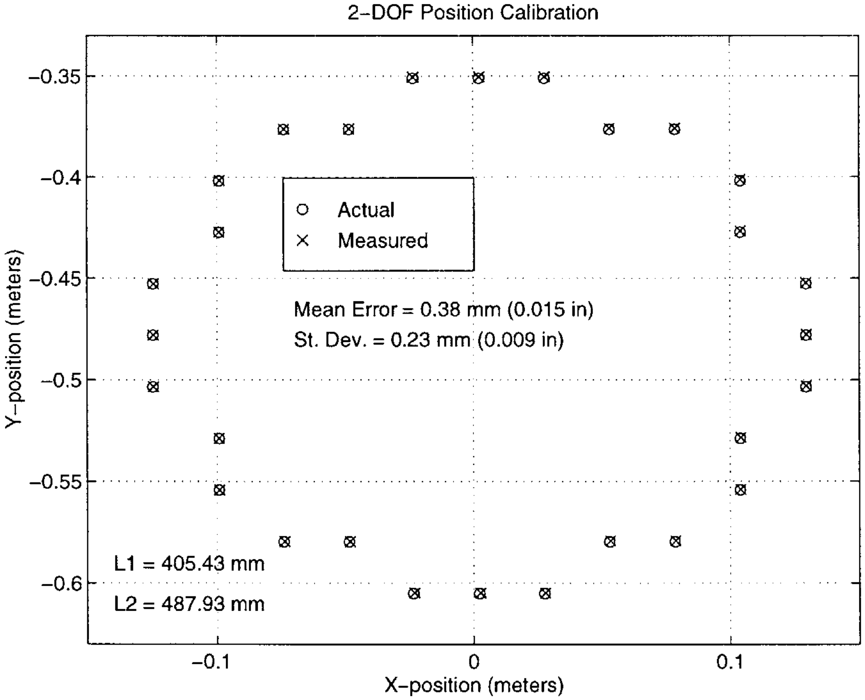

Figure 3-16: This plot summarizes the 2 DOF position calibration

3.5 System Identification

A simple procedure described by Won [19] was used to characterize the physical parameters of the two-link manipulandum. First, a basic modeling assumption is made that treats the four bar linkage as a simple two bar linkage as seen in figure 3-17. It is also assumed that the losses in the joints of the robot can be accounted for by a combination of coulomb and viscous friction. Measuring joint angles q_1 and q_2 with respect to the base frame leads to the following set of equations.

$$\tau_1 = H_{11}\ddot{q}_1 + H_{12}\ddot{q}_2 + \frac{\partial H_{12}}{\partial q_2}\dot{q}_2^2 + b_1\dot{q}_1 + F_{f_1}\mathrm{sgn}(\dot{q}_1) \tag{3.2}$$

$$\tau_2 = H_{12}\ddot{q}_1 + H_{22}\ddot{q}_2 + \frac{\partial H_{12}}{\partial q_1}\dot{q}_1^2 + b_2\dot{q}_2 + F_{f_2}\mathrm{sgn}(\dot{q}_2) \tag{3.3}$$

The H_{ij} are the terms in the symmetric positive definite manipulator inertia tensor given by the following.

$$H(\vec{q}) = \begin{bmatrix} H_{11} & H_{12} \\ H_{12} & H_{22} \end{bmatrix} = \begin{bmatrix} m_1c_1^2 + I_1 + m_2l_1^2 & m_2l_1\cos(q_2 - q_1) \\ m_2l_1\cos(q_2 - q_1) & m_2c_2^2 + I_2 \end{bmatrix} \tag{3.4}$$

where m_i indicates the mass of a link, c_i indicates the distance from the joint to the center of mass of the link, and I_i indicates the inertia of the actuator rotor.

The purpose of this section is to get estimates of the values of the H_{ij}, the b_i and the F_{f_i}.

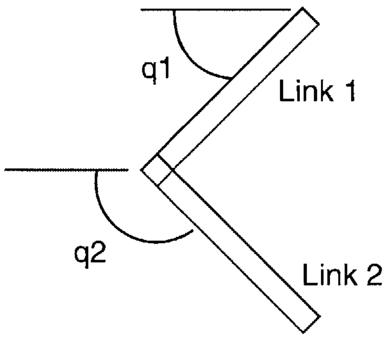

Figure 3-17: Modeling assumption: Treat the four-bar linkage as a simple two-bar linkage.

3.5.1 The Experimental Setup

The experiment was broken down into three parts. Each part consisted of a sub-experiment in which one of the degrees of freedom was eliminated resulting in a single equation of motion. In each case, the robot was configured to act like a simple harmonic oscillator. This was accomplished by using the actuators as virtual springs. The control law of equation 3.5 allows for the actuator to act like a torsional spring where the stiffness is K (Nm/rad). For all the experiments, $K = 10\frac{Nm}{rad}$ was used as the stiffness.

$$\tau = K(q_d - q) \tag{3.5}$$

where q_d is the equilibrium.

3.5.2 Locking the Elbow Joint

By locking the elbow joint in the absolute frame, an equation of motion involving only q_1 is obtained.

$$\tau_1 = H_{11}\ddot{q}_1 + b_1\dot{q}_1 + F_{f_1}\mathrm{sgn}(\dot{q}_1) \tag{3.6}$$

With the elbow locked, the simple control law of equation 3.5 was implemented on the shoulder joint resulting in the following equation of motion.

$$H_{11}\ddot{q}_1 + b_1\dot{q}_1 + F_{f_1}\mathrm{sgn}(\dot{q}_1) + Kq_1 = Kq_d \tag{3.7}$$

The shoulder was then displaced from its equilibrium position and released. The oscillations were recorded and a simulation completed to find the best estimates of H_{11}, b_1, and F_{f_1}. The data and the simulation are shown in figure 3-18, and the best fit parameters are listed below. Note that the data and the simulation differ at low displacement as well as a slight offset in equilibrium. This may be due to the fact that stiction has not been included in the model.

$$
\begin{aligned}
H_{11} &= 0.349 \quad \text{kg-m}^2 \\
b_1 &= 0.222 \quad \frac{\text{Nm}}{\frac{\text{rad}}{\text{sec}}} \\
F_{f_1} &= 0.099 \quad \text{Nm}
\end{aligned}
$$

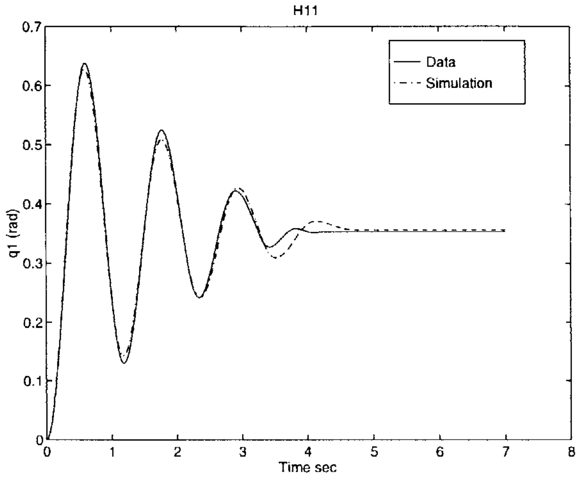

Figure 3-18: This simulation gave the following estimates: $H_{11} = 0.349$ (kg-m^2), $b_1 = 0.222 \frac{\text{Nm}}{\frac{\text{rad}}{\text{sec}}}$ and $F_{f_1} = 0.099$ (Nm).

3.5.3 Locking the Shoulder Joint

Similar to locking the elbow joint, locking the shoulder joint in the absolute frame results in the following equation of motion. This equation describes the motion of link 2 when link 1 is locked in the absolute frame..

$$H_{22}\ddot{q}_2 + b_2\dot{q}_2 + F_{f_2}\text{sgn}(\dot{q}_2) + Kq_2 = Kq_d \tag{3.8}$$

The same control law as before was implemented and link 2 was displaced from its equilibrium. The oscillations were recorded and the simulation returned the following results. The data and the simulation are shown in figure 3-19.

$$
\begin{aligned}
H_{22} &= 0.246 \quad \text{kg-m}^2 \\
b_2 &= 0.181 \quad \frac{\text{Nm}}{\frac{\text{rad}}{\text{sec}}} \\
F_{f_2} &= 0.139 \quad \text{Nm}
\end{aligned}
$$

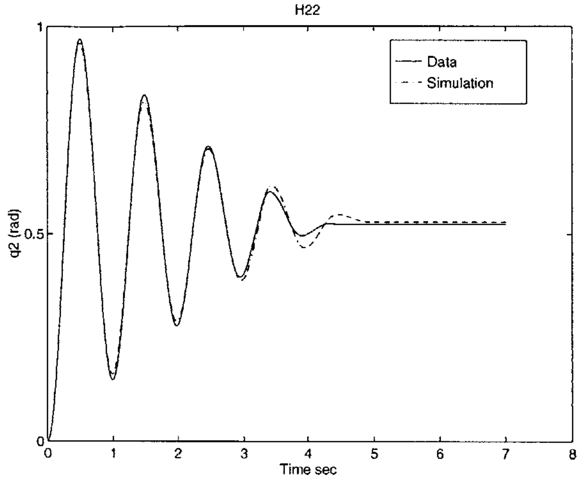

Figure 3-19: This simulation gave the following estimates: $H_{22} = 0.246$ (kg-m^2), $b_2 = 0.181$ $\frac{\text{Nm}}{\frac{\text{rad}}{\text{sec}}}$ and $F_{f_2} = 0.139$ (Nm).

3.5.4 Locking the Elbow Joint in the Relative Frame

Referring back to equation 3.4, the only term left to identify is H_{12}. This is a configuration dependent term, because $H_{12} = m_2 l_1 c_2 \cos(q_2 - q_1)$. So the term that must be found is actually the coefficient multiplying the cosine term $(m_2 l_1 c_2)$. By locking link 2 relative to link 1 the difference between angles q_1 and q_2 is fixed. In this case, the difference was fixed at:

$$q_2 - q_1 = 0.4554 \text{ rad} \tag{3.9}$$

This difference being fixed enables us to write a new equation of motion.

$$H_{11}^* \ddot{q}_1 + b^* \dot{q}_1 + F_f^* \text{sgn}(\dot{q}_1) + K q_1 = K q_d \tag{3.10}$$

where b^* and F_f^* are the viscous and coulomb friction associated with rotating both actuators simultaneously, and H_{11}^* is given by the following equation:

$$H_{11}^* = H_{11} + H_{22} + 2 m_2 l_1 c_2 \cos(q_2 - q_1) \tag{3.11}$$

Thus the term $(m_2 l_1 c_2)$ in question can be obtained by the following equation.

$$m_2 l_1 c_2 = \frac{H_{11}^* - (H_{11} + H_{22})}{2\cos(q_2 - q_1)} \tag{3.12}$$

The test was performed just as the previous two were conducted. The robot was displaced from its equilibrium and the oscillations were recorded. A simulation was then performed resulting in the following parameter estimates. The simulation and the data are shown in figure 3-20.

$H_{11}^* = 1.028$ kg-m^2

$b^* = 0.407 \; \frac{\text{Nm}}{\frac{\text{rad}}{\text{sec}}}$

$F_f^* = 0.238$ Nm

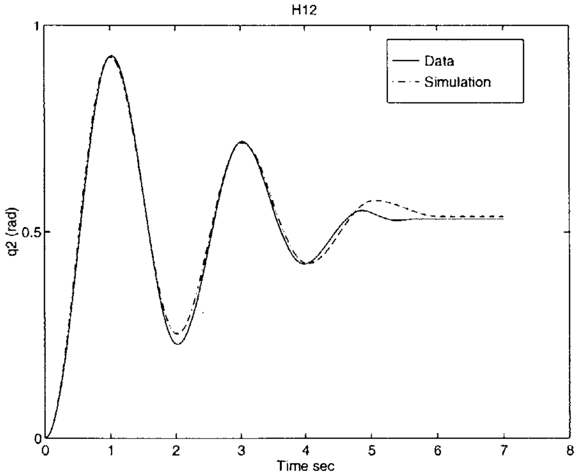

Figure 3-20: This simulation gave the following estimates: $H_{11}^* = 1.028$ (kg-m^2), $b^* = 0.407 \; \frac{\text{Nm}}{\frac{\text{rad}}{\text{sec}}}$ and $F_{f_1} = 0.238$ (Nm).

Using this H_{11}^* and equation 3.12 the off-diagonal term of the inertia tensor can be obtained.

$$m_2 l_1 c_2 = \frac{1.028 \text{ - } (0.349 + 0.246)}{2\cos(0.4554)} = 0.241 \tag{3.13}$$

Thus the H_{12} term was obtained as:

$$H_{12} = \ 0.241\cos(q_2 \text{ - } q_1) \tag{3.14}$$

The values of b^* and F_f^* were expected to take on specific values. The actuators were expected to be the main contributors of viscous damping and coulomb friction. This being the case, b^* was expected to be approximately equal to the sum of b_1 and b_2. Likewise, F_f^* was expected to be equal to the sum of F_{f_1} and F_{f_2}. Both these equalities are satisfactorily attained, and thus all joints not involving the actuators add negligible amounts of damping and friction.

3.5.5 Results

Using the estimates for the H_{ij}, the inertia tensor can be written as follows.

$$H(\vec{q}) = \begin{bmatrix} 0.349 & 0.241\cos(q_2 - q_1) \\ 0.241\cos(q_2 - q_1) & 0.246 \end{bmatrix} \tag{3.15}$$

Another method, using an adaptive controller, was used to estimate the inertia parameters, and it gave similar results. This method is outlined in appendix C of this thesis.

Incorporating the estimates for the b_i and the F_{f_i} allows us to rewrite equations 3.2 and 3.3.

$$\tau_1 = H_{11}\ddot{q}_1 + H_{12}\ddot{q}_2 + \frac{\partial H_{12}}{\partial q_2}\dot{q}_2^2 + 0.222\dot{q}_1 + 0.099\mathrm{sgn}(\dot{q}_1) \tag{3.16}$$

$$\tau_2 = H_{12}\ddot{q}_1 + H_{22}\ddot{q}_2 + \frac{\partial H_{12}}{\partial q_1}\dot{q}_1^2 + 0.181\dot{q}_2 + 0.139\mathrm{sgn}(\dot{q}_2) \tag{3.17}$$

where the H_{ij} are given by equation 3.15.

3.6 Inertia, Damping and Friction Parameters: Functions of Endpoint Position

In the previous section, joint-level estimates of inertia, damping and coulomb friction were given. As most experiments will be designed in cartesian space, it is desirable to transform the joint-level parameters into their cartesian counterparts. The details for how these transformations are carried out can be found in the thesis by Channarong [4].

The results of the transformations are shown in three separate figures. Figure 3-21 shows the inertia parameteres, figure 3-22 illustrates the damping paramaters, and figure 3-23 shows the coulomb friction paramaters. Some common traits are found in all three figures. First, the large circle near the top of each figure represents the actuators of the robot. Next, the large rectangle in each figure represents the workspace. And finally, dotted lines represent arcs of constant radius (the distance from the actuator axis to the endpoint of the robot). Note that the magnitudes of each paramter change as a function of distance (between actuator axis and endpoint) alone. Thus the magnitudes (given in small print in each figure) are the maximum and minimum values of the parameter at that radius.

In addition to these similarities, there is one major difference between the figures as well. The inertia and damping parameters are represented as ellipses while the friction is illustrated as a parallelogram. Past research [4, 17] shows that the inertia and damping of a two degree of freedom mechanism operating in a plane may be understood as an ellipse. The vector (in any direction) from the center of the ellipse to the surface of the ellipse is representative of the inertia or damping in that direction. Statics and geometry show that the joint-level friction of this robot takes on the shape of a parallelogram when projected to the endpoint. And much like the other parameters, the vector from the center of the parallelogram to the surface of it (in any direction) is representative of the friction in that direction.

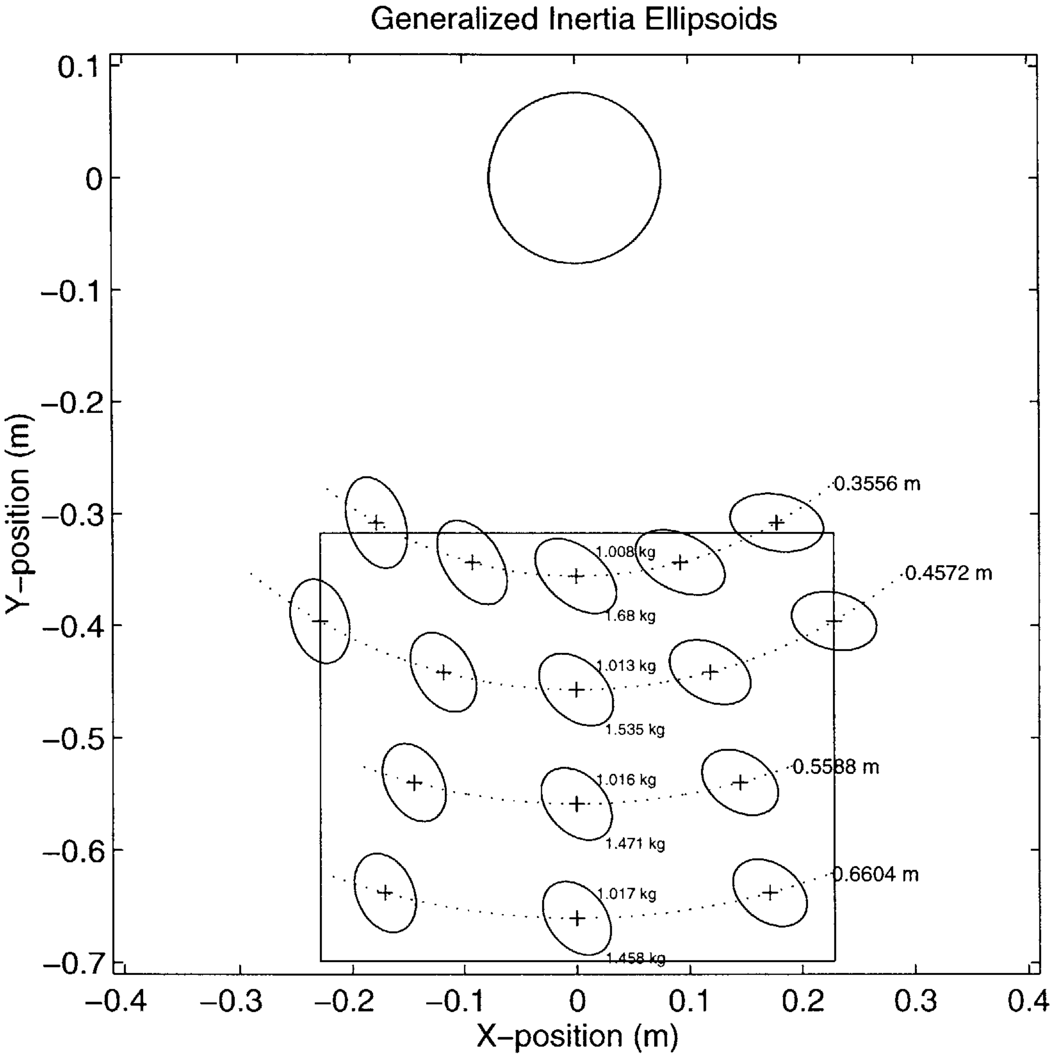

Figure 3-21: Generalized Inertia Ellipsoids

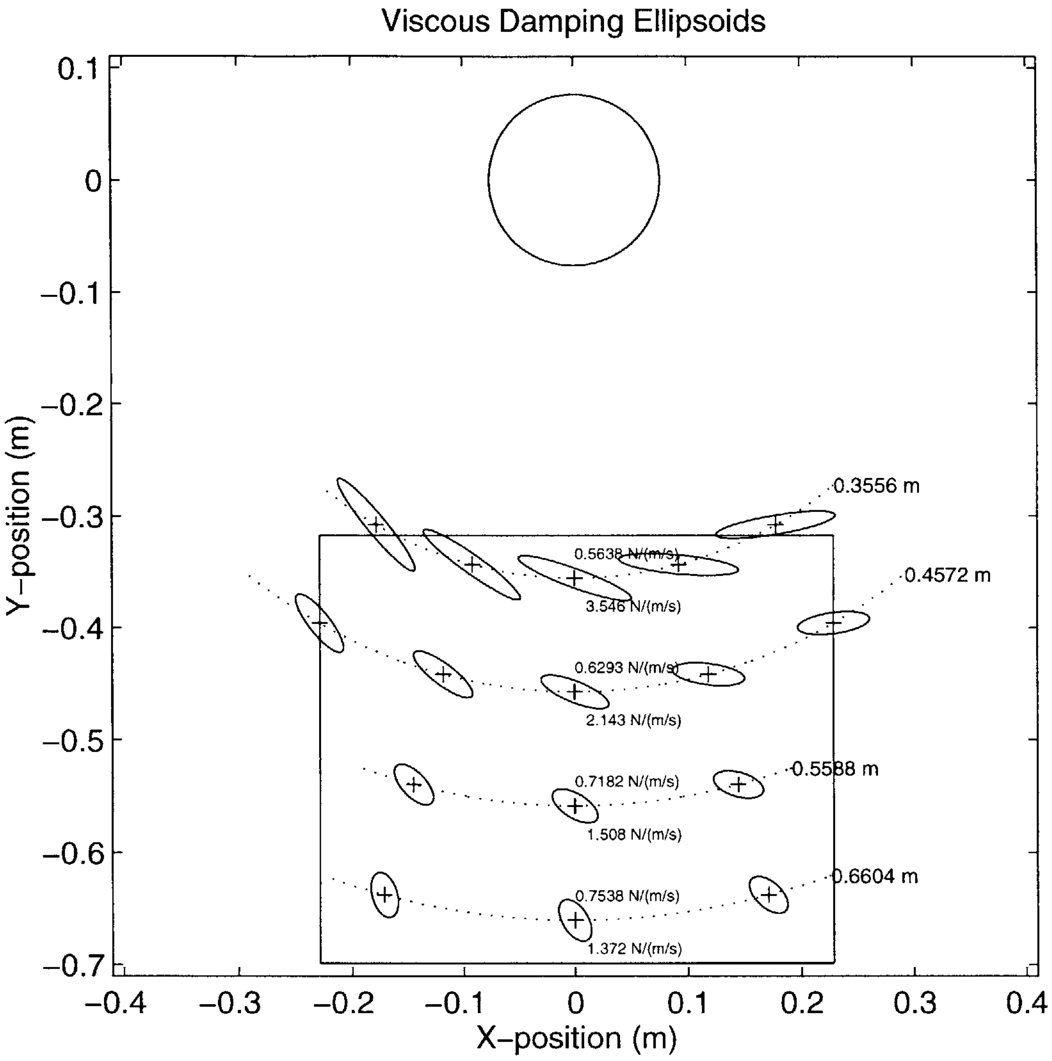

Figure 3-22: Viscous Damping Ellipsoids

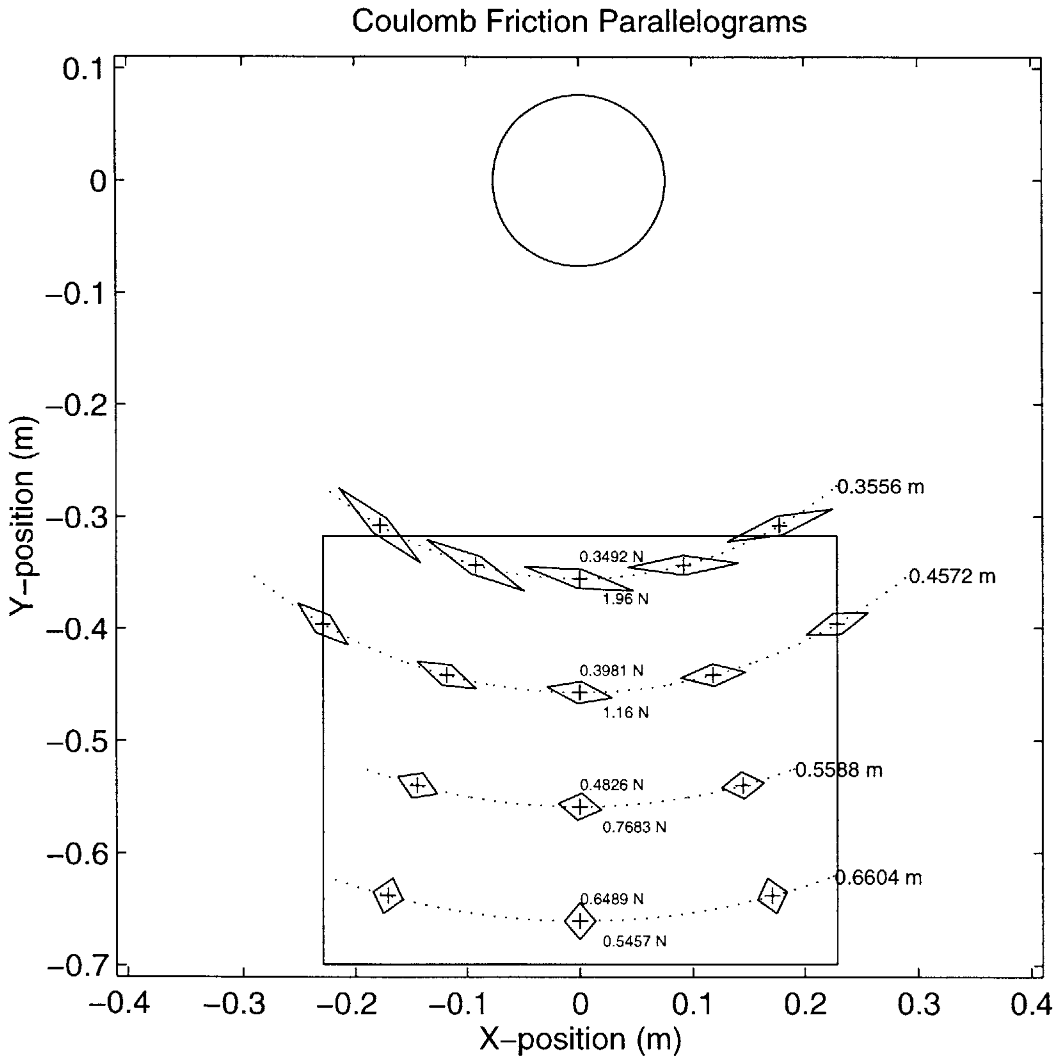

Figure 3-23: Coulomb Friction Parallelograms

3.7 Velocity Estimation

Velocity signals are desired for feedback in the closed loop control of the robot. As there are no velocity sensors on this machine, velocity must be estimated. The simplest approach to estimating velocity is to simply take the first difference of the position signal. This is actually not a bad estimate at high velocities, but at low velocities it causes problems. The problems arise from the fact that the position information is digital and at a finite resolution. Thus, there is a minimum measurable change in velocity Δv_{min}. This Δv_{min} is quite easy to calculate as it depends on the position sensor resolution and the sampling period alone.

$$\Delta v_{min} = \frac{\Delta x_{min}}{T} \tag{3.18}$$

Where Δx_{min} is the smallest record-able change in position, and T is the sampling period.

It is desirable to be able to measure infinitely small changes in velocity. Equation 3.18 shows that both increases in Δx_{min} and decreases in T work to prohibit the measurement of small velocity changes. Decreasing resolution is expected to cause problems, but increasing the sampling rate would normally be expected to help the velocity estimates. Lowering the sampling frequency however, is not an acceptable means of getting better velocity estimates as it can cause other problems. Therefore, the approach of keeping the sampling rate high and using a filter to enhance the velocity estimates was adopted. Currently, the sampling rate is limited by the ATI force transducer which can update no faster than 1066 Hz. The sampling rate has been set to 1000 Hz to simplify calculations and avoid round-off error. Using this rate and the resolution of the position sensor ($131072\frac{counts}{rev}$), a simulation was completed for the first difference velocity estimator. The results of this simulation are shown in figure 3-24.

The results in figure 3-24 show unsatisfactory performance of the velocity estimator. Indeed, a filter is required to attenuate the high frequency noise (quantization noise) on the velocity signal. Taking the simple approach, a first order filter was

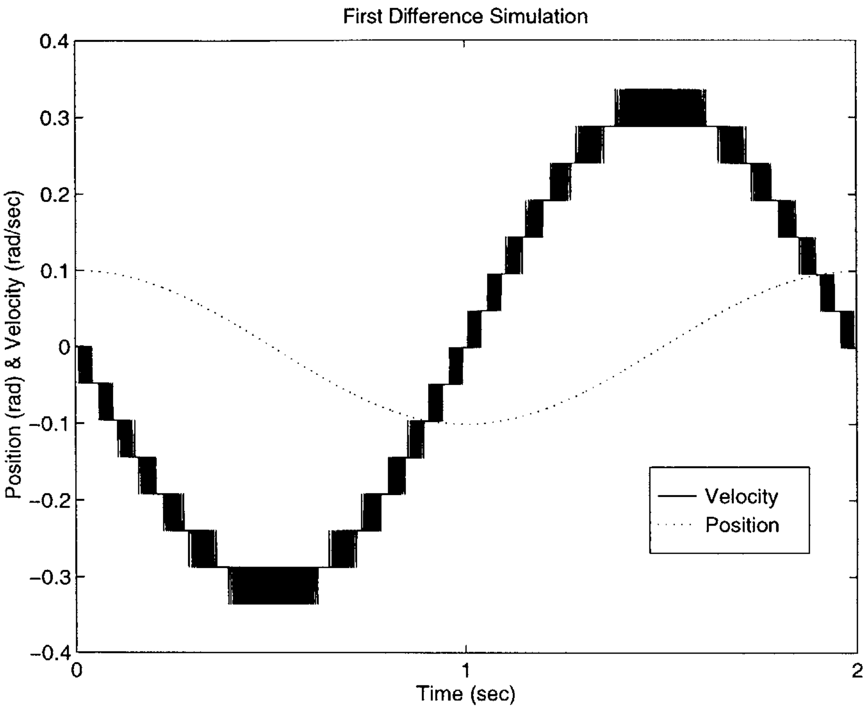

Figure 3-24: Simulation of the first difference velocity estimator: Sampling frequency = 1000 Hz, Position resolution = $131072 \frac{counts}{rev}$

designed and applied to the first difference velocity estimate. The corner frequency of 30 Hz (188.5 *rad*) was chosen for the filter. The trade-off between high frequency attenuation and low frequency phase distortion was considered when making the corner frequency selection. The manipulator is designed for use with humans who can generate velocities with a maximum frequency content on the order of 5 Hz. At 5 Hz, this filter creates 9.3° of phase lag (in theory; see figure 3-25). In general, the movements being studied will contain frequencies on the order of 2 Hz, and the filter creates less than 4° of lag at this frequency.

This filter can be described in the Laplace domain by equation 3.19. A plot of the frequency response of this velocity estimator can be found in figure 3-25. Finally, the simulation that was executed earlier was completed again for this filtered first difference velocity estimator. The results for this simulation show satisfactory performance as illustrated in figure 3-26.

$$\frac{v(s)}{x(s)} = \frac{\lambda s}{s+\lambda} \tag{3.19}$$

Where v is velocity, x is position, and λ is the corner frequency of the filter in $\frac{rad}{sec}$.

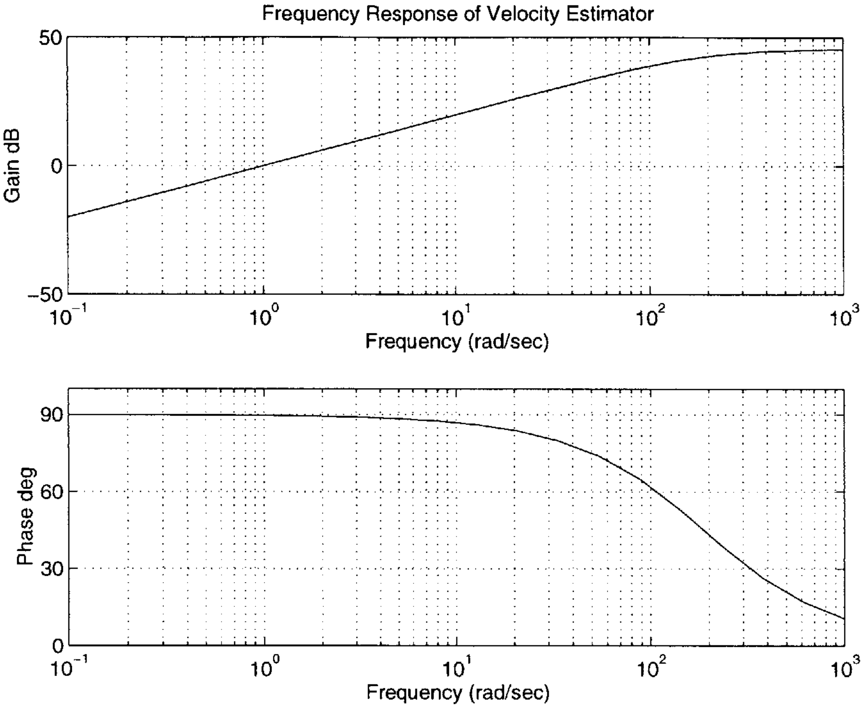

Figure 3-25: Frequency response of the velocity estimator

The possibility that the filter could cause instability of the system was also investigated. For this investigation, the manipulator was considered in its simplified linear form. Also, because the time delay is known to cause instability, it is eliminated from the system in order to isolate the behavior of the filter. Figure 3-27 below shows a block diagram of the system in this simplified form. The corresponding transfer function (mapping actual position to desired position) for this system is given by equation 3.20.

$$\frac{x(s)}{x_d(s)} = \frac{k(s+\lambda)}{ms^3 + (m\lambda + b)s^2 + (b\lambda + b_c\lambda + k)s + k\lambda} \tag{3.20}$$

Where k and b_c are controller gains, and m and b are the inherent mass and inherent damping of the system respectively.

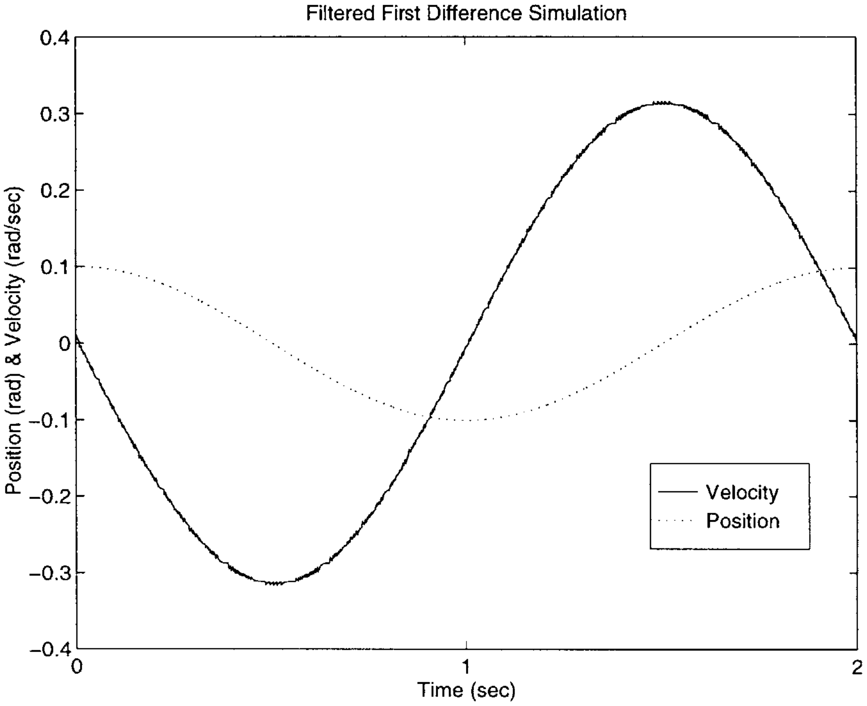

Figure 3-26: Simulation of the **filtered** first difference velocity estimator: Sampling frequency = 1000 Hz, Position resolution = $131072\frac{counts}{rev}$, first order cut-off 30 Hz.

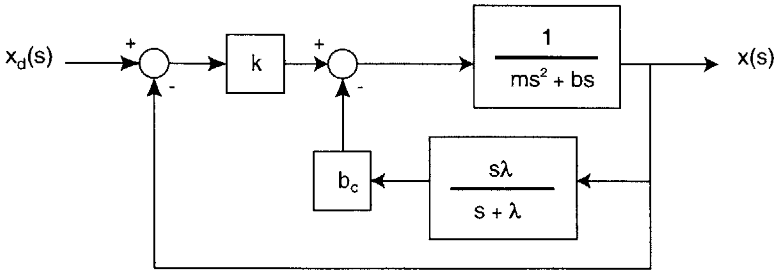

Figure 3-27: Block diagram of the simplified system. This block diagram was created by considering a 1 d.o.f. system with the same linear characteristics of the manipulator and ignoring any nonlinear characteristics

Using the Routh Hurwitz Criterion for stability, this transfer function was confirmed to be stable for all positive values of k, b_c, m, b, and λ. Note, that the inherent mass and damping (m and b respectively) are positive, and that the λ value has been chosen as 188.5 $\frac{rad}{sec}$. Thus the system will remain stable for all positive values of k and b_c. Currently, there is no intention to set negative gains in the controller, so these results show that the velocity estimator by itself is incapable of creating instability.

After establishing that the velocity estimator could not cause instability, it was implemented on MANUS-2. A simple experiment was run to observe the action of the filter. The procedure used in this experiment involved grasping the endpoint of the robot and slowly moving it through the workspace. The results from this experiment are in figure 3-28. It is clear from the plot that the filter performs as expected, attenuating the unwanted high frequency noise.

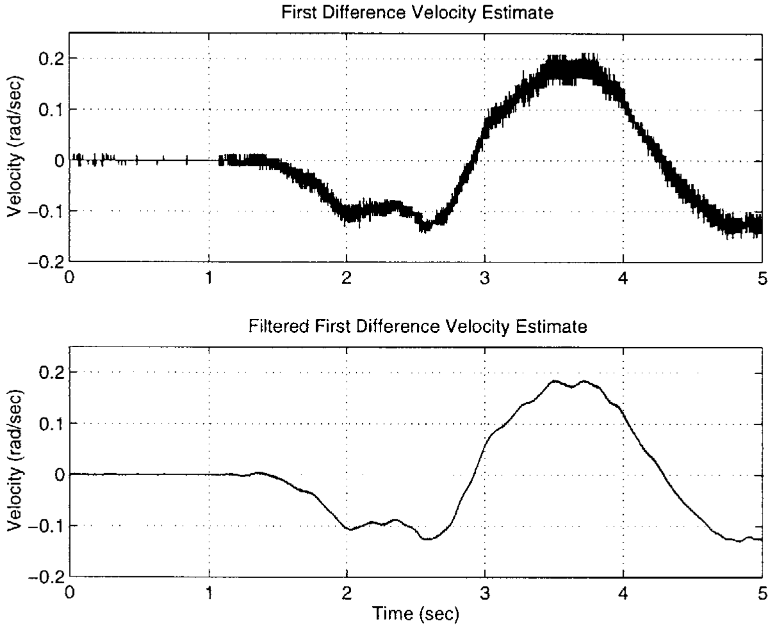

Figure 3-28: Velocity Estimator Implementation: This plot demonstrates the ability of the filter to attenuate unwanted high frequency noise on the velocity signal.

Another important consideration of the velocity estimator is its effect on the poles of the system (denominator of eq. 3.20). The operator should know where the poles of the system are under normal operating conditions. Normal operating conditions are not extremely well defined at this point as the full realm of uses for this machine have not been explored. On the other hand, an earlier version of this sytem has been used extensively in clinical experiments. During these experiments, the controller gains were set to $k = 100\,\frac{N}{m}$ and $b_c = 2\,\frac{\frac{N}{m}}{sec}$. Also, the inherent mass and damping can be estimated at $m = 1\,kg$ and $b = 1.5\frac{\frac{N}{m}}{sec}$ near the center of the workspace (approximated from figures 3-21 and 3-22). Finally, for a cutoff of 30 Hz in the filter, $\lambda = 188.5$. Thus the three poles of the system are at -186.5, and $-1.7 \pm 9.9i$. The response of the system is dominated by the complex conjugate pair of poles. This pair of poles corresponds to a natural frequency of $\omega_n = 1.6$ Hz and a damping ratio of $\zeta = 0.17$.

Chapter 4

Impedance Limits

The purpose of this chapter is to experimentally determine the impedance limits of the robot. Two seperate sets of tests were performed. The first was a group of experiments used to determine the stability of the robot while the endpoint was **not** in contact with an environment. This is called uncoupled stability. The second group of tests was used to determine the stability of the robot while the endpoint was interacting with some known environment. This is known as coupled stability, and in these experiments, the robot was interacting with a spring. The reasons for choosing a spring as the environment will be covered in the section on coupled stabilty. For both the uncoupled and the coupled tests, the robot was considered unstable if it exhibited sustained (i.e. not decreasing) oscillations during the test. Two types of instability were discovered during the testing, and the oscillations were different for each type. These two types of instability, as well as the oscillations defining them, will be discussed later in this chapter.

Recall that the objective of this chapter is to determine the impedance limits for this robot. As the controller uses only position and velocity feedback, the impedance can be modulated using only position and velocity feedback gains. In the context of the controller, position gain can be thought of as controller stiffness, and velocity gain can be thought of as controller damping. Thus the task becomes defining the range of controller stiffness (k) and controller damping (b_c) for which the robot is stable. More details on how the gains affect the system are covered in section 4.3 of this chapter.

4.1 Uncoupled Stability

Three separate experiments were conducted for determing the uncoupled stability of the robot. Each of these experiments was conducted in a different location of the workspace and consisted of several trials. Each of the trials was five seconds in duration. For each trial, the endpoint was servoed to the desired position and then stabilized by hand. Two seconds into the trial, a step in endpoint position was commanded. The table below shows the locations and sizes of steps used for each of the three tests. The locations are measured from the center of the workspace which is 20" (.508m) from the center of the motor axis (see figure 2-2 for workspace layout).

Test	Location		Step	
	x	y	dx	dy
1	0.200	0.226	0.005	0
2	0.269	0.138	0	0.005
3	0	0	0.002	0.002

Table 4.1: Locations and Directions of the step inputs used for uncoupled stability testing

Figure 4-1 summarizes the results of the uncoupled stability tests. All three tests report similar results which will be discussed in section 4.3 of this chapter.

4.2 Coupled Stability

Past research [20, 7, 6, 8, 14] has shown that a manipulator which is stable when uncoupled may become unstable when coupled (to an environment). This *coupled instability* depends on many things, most importantly, the controller and the dynamic properties of the environment. As discussed in Chapter 1, impedance control is the method of choice when faced with such interaction problems. Colgate [7] has shown that for systems such as MANUS-2 using impedance control, an approximation to the worst case environment is simply a spring. Colgate goes even further stating that the

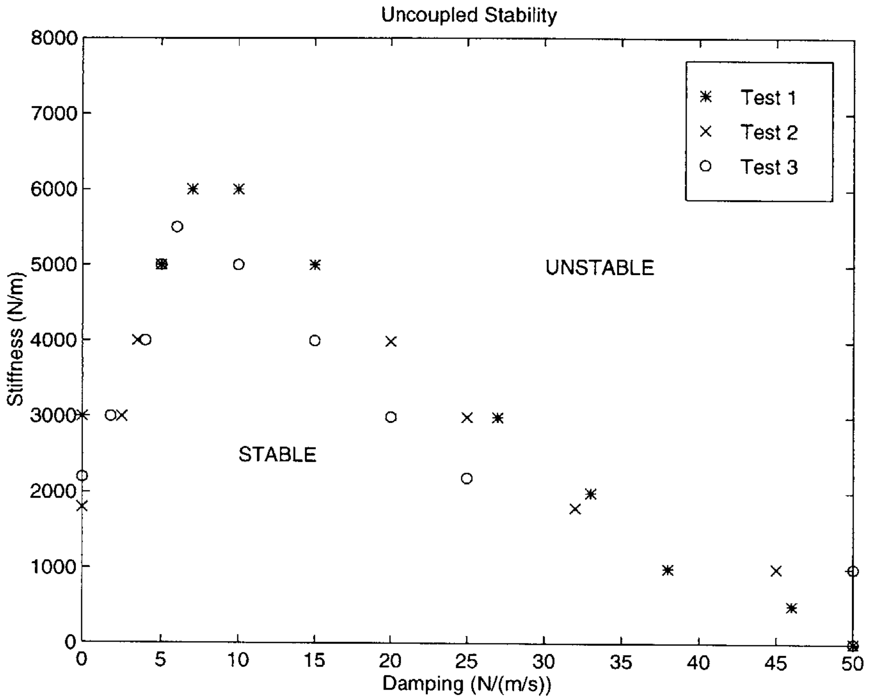

Figure 4-1: Uncoupled stability results

worst case stiffness for this spring is that which resonates at the Nyquist frequency when coupled to the inherent mass of the system. That is to say; $k_{env_{worst}} = \omega^2_{Nyqist}m$, where $\omega_{Nyquist}$ is half the sampling frequency and m is the inherent mass of the system. For this system, the sampling frequency is 1000 Hz or $6283\frac{rad}{sec}$, and the inherent mass is on the order of $1kg$ (note: The inertia of the system is configuration dependent, and $1kg$ is representative of the mass of the system with endpoint positioned near the center of the workspace). Thus $k_{env_{worst}} = (3142)^2(1) \approx 9,872,000\frac{N}{m}$. It is unrealistic to create a test apparatus which has a stiffness of this magnitude. On the other hand, an apparatus with more realistic stiffnesses can be used to gain some understanding about the coupled behavior of the system.

4.2.1 Design of a Test Apparatus

The objective of this section is to give a brief overview of the design of the apparatus used in coupled stability testing of MANUS-2. Two desired features of the test apparatus were considered during the design phase. First, the apparatus should have a wide range of available stiffnesses. Second, it should be easy to use (i.e., changing the stiffness should be easy). The sketch in figure 4-2 shows a design which is capable of satisfying the design constrains. The adjustable support will allow for a wide range of stiffnesses. If the procedure for moving the support is kept simple, changing the stiffness is painless.

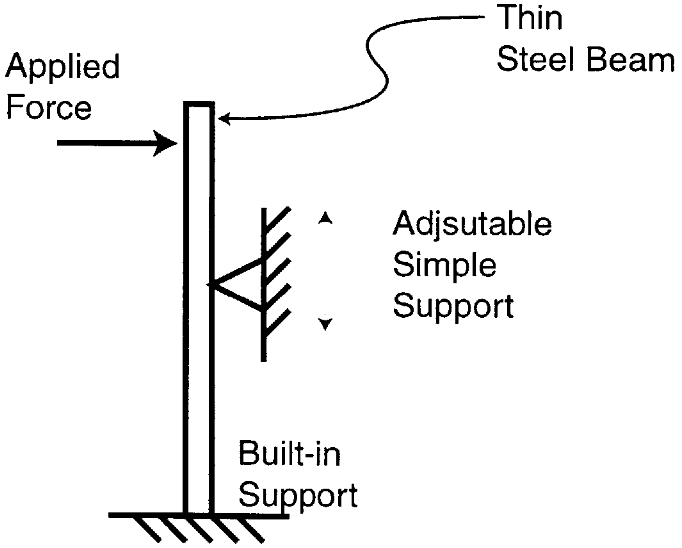

Figure 4-2: Sketch of the variable rate spring test apparatus

This design concept was put to manufacture and the photo in figure 4-3 shows the finished product. Note the quick release mechanism used for adjusting the support. This apparatus was calibrated for 6 different positions (of the adjustable support), and the results of this calibration are shown in the table below. Position 1 is actually the stiffness of the apparatus with the support removed. This calibration was carried out statically using the robot to measure deflection, and the ATI Gamma force transducer to measure force.

4.2.2 Coupled Stability Tests

Tests were completed with the robot coupled to the spring aparatus. The robot was outfitted with a disc that was able to come into contact with the spring. This disc was manufactured so that it would contact the spring at a single point. Figure 4-4 is a photograph of MANUS-2 interacting with the variable spring.

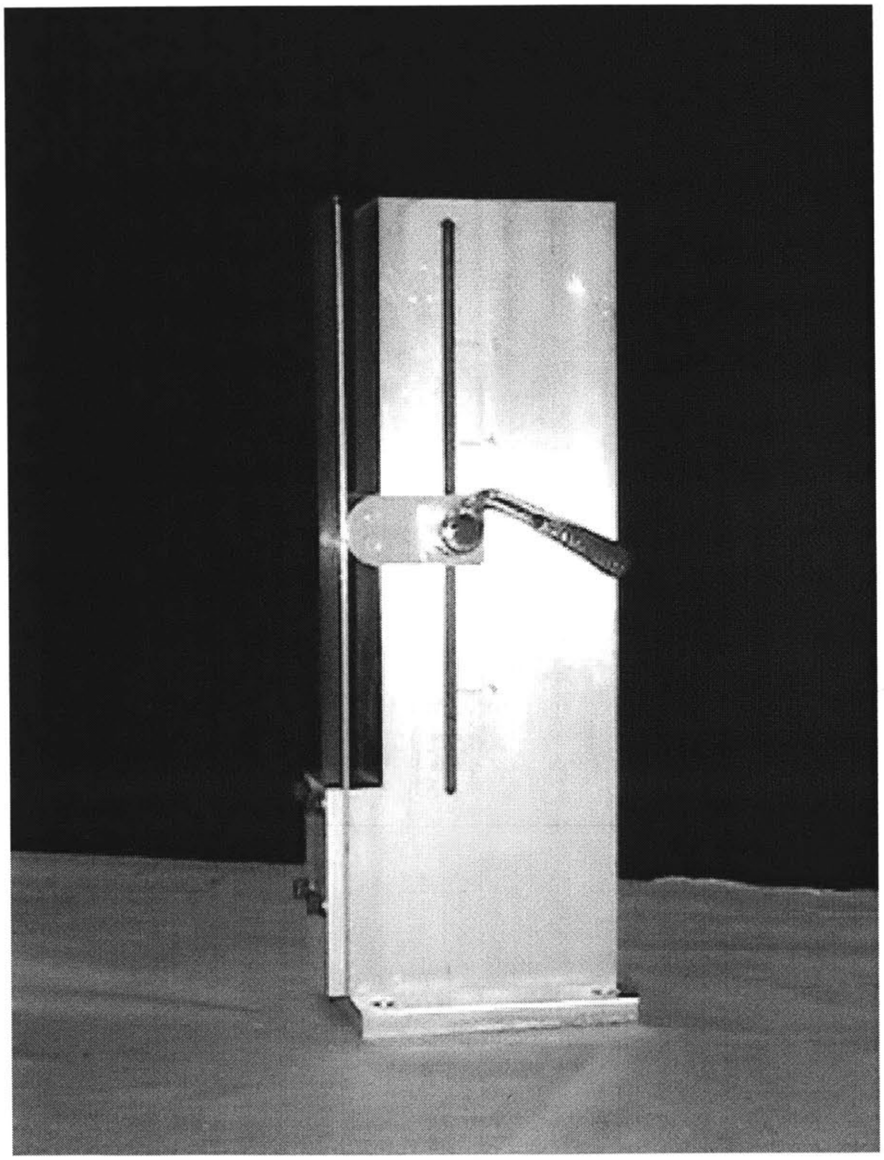

Figure 4-3: Photo of the variable stiffness test apparatus

Position	Stiffness ($\frac{N}{m}$
1	1050
2	1883
3	3826
4	9842
5	34660
6	130900

Table 4.2: Calibrated stiffness values for the variable spring apparatus

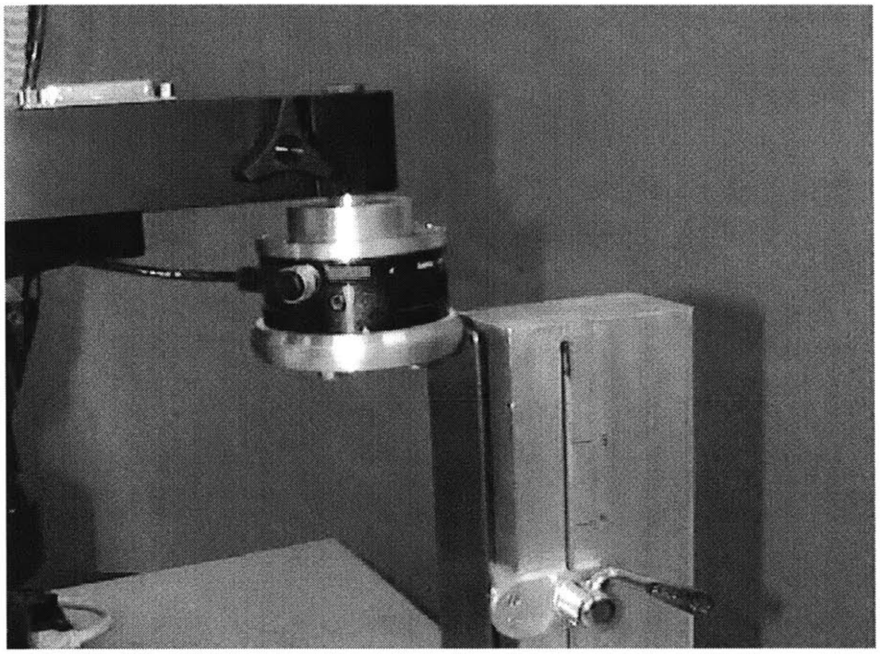

Figure 4-4: Photo of MANUS-2 interacting with the variable spring

The procedure for the coupled experiments was similar to that for the uncoupled experiments. The difference was that the robot was first servoed to a position where it was deflecting the spring (by $1mm$). Then the endpoint was stabilized by hand and finally the step commmand was issued. This method insured that the endpoint remained in contact with the spring for the duration of the test. The coupled stability tests were completed for 2 locations in the workspace. These locations are the same as the test 1 and 2 locations for the uncoupled robot (see table 4.1). The step sizes were also kept the same as in the uncoupled case.

The results of the the coupled stability tests are summarized in figure 4-5. The data in this plot has a great deal in common with data from the uncoupled case.

These similarities as well as some differences will be discussed further in section 4.3 of this chapter.

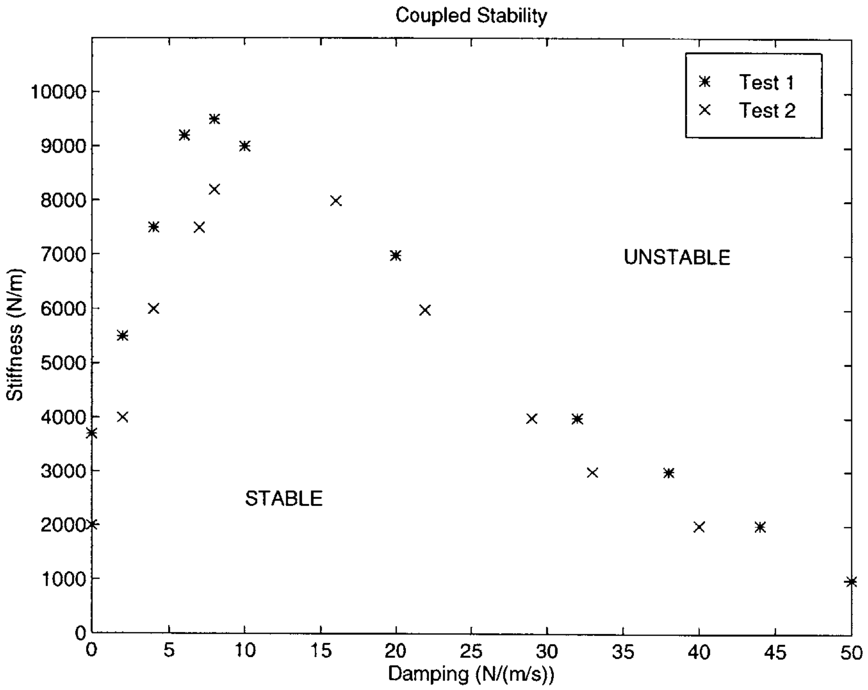

Figure 4-5: Coupled stability results

4.3 Discussion of Results and The Achievable Impedance Range

The shape of the stable region in figures 4-1 and 4-5 suggests that there may be two distinct types of instability; one stability threshold (Type 1) characterized by the positive sloping edge of the stable region, and another stability threshold (Type 2) characterized by the negative sloping edge of the stable region. Based on this evidence, the discussion of the results will be broken down into two sections; one for Type 1 instability, and one for Type 2 instability.

4.3.1 Type 1 Instability Threshold

First, one should understand the type of oscillations which defined the Type 1 instability. As shown in table 4.1 steps of either $5mm$ or $2mm$ were imposed on the system. When the oscillations were sustained at $5mm$ or $2mm$ (zero to peak) respectively, the system was considered marginally stable. The points plotted in figures 4-1 and 4-5 (along the positive sloping edge of the stable region) represent points of marginal stability for the system. If controller stiffness were increased slightly for a given controller damping, the system would be unstable.

In order to understand the Type 1 instability threshold, a simple model was proposed. This model includes the linear properties of the robot as well as the time delay. The model was also reduced to a single degree of freedom. A block diagram of this simplified system is shown in figure 4-6. This system is the same as that shown in figure 3-27 except that now the delay is included. The transfer function for this system (without the delay) is given by equation 4.1. The reason the delay is left out is that frequency response is the tool to be used in this analysis, and the delay affects only the phase aspect of the frequency response. Thus the phase lag due to the delay can be added directly to the phase lag calculated during the frequency response.

$$\frac{x(s)}{x_d(s)} = \frac{k(s+\lambda)}{ms^3 + (m\lambda + b)s^2 + (b\lambda + b_c\lambda + k)s + k\lambda} \tag{4.1}$$

Where k and b_c are controller stiffness and damping respectively, and m and b are the inherent mass and damping of the system respectively.

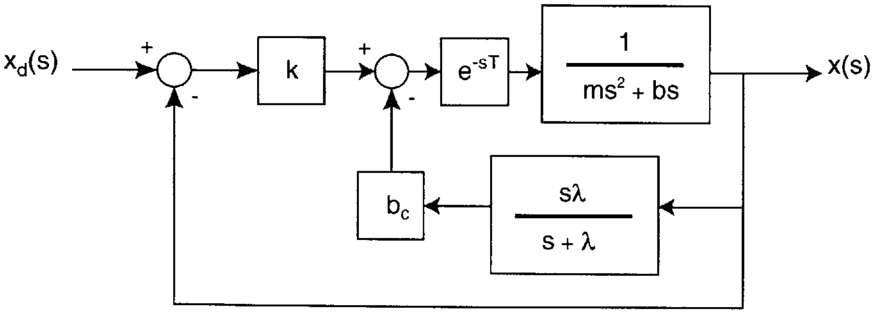

Figure 4-6: Block Diagram of the simplified system

The strategy used in this analysis is to set controller stiffness of the model to unity, and then use the frequency response to get the gain margin of the system. This process is repeated for several values of controller damping in the range of the Type 1 stability threshold. Using the gain margin, the maximum allowable controller stiffness for the selected controller damping value can be calculated. The results of this analysis (for the uncoupled robot) are shown in figure 4-7. The model fits the actual data quite well.

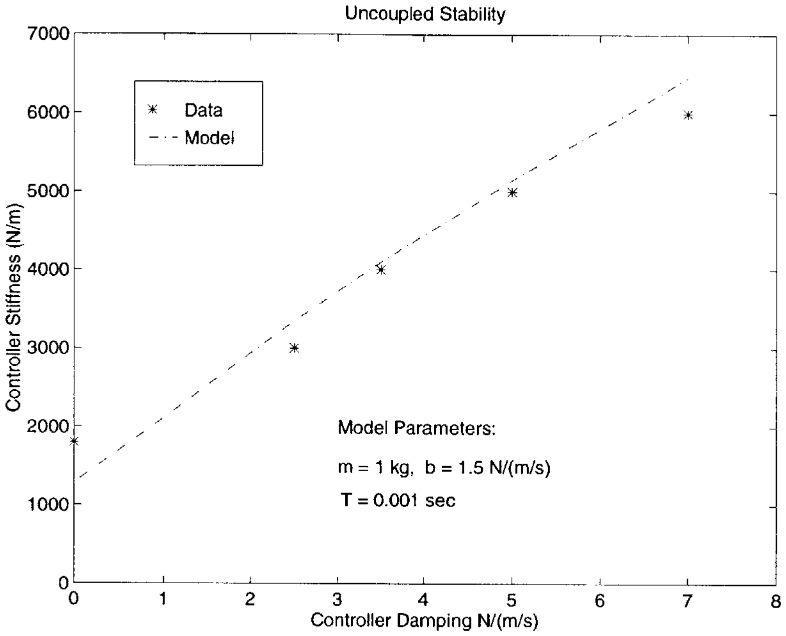

Figure 4-7: Model for the uncoupled stability results

The physical explanation for these results is straight forward. For a fixed value of controller damping, the system becomes more under-damped as the controller stiffness is increased. As the system becomes more under-damped, the 180° phase lag (the relative order of the system is two) becomes very abrupt. Recall that the phase lag is centered at the natural frequency of the system (i.e. -90° at the natural frequency). Therefore, when the system is extremely under-damped, 180° of phase lag can be observed at just above the natural frequency. When the phase lag due to the delay is added into the picture, the system has more than 180° of phase lag rendering it unstable.

This technique was also used in the case of the coupled robot. The new transfer function becomes that of equation 4.2. The results for this analysis are shown in figure 4-8, and again the model fits the actual data very well.

$$\frac{x(s)}{x_d(s)} = \frac{k(s+\lambda)}{ms^3 + (m\lambda + b)s^2 + (b\lambda + b_c\lambda + k + k_{env})s + (k + k_{env})\lambda} \tag{4.2}$$

Where k_{env} is the stiffness of the environment.

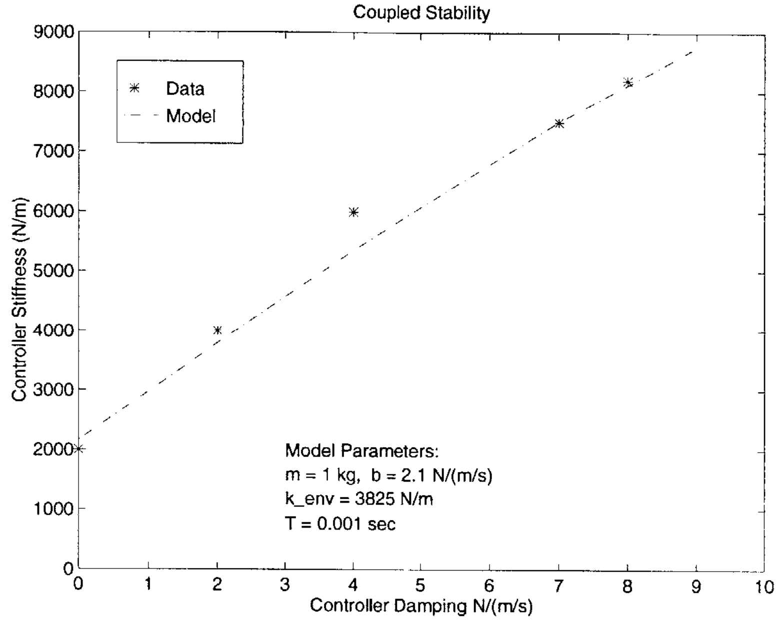

Figure 4-8: Coupled stability results; Note: a higher damping value was used in the coupled case to account for damping and friction added to the system by the variable spring

4.4 Type 2 Instability Threshold

The second threshold of instability is slightly less intuitive than the first. This instability manifested itself in a peculiar way. Given a step input, the robot would exhibit seemingly normal behavior as an underdamped system. A sample of such a time response is shown in figure 4-9. Although the large amplitude oscillations are clearly dying out in this figure, there is a component of vibration which is not decreasing. A close up view of the last 0.2 seconds of the time response shows some higher frequency activity (see figure 4-10). The power spectrum of the last two seconds of the time response shown in figure 4-11 reveals that the frequency of this vibration is on the order of 200Hz. This 200 Hz component of vibration proved to be the source of the type 2 instability. The Type 2 instability threshold is defined by the magnitude of the 200 Hz vibration. The points along the threshold were documented when the 200 Hz vibration could be heard by the operator or could be felt when gripping the endpoint. Upon further examination of the data at each of these points, it was discovered that the power spectral density of the signal at 200 Hz averaged near 10^{-6}.

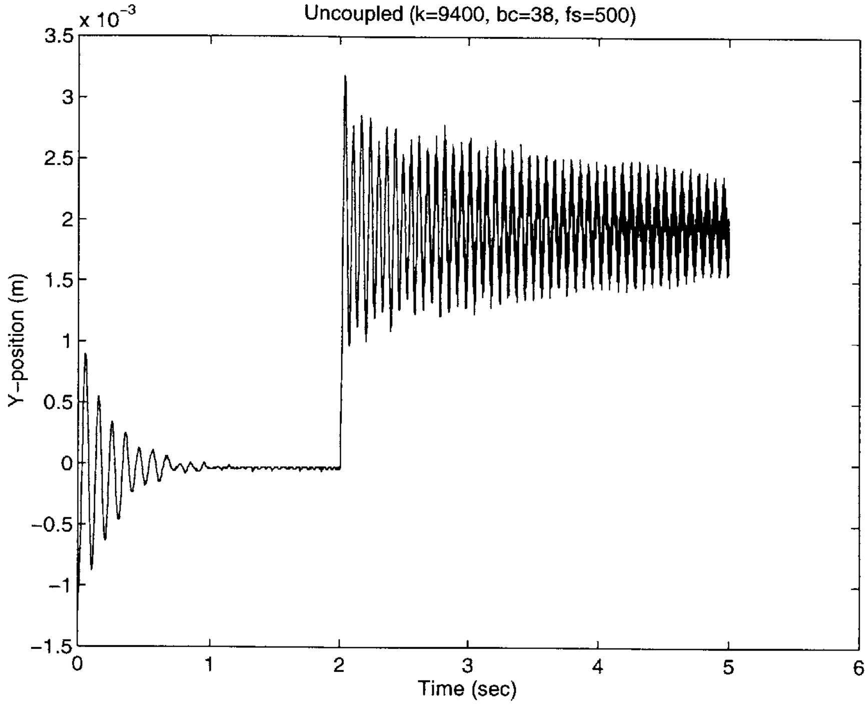

Figure 4-9: Type 2: Closed loop response to a step input

The dynamics of this robot (discussed thoughout this thesis) suggest the system should never exhibit vibrations on the order of 200 Hz. One possibility for the origin of these vibrations was the discrete time controller being used. As mentioned previously, the controller is using a sampling frequency of 1000 Hz which means it is capable of creating inputs at 200 Hz. To verify that the controller was not creating the vibrations at 200 Hz, step input tests were conducted using sampling frequencies ranging from 500 to 2000 Hz. All of these tests showed the same results, significant vibrations on the order of 200 Hz. This strongly suggested that the controller was not at fault.

Another possible origin of the high frequency oscillations was a structural mode of

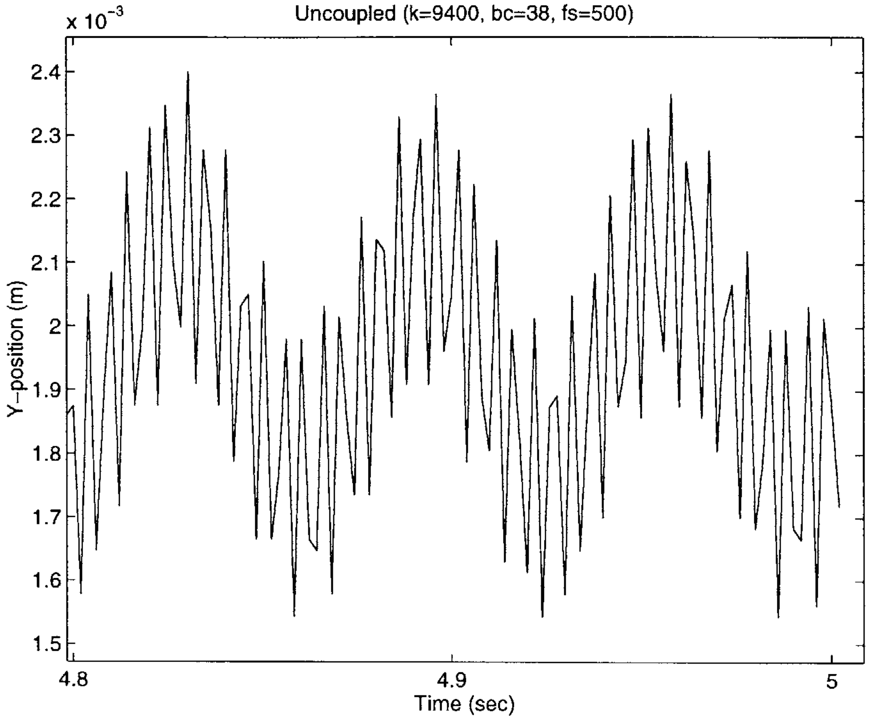

Figure 4-10: Type 2: Closed loop response to a step input (close up)

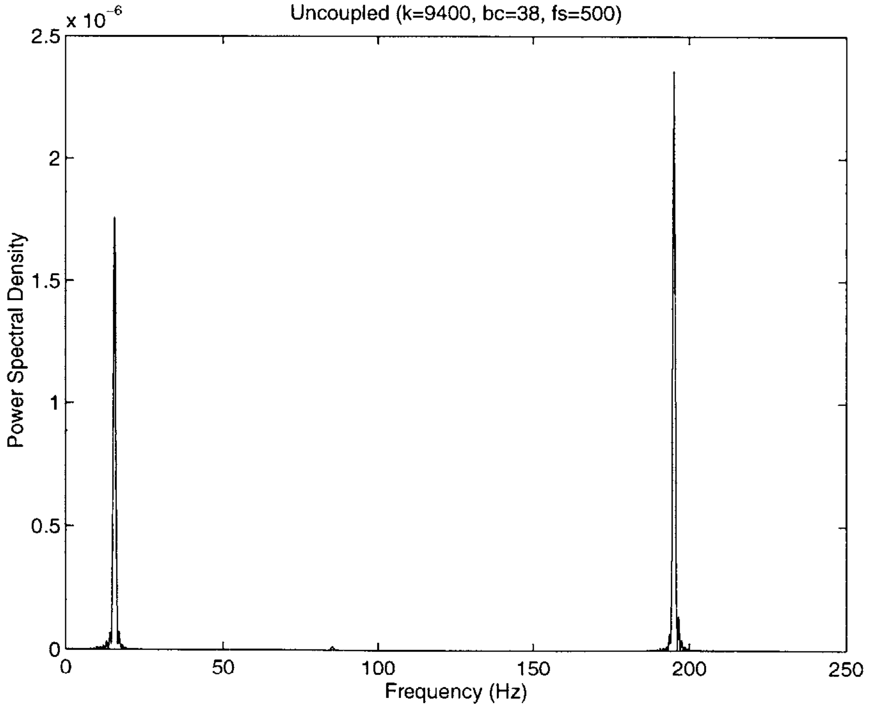

Figure 4-11: Type 2: Spectrum

vibration. This idea gave rise to the following hypothesis: If a structural mode with a natural frequency of 200 Hz existed, it should be able to be excited by open loop input from the actuators. This hypothesis was put to the test by inputing a square wave through each actuator. This square wave had an amplitude of $4Nm$ (zero to peak) and a period of $\frac{1}{10}sec$. The square wave was applied to one actuator at a time with the other actuator remaining inactive throughout the test. Figures 4-12 and 4-13 show the results of these open loop tests. In each figure, the upper plot shows the response recorded by the position sensor of the upper actuator, and the lower plot shows the response recorded by the lower sensor.

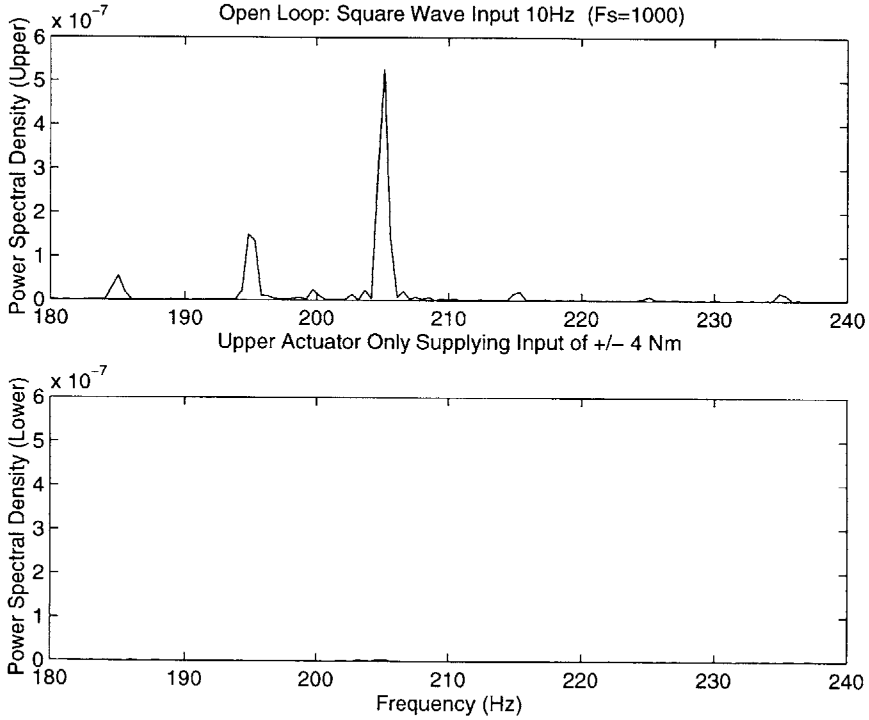

Figure 4-12: Open loop Spectrum (square wave input to upper actuator)

In addition to these spectra, a time plot of the response of the system to the square wave input is shown in figure 4-14. By looking closer at one of the peaks of this plot, evidence of the higher frequency vibration can be seen. Figure 4-15 is a close up view of one of the peaks shown in figure 4-14.

These plots show clearly that some form of structural vibration (on the order of 200 Hz) is taking place. Furthermore, they suggest that the upper actuator is

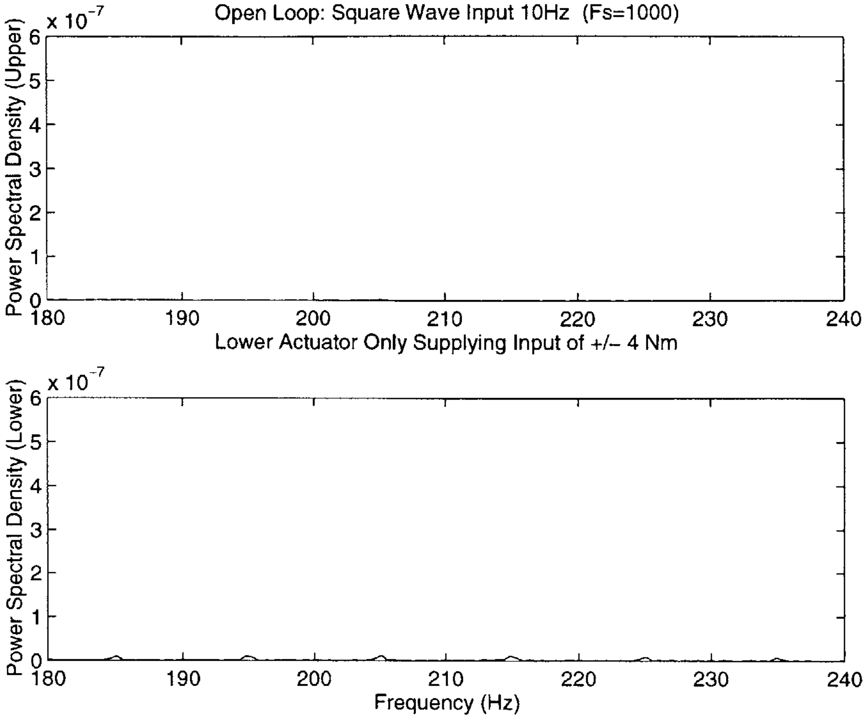

Figure 4-13: Open loop Spectrum (square wave input to lower Actuator)

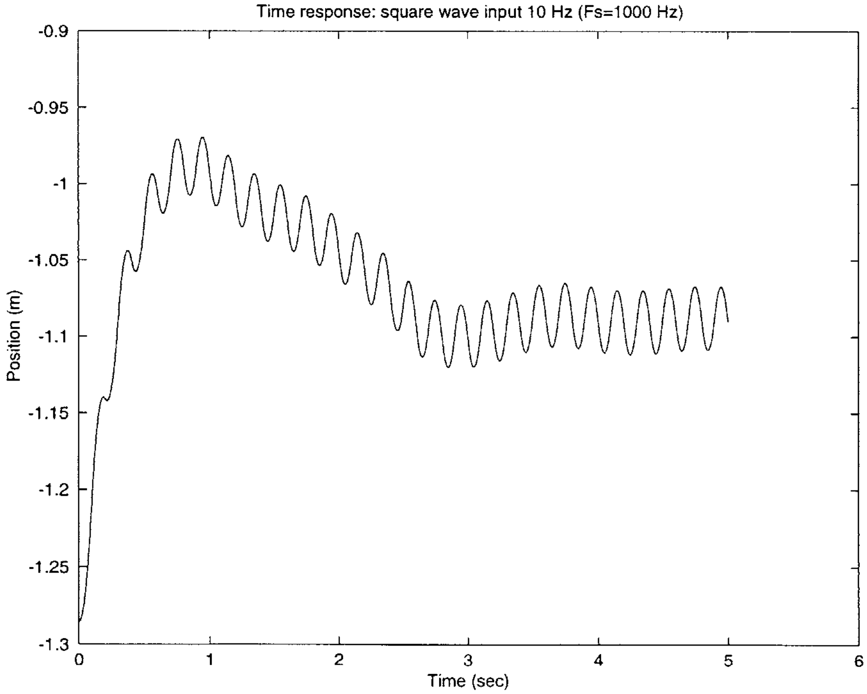

Figure 4-14: Open loop Time Response (square wave input to Upper Actuator)

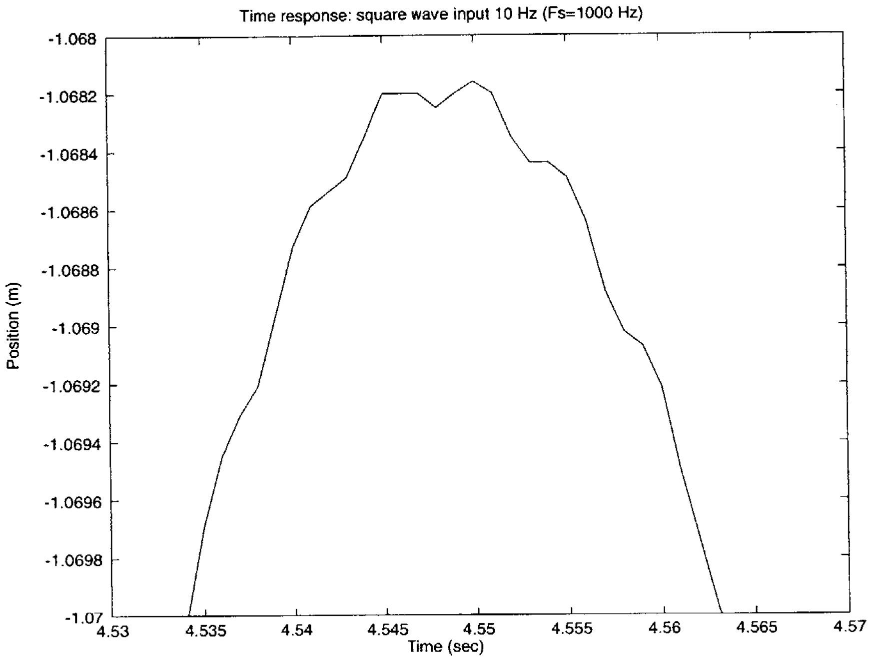

Figure 4-15: Close up: Open loop Time Response (square wave input to Upper Actuator)

the most likely culprit. This data led to another hypothesis regarding this behavior: Compliance along the shaft of the upper actuator is the source of the structural vibration at 200 Hz. This hypothesis was developed because the actuator shaft is actually in several sections which are bolted together. Also, The upper actuator shaft had exhibited problems in the past (bolts connecting two sections of the shaft had worked themselves loose).

4.5 Simulating Type 2 Instability

In order to show that compliance along the actuator shaft could cause the robot to exhibit the behavior seen in the stability experiments, a model was developed. This model starts with the initial actuator model as a foundation and adds to it one degree of freedom. The initial actuator model was that of just a mass with damping, and to add a degree of freedom, another mass was attached via a spring and damper. A sketch of the new model as well as the corresponding transfer function can be found in figure 4-16. In addition, a Bode plot of this new transfer function can be found in figure 4-17.

For this Bode plot, the following parameter values were used: $b = 1.5\frac{N}{\frac{m}{s}}$, $b_2 = 2.0\frac{N}{\frac{m}{s}}$, $m = 0.1kg$, $m_2 = 0.9$, $k_2 = 170000$. These values were chosen using information gained from previous experiments. The system identification experiments allowed for the approximation of the total mass of the system at 1.0 kg near the center of the work space. The geometry of the robot dictates that the linkage mass (m_2) is about 90% of the total mass of the robot. Likewise, the system identification experiments allowed for the approximation of the actuator damping (b) at around $1.5\frac{N}{\frac{m}{s}}$ near the center of the workspace. Finally, b_2 and k_2 were chosen such that the system would have a lightly damped resonance at 200 Hz.

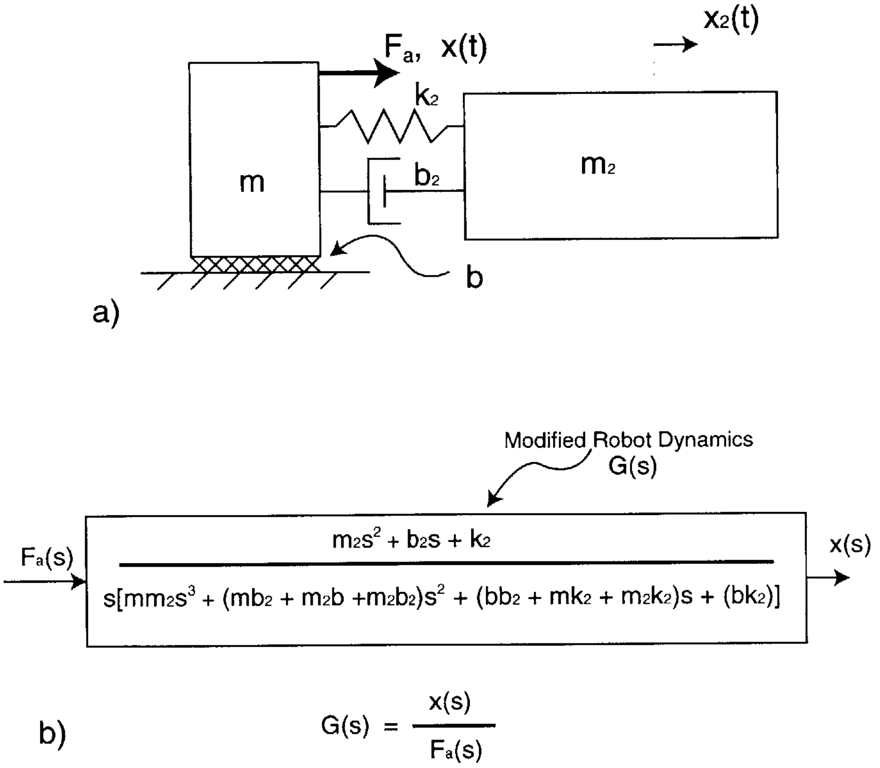

Figure 4-16: a) simplified mechanical representation of the robot system with compliance along the shaft b) the corresponding transfer function

A simulation of the square wave input test was also completed to demonstrate that the open loop transfer function could exhibit similar behavior to that seen in the experiment. The simulated time response of the open loop system to the square wave input is shown in figure 4-18. The power spectral density of this response was then computed and is shown in figure 4-20, and by comparing this figure to figure 4-12 the

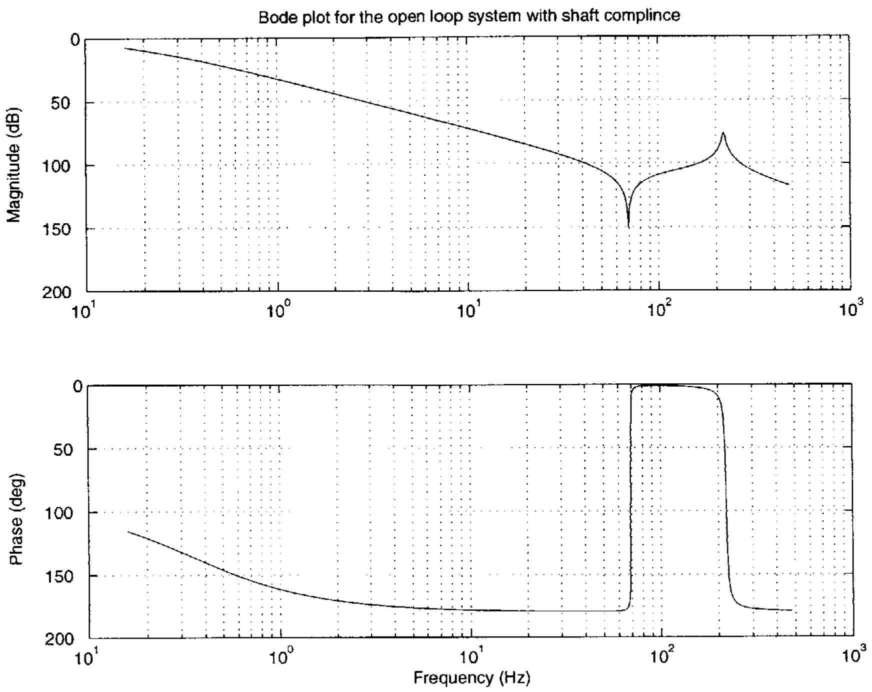

Figure 4-17: Bode plot of the open loop transfer function including shaft compliance; The open loop zero-pair occurs at $69.2Hz$ and has a damping factor of $\zeta = 0.0025$ and the open loop pole-pair occurs at $218.7Hz$ with $\zeta = 0.013$

similarities between the model and the actual system can be identified. The model and the system both have some vibration just above 200 Hz, but the model has lower magnitude. The later simulations will show that the model parameters have been tuned carefully enough to emulate the behavior of the system.

Next, the new transfer function was placed into the closed loop system. This allowed for the simulation of the stability experiments involving step inputs. Simulink (the MATLAB simulation engine) was chosen to complete these simulations. The Simulink block diagram is shown in figure 4-21, and includes some new elements. The two new elements are the zero-order hold, and the quantizer. The zero-order hold allows for the integration of the continuous time robot dynamics with the digital controller; it is the sampling frequency of the controller ($0.001sec$). The quantizer simulates the effect of the discrete position sensor (the encoder). The quantization step is $2.4 \times 10^{-5} \frac{m}{count}$. This step is the approximate linear distance traveled between encoder counts. Also, notice that the model includes the time delay of $0.001sec$. This is the pure time delay of the amplifier as described in Chapter 3. Recall that the

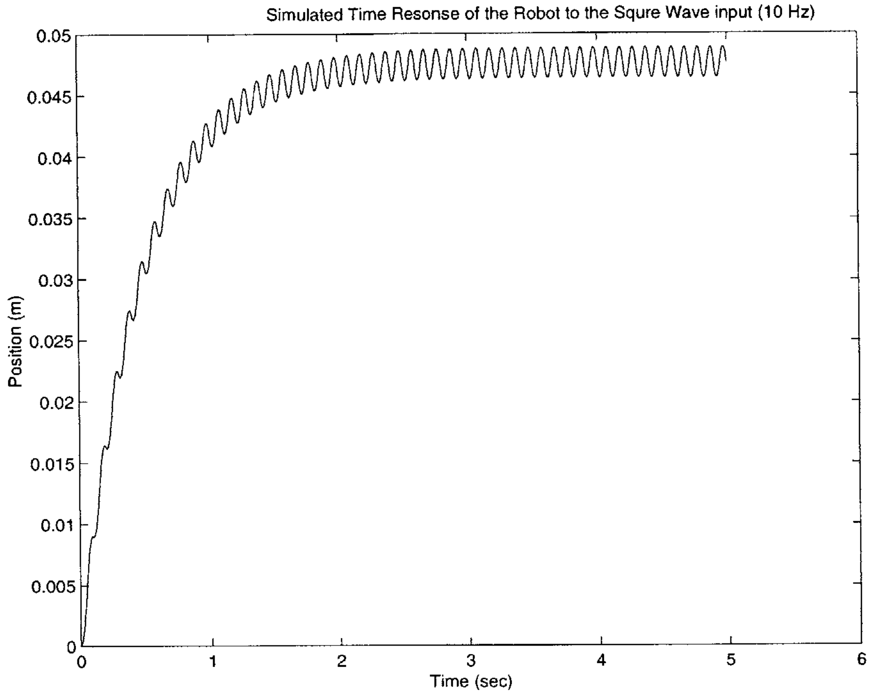

Figure 4-18: Simulated time response of the modified open loop transferfunction to a 10 Hz square wave input; compare this simulation to the experimental data in figure 4-14

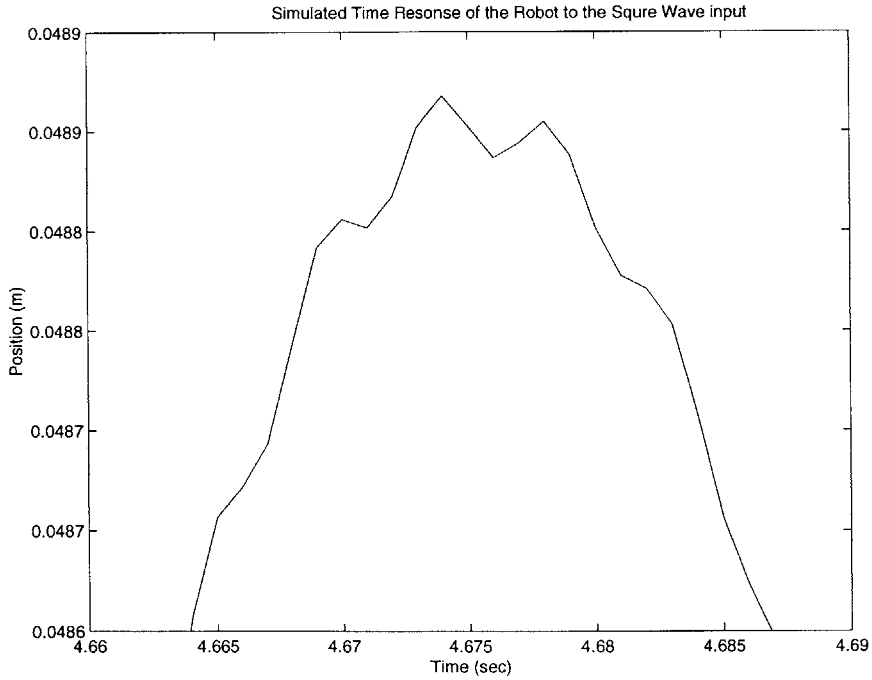

Figure 4-19: Close up: Simulated time response of the modified open loop transferfunction to a 10 Hz square wave input; compare this simulation to the experimental data in figure 4-15

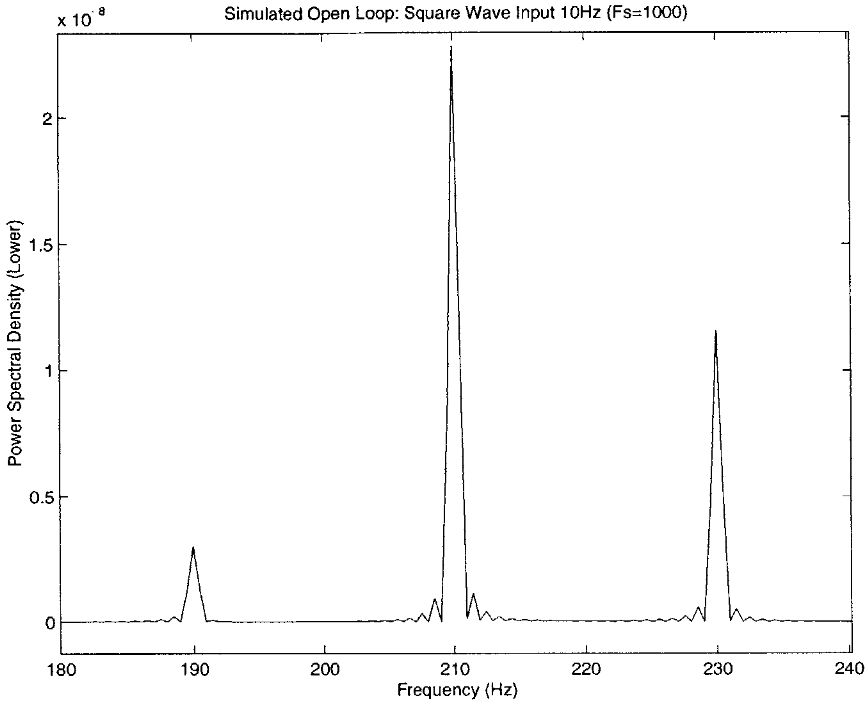

Figure 4-20: Power spectral density of the simulated response; compare this simulation to the experimental data in figure 4-12

total delay discussed in Chapter 3 was 0.002*sec*, but 0.001*sec* was attributed to the sampling order used during data collection. This is the reason 0.001*sec* is used in the simulations.

Using this Simulink model, the stability experiments discussed earlier were simulated. The controller stiffness (k) and damping (b_c) could easily be adjusted and the the Type 2 stability threshold estimated in much the same way that the experiments were conducted on the robot. Figure 4-22 shows a typical time response for a point on the Type 2 stability threshold. A close up of this time response is shown in figure 4-23. This time response clearly shows high frequency oscillations, and can be compared with the experimental data shown in figure 4-10. Like the experimental data, the power spectral density of the simulated response was computed. These results are found in figure 4-24. Once again, the power spectral densitiy of the simulation can be compared to that of the data (4-11) in order to see the distinct similarities.

The threshold of Type 2 instability was only loosely defined earlier in this chapter. It was stated that the points along the Type 2 threshold contained a 200 Hz

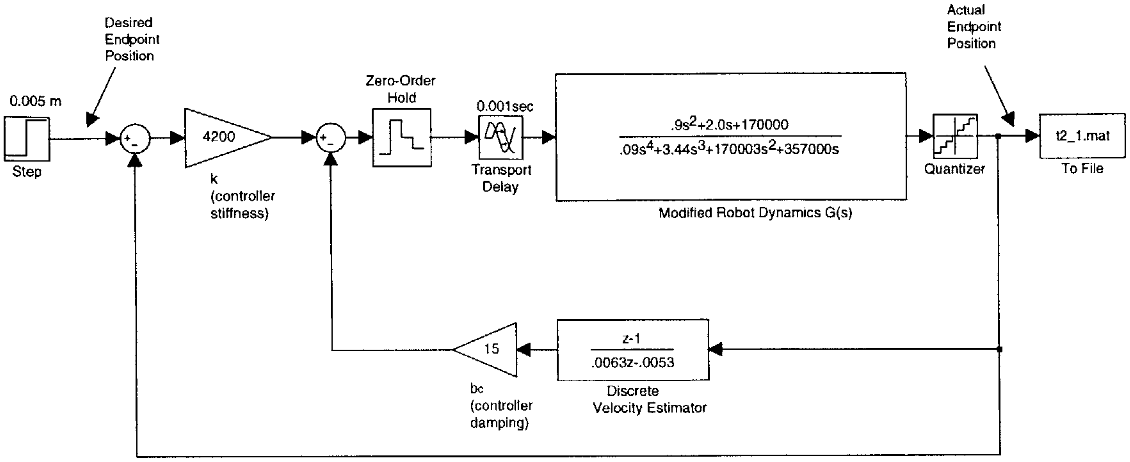

Figure 4-21: Block diagram used to simulate the complete system in Simulink

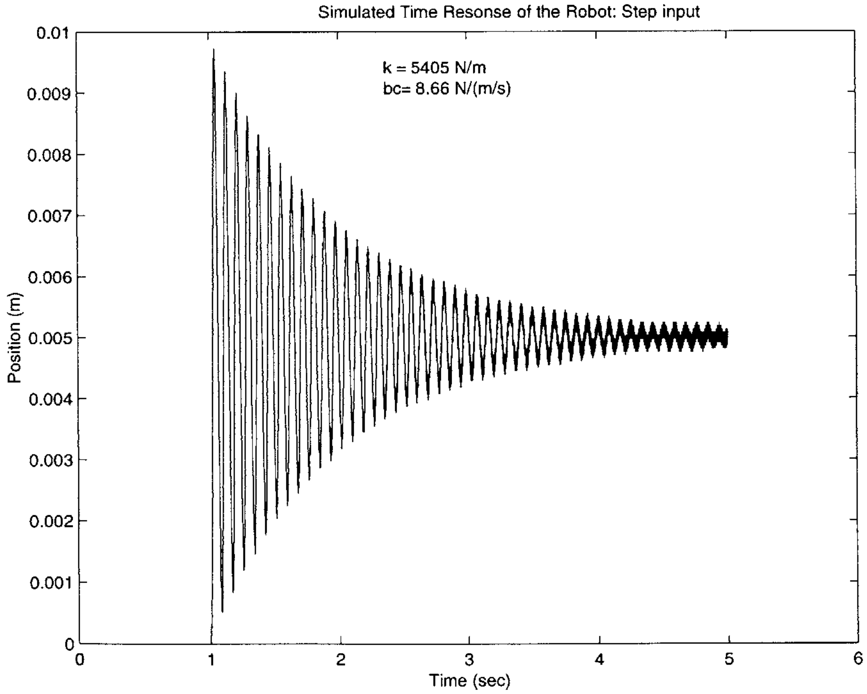

Figure 4-22: Simulated time response to a step input of $5mm$; compare this simulation to the experimental data in figure 4-9

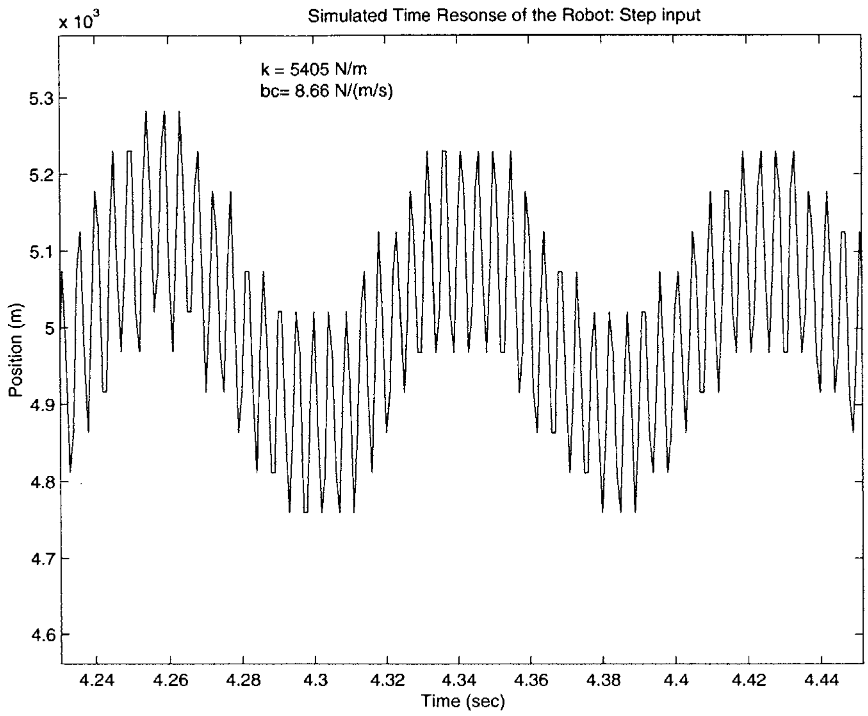

Figure 4-23: Close up: Simulated time response to a step input of $5mm$; compare this simulation to the experimental data in figure 4-10

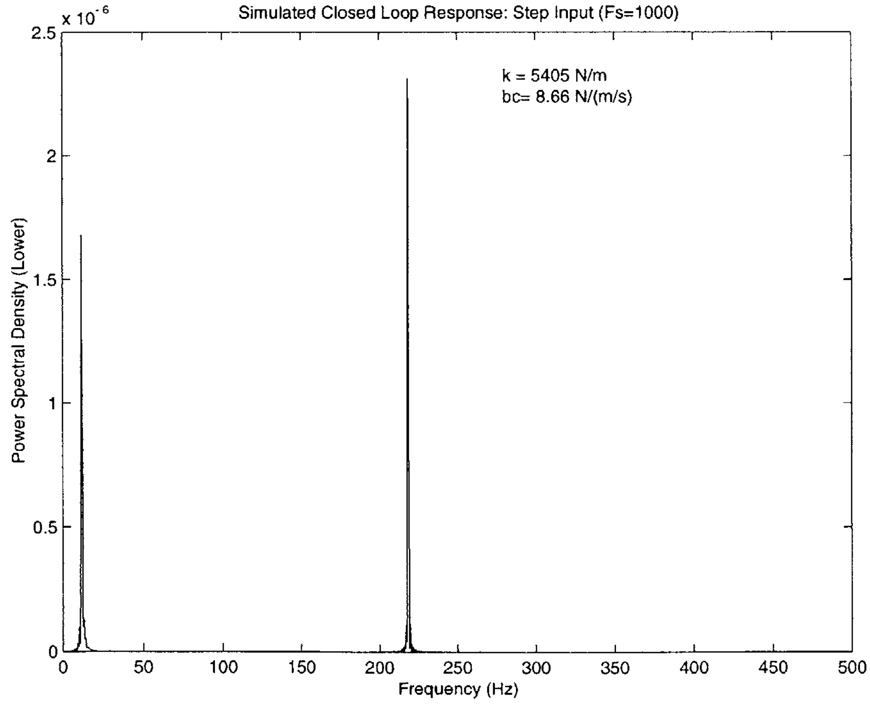

Figure 4-24: Power spectral density of the simulated time response to a step input of $5mm$; compare this simulation to the experimental data in figure 4-11

component of vibration with a power spectral density of 10^{-6} or greater. This power spectral density calculation was determined using only the final second of data in the five second test. This notion was justified because if the behavior is truly unstable, the 200 Hz vibration should be increasing with time. Using this idea, one can more firmly define the Type 2 instability threshold. For each value of controller damping b_c a point on the Type 2 instability threshold may be determined by finding the value of controller stiffness k which results in a 200 Hz component of vibration with a power spectral density of 10^{-6}. Using this definition, the Simulink model was used to solve for points on the Type 2 threshold. The results are shown in figure 4-25. This is a repeat of the plot shown in figure 4-1 with the simulation results superimposed over the data. Notice that the simulation accurately models both the Type 2 threshold as well as the Type 1 threshold. This is because the model includes the time delay which is the important factor in determining the Type 1 threshold. This model can also be used to determine the maximum negative damping value. The simulations showed that the value of $-1.5\frac{N}{\frac{m}{s}}$ was the largest negative damping value which could be simulated in a stable manner. This is exactly what was expected as the controller should be able to apply as much negative damping as there is real physical damping in the system (a notion pointed out by Colgate [7]). An experiment could be carefully executed on the robot to verify that the model projections are correct.

The final useful aspect of the model is that it can be used to see how the individual parameters effect the stability thresholds. In this respect, the model should be subjected to a rigorous sensitivity analysis to determine the most effective means of improving the robot design. Although this thesis will not cover a complete sensitivity analysis, the model was used to come up with a brief summary of how the individual parameters effect the stability thresholds. First, the extra degree of freedom in the robot should be eliminated. Without this degree of freedom, the robot would not exhibit Type 2 instability. Next, decreasing time delay raises both Type 1 and Type 2 thresholds. Also, decreasing the quantization step raises the Type 2 threshold. Contrary to intuition, increasing the sampling frequency lowers the Type 2 threshold. This is due to the discrete velocity estimation being used. On this note, the

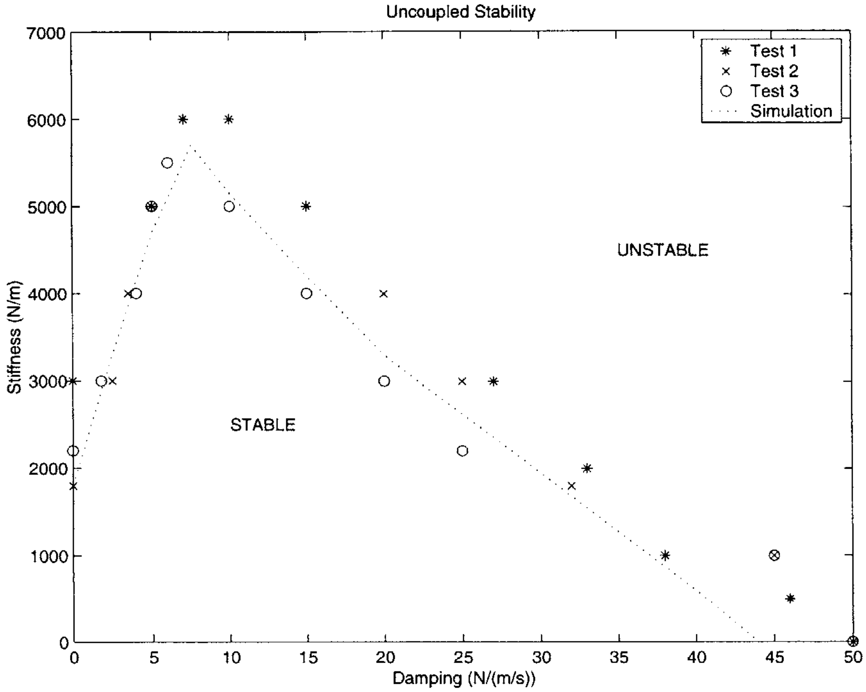

Figure 4-25: Actual and Simulated stability thresholds

method of obtaining a velocity measurement is very crucial to stability of the robot. Although it was not done in this thesis, alternative velocity (digital) estimators as well as different types of velocity sensors should be investigated to determine which is the best for obtaining stability with high damping values.

4.6 The Actual Endpoint Impedances

Although efforts were made to insure that MANUS2 will exhibit endpoint impedance requested by the operator, there are many factors which may prevent it from doing so. An experiment was conducted to show how accurately MANUS2 can exhibit the endpoint impedances requested of it. The experiment was conducted in two parts; one to measure the actual stiffness of the robot and the other to measure the actual damping in the robot. The values tested were near the maximum allowable values which were discussed earlier in this chapter.

For both tests the endpoint of the robot was first placed in the center of the workspace. For the stiffness tests, controller stiffness (k) was then set to $5000\frac{N}{m}$ and the controller damping (b_c) was set to zero. The robot was then displaced in the x-direction (small displacements were used to avoid saturation of the actuators). During the test, both the x-displacement and x-force were measured. This test was then repeated for the y-direction. The results of these stiffness experiments are illustrated in figures 4-26 and 4-27.

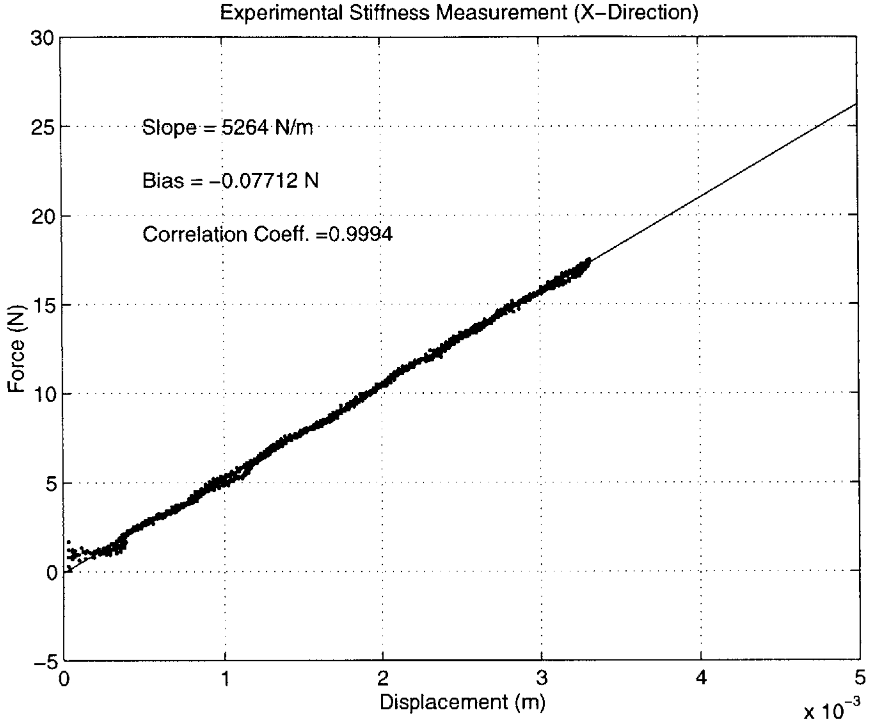

Figure 4-26: Actual X-Stiffness: controller stiffness set at $5000\frac{N}{m}$

Figures 4-26 and 4-27 show that the x and y-stiffnesses were measured at $5264\frac{N}{m}$ and $5206\frac{N}{m}$ respectively. These values are 4 to 5% higher than the set value of $5000\frac{N}{m}$. Although this error is satisfactorily small, some discussion of what errors were expected is necessary. The main sources of error in the stiffness measurement stem from the calibration of the force sensor. The calibration of the ATI Gamma Force/Torque sensor in Appendix B shows some error for both torque and force measurements (1% for torque, and 2% for force). The error in the torque mesurements is reflected in the robot's ability to accurately produce joint torques as the ATI was used to calibrate the actuators. In addition, the ATI was used to measure the forces applied by the robot during the stiffness experiments. Thus the expected error in applied torque is

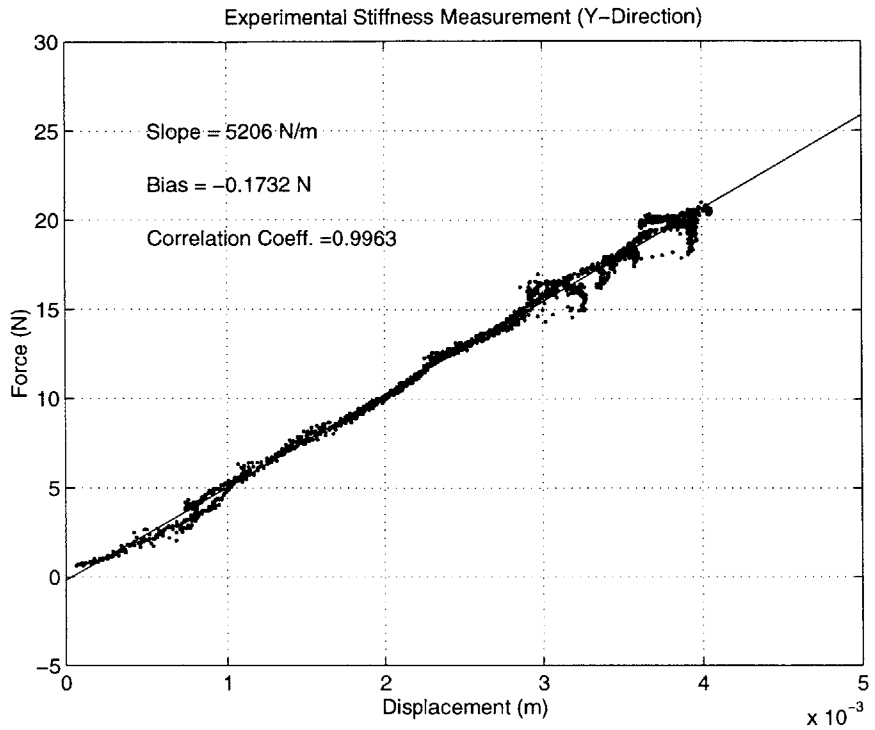

Figure 4-27: Actual Y-Stiffness: controller stiffness set at $5000\frac{N}{m}$

1% and the expected error in measured force is 2%. Therefore the force transducer is capable of accounting for up to 3% of the error seen in the stiffness measurements.

For the damping tests, the controller used the following values: $k = 0$ and $b_c = 40\frac{\frac{N}{m}}{sec}$. The endpoint was then accelerated (by hand) in the x-direction and then brought to a stop again. During this test, both the x-velocity and the x-force were recorded. The test was again repeated in the y-direction. It is important to note that the total damping which was expected at the endpoint was the value of b_c $(40\frac{\frac{N}{m}}{sec})$ plus the inherent damping and any static friction of the mechanism. The inherent damping is configuration dependent, but can be approximated using figure 3-22. The results of the damping experiments are shown in figures 4-28 and 4-29.

Figures 4-28 and 4-29 show that the x and y-damping values were measured at $44.2\frac{\frac{N}{m}}{sec}$ and 43.3 $\frac{\frac{N}{m}}{sec}$ respectively. After taking into consideration the inherent damping of the mechanism in each case, these values are 6% higher than set values. Again, this small percent error is considered satisfactory. The peculiar loop created by the data in each plot is believed to be due to the fact that the tests were not performed

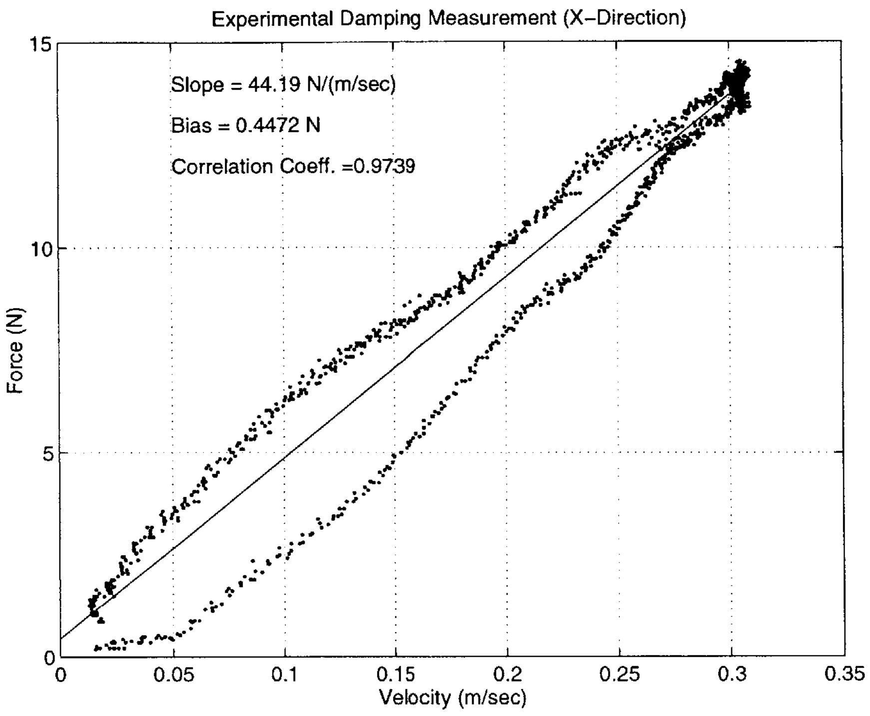

Figure 4-28: Actual X-Damping: controller damping set at $40\frac{N}{\frac{m}{sec}}$ inherent damping approximated at $1.6\frac{N}{\frac{m}{sec}}$: Expected total damping = $41.6\frac{N}{\frac{m}{sec}}$

at constant velocity. The end point of the robot was slowly accelerated and then decelerated again during the damping experiments. Thus some of the force went into accelerating the mass of the manipulator links. The experiment was performed under low acceleration ($< 0.5\frac{m}{s^2}$), in hopes to eliminate this effect, but apparently it was not eliminated completely. With the exception of this small quirk, the damping experiments were a success as they demonstrate the ability of the robot to exhibit the requested damping value.

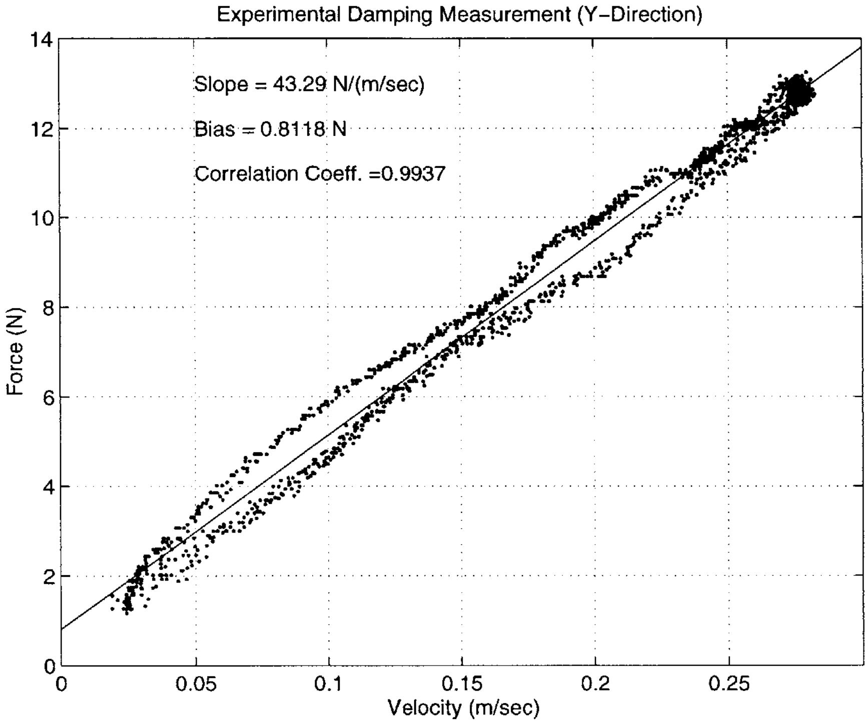

Figure 4-29: Actual Y-Damping: controller damping set at $40\frac{N}{\frac{m}{sec}}$ inherent damping approximated at $0.7\frac{N}{\frac{m}{sec}}$: Expected total damping $= 40.7\frac{N}{\frac{m}{sec}}$

Chapter 5

Conclusions

The main accomplishment of this thesis was the detailed characterization of the two degree of freedom MANUS2 robot. This characterization provided a qualitative evaluation of the performance of every component which makes up the system. The characterization also included the determination of the impedance limits of the robot and pointed out the likely causes of these limits.

The results of the impedance testing suggest that some important details be kept in mind when designing this type of robot. The discoveries made during the investigation of the impedance limits are the foundation of these suggestions. First, as many designers are aware, pure time delays are to be avoided. The research presented shows that delays on the order of $1msec$ are enough to significantly limit performance. It is easy to speculate that small time delays should cause no problems, but a careful investigation is worthwhile. Also, designers should be careful to avoid extra structural modes in their designs. This research showed that an unwanted structural vibration was a serious limitation on robot performance. If at all possible, the actuator shafts should be constructed of one continuous piece and not several segments joined by bolts. Another important note; if a design is implementing digital sensors, the higher the resolution the better. The resolution issue can often be deceiving. MANUS2 uses encoders with a resolution of 131072 $\frac{counts}{rev}$. This may seem like an extremely high resolution, but the experiments show that this resolution has a direct impact on Type 2 instability. The resolution of the sensor is especially important when using the position information to estimate the velocity. These issues were touched on in chapter 3, but more investigation as to the optimal method of filtering could certainly prove worthwhile.

Appendix A

Noise and Sensing: Effects of a PWM Amplifier on Position Sensing

Abstract

After several experiments, a solution to the sensing problem exhibited by the black robot has been uncovered. The solution in the end turned out to be the installation of a common mode choke on the outputs of the two three phase servo amplifiers. The common mode choke was able to reduce magnetically broadcast noise created by the high-energy Pulse Width Modulation (PWM) amplifiers. The magnetic broadcast had previously induced noise on sensor signals to unacceptable levels.

A.1 Introduction

The writer,s first task at the Newman Lab was to assess and conquer the sensing problems exhibited by the black robot, which Debo Adebiyi[1] referred to as the beta prototype. The robot will be refered to as just Beta for lack of a more descriptive

---

[1] Debo Adebiyi was a Master's Student in the Newman Lab. He designed and manufactured the beta prototype

name. Some preliminary experiments conducted by Debo and further experiments by the writer concluded that the sensor signals were being corrupted by noise.

This appendix discusses the possible sources of this noise and concludes with a solution to the noise problem. The objective of the appendix is to document what was done to overcome the noise problem. In this sense, it is important not only to discuss the solution, but also to explain the methods used to obtain that solution. This should save time in trouble shooting noise problems in the future.

A.2 Background

A few words on the status of the robot in January 1998, when this work began, appropriate at this time. The entire system is composed of two identical subsystems; one for the shoulder motion, and one for the elbow motion of the two-link manipulandum. For simplicity sake, the system will be referred to as a singular actuator and sensor package. The actuator package is composed of a Kollmorgen PAO8 power supply, and SEO6 3 Phase Servo amplifier as well as the Kollmorgen RBE 03013C frameless 3-phase DC motor. This Kollmorgen system is able to receive analog voltages from a digital to analog (D/A) card in the computer.

Figure A-1 is a diagram showing the connections between system components. The actuator was outfitted with a Teledyne Gurley optical encoder with 13bit/rev resolution A, B and index signals. These buffered sine outputs from the encoder were fed into a Teledyne Gurley interpolator with two types of output. The high-resolution (15-bit/rev) quadrature output is fed to a counter card designed and built by Paul Oppold[2]. This counter card uses a quadrature interpolation scheme to increase the resolution of the signal to 17 bit/rev. This 17 bit digital output of the counter is scanned by a digital input/output (DIO) card in the computer. The low-resolution (13 bit/rev) signals were output from the interpolator in the form of single ended digital A, B, and index signals. These signals were fed into an interface card designed

---

[2] Paul Oppold was an Undergraduate Research Opportunity Program (UROP) student in the Newman Lab

and built by Debo Adebiyi. The function of the interface card was to take the single ended signals and create the corresponding differential signals to be fed back to the amplifier for proper commutation.

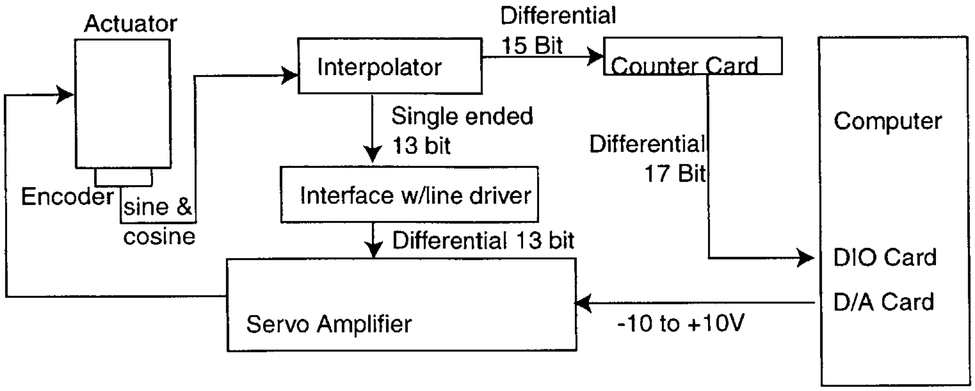

Figure A-1: Original layout of system components

The computer mentioned above is a Pentium with 100 MHz processor speed. It is the computer dubbed Emulator by the lab as it was originally used for controlling the Emulator. The D/A and DIO cards in the computer already had drivers written for them and this proved to be a time saver for Debo. Although a newer computer had been purchased, Debo used the Emulator computer to eliminate the need for creating new drivers for the cards in the new computer. At the same time, the new computer was being used to configure the Kollmorgen amplifiers. The amp has an EPROM on board which stores parameters concerning the desired performance of the drive system. Communication between the amp and the computer was executed via a serial connection using ServoStar software provided by Kollmorgen. The ServoStar software is a handy tool used in diagnosing problems with the system. The software allows the user to adjust critical parameters associated with the actuator and sensing package as well as operate the system in a velocity feedback mode. For example, the user may enter such parameters as the resolution of the encoder and the maximum velocity and current limits. In addition, the user may enter a velocity command and watch how the actuator reacts to the input both physically and on the monitor where the position and velocity information are displayed.

A.3 Original Problems

There were two major problems with the system that pointed to the possibility of noise corrupting the sensor signals. When using the ServoStar software to control the actuator, the following problem was observed: Upon receiving a moderate velocity command of 30 rpm, the actuator would often times ramp quickly to velocities above 400 rpm. In executing this action, the amplifier would violate either its maximum velocity or maximum current setting and shut down. This led one to believe that the feedback loop was disrupted in some way which caused an instantaneous step change in the position which in turn caused the drive to output maximum current. Although drawn out, this conclusion was reached in a logical manner. First, the assumption was made that the sensor signals were indeed corrupted with noise. This noise was observed using an oscilloscope and found to be spikes at regular intervals. A more adequate description of the noise signals will be discussed in the noise section of this document. The method the amplifier uses to read the position information is essentially the counting of spikes; the interpolator outputs a digital signal at a frequncies 8192 (13 bit) times the velocity in rpm (see figure A-1). The noise spikes superimposed on the actual signal could easily confuse the feedback loop of the amplifier.

This was not always the case; the drive would sometimes commutate correctly. The operator was able to observe that the actuator followed the commanded velocity via the read out on the monitor. When this was the case, one was led to believe that the feedback loop was intact; otherwise, the drive would not be able to commutate at a regulated velocity. Referring back to Figure A-1, this would indicate that the low-resolution loop of the feedback was intact and working correctly. With the low resolution loop intact, experiments were conducted to check the high-resolution information. It was then discovered that the output of the counter card was still corrupted. There were unexplainable jumps in the position information. Attempts were made to shield the signal wires, and even the entire interpolator, but shielding did not decrease the noise observed on any of the signal lines. In addition, the fact that the feedback loop from the encoder to the amplifier seemed undisturbed points to a problem down stream of the interpolator (i.e. in the counter card, see figure A-1).

A.4 Computer

The first change to the system was to set up the new computer to handle all the tasks associated with operating the robot. In this process it was decided to purchase different cards than those in the Emulator computer. This decision was made because the cards in the Emulator were lower performance and at higher cost than those which were purchased. One card purchased was a ComputerBoards card that has analog to digital (A/D), digital to analog (D/A), and digital input/output (DIO) capability. A counter card was also purchased from US Digital to replace the original. This choice was made because it was not certain whether the original counter was operating correctly, and it reduced the amount of external circuitry in the system. In addition, the counter card was highly recommended by Michel Lemay[3] who had used another version of this card for reading encoders on his two-link manipulandum.

After purchasing the new cards, new drivers were written so that they could be used in the QNX operating system. QNX has become the standard in the Newman lab as it has proven to perform the best for real-time control. These drivers were completed and then some simple tests demonstrated they were working properly. The purchase of the new cards coupled with the development of the drivers allowed for the robot to be controlled by just one computer. Previously, the windows (i.e. Kollmorgen ServoStar) software was on one machine, and the QNX software was on another.

---

[3] Michel Lemay was a Post Doctoral student in the Newman Lab. He worked extensively with two link manipulandums similar to the beta prototype.

A.5 Hardware

After the computer was set up with the new cards functioning, the previous problems were reduced to the following: The index signal was corrupted with noise that caused inadvertent indexing. At the same time, the A and B signals were corrupted with similar noise but did not seem to be producing incorrect readings. This meant that the incremental position information was available, but absolute position could not be measured. After referring to *The Art of Electronics*[4] for techniques on reducing noise, it was decided that the signal circuitry should be rewired. The text emphasizes the use of low impedance wiring especially large low impedance grounding-planes as well as the use of twisted pair wiring for signal pairs. This called for the rewiring of the interface card mentioned earlier. This task was needed regardless of noise problems, as the original interface card was designed for only one drive system, and the robot required two separate drive systems. This reference to the text did however allow for the upgrade of the card during the rewiring. The new interface card incorporates a large low impedance grounding-plane and low impedance twisted pair wiring.

In addition to the new interface card, all the signal cables were remade. The new cables use the twisted pair technique mentioned above.

A.6 Noise

All the work done on the hardware was well justified, yet it provided no significant change in the noise level on the index signal. This noise was recorded via an oscilloscope and a digital camera and is displayed in Figure A-2 below. This noise was measured by simply connecting the scope leads across the ground and index wires where they exit from the encoder. This 2 volt zero to peak noise is astounding, when considering that the index signal output from the encoder is only 0.7 volts zero to peak. Note that the trace shows no evidence of the actual index signal. This is because it is difficult to take a picture of the scope at the exact moment in time when

---

[4] Paul Horowitz and Winfield Hill, *The Art of Electronics*, Second Edition (Cambridge University Press, 1989)

the index bit fires.

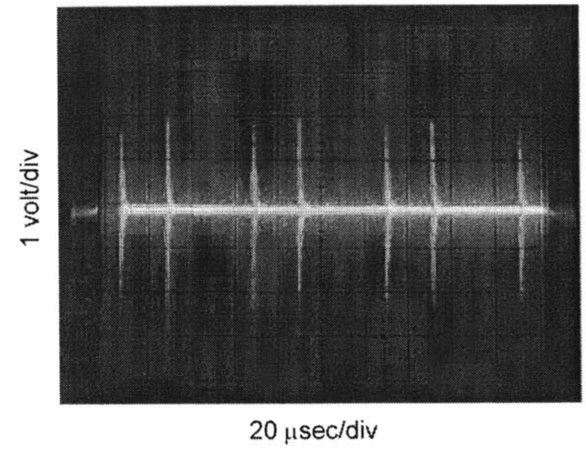

Figure A-2: Illustrates the noise on the index signal under the original setup

At this point, it is necessary to explain another measure that was taken in an attempt to reduce the noise on the index signal. First, refer to Figure A-3 below to see how the power and ground wires were routed in the original system. Notice that the AC power supplying the servo amplifier is also directly connected the DC power supply, which supplies all the signal circuitry with power. This gave rise to the idea that the servo amplifier may be corrupting the AC power upstream of itself. This of course means the DC power being supplied to the signal circuitry may be corrupted. This was exactly the case. The scope leads were attached across the +5 volt and ground wires where they exit from the encoder and the noise was measured. The trace, shown in Figure A-4 below, is quite similar to that seen in Figure A-2. This was promising as it pointed to the possibility of using a filter to reject noise in the AC power supplying the DC power supply in turn decreasing the noise on the 5 volt supply to the encoder. Refer to Figure A-5 to see the change in position of the RFI filter in the system.

Unfortunately, this change with the filter had no effect on the noise. Needless to say, this was both baffling and discouraging, but with a little more thought, the following hypothesis was conceived.

Hypothesis: The servo (switching) amplifier creates large magnetic fields as a byproduct of the large pulse width modulated (PWM) currents. These magnetic

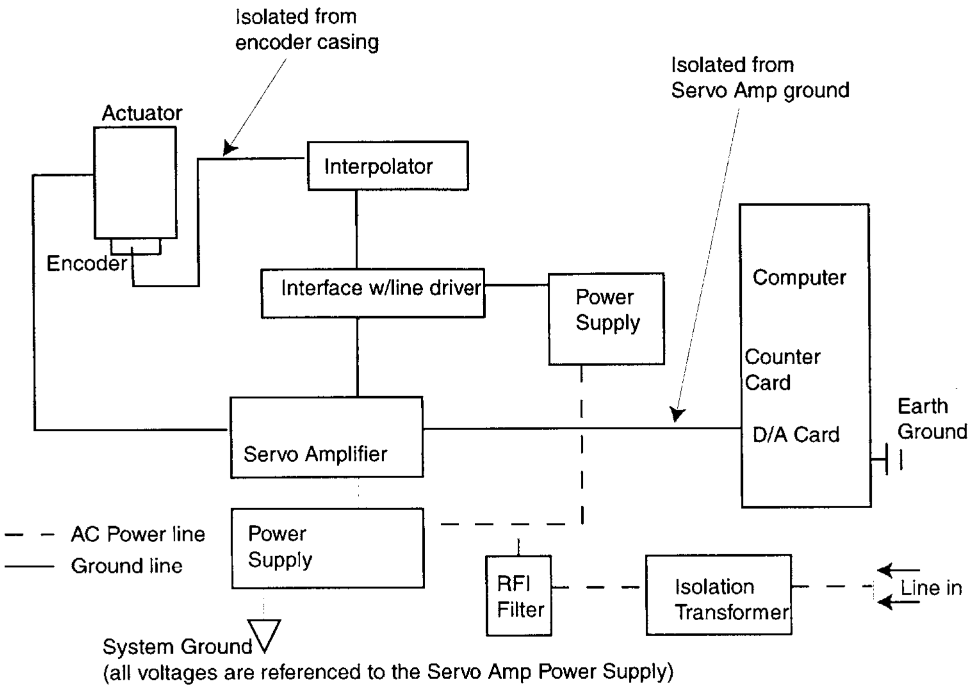

Figure A-3: This figure shows the original ground and power connections

fields induce current (and therefore noise) on all closed loops in the system.

Any two wires traveling between any two components of the system could pick up the noise. One component acts as the transmitter of the signal and the other acts as the receiver. Of course, the assumption is that the transmitter does not have infinite output impedance and that the receiver does not have infinite input impedance. Thus any such connection makes a closed loop whether the two wires are supplying power or sending a signal. This is why the noise looks the same on the power supplied to the encoder as it does on the encoder's output (e.g. the index signal). The area enclosed by the loop is the dominant factor.

Looking back to Figure A-2, this noise signal can now be looked at more carefully. Notice that the signal appears in groups of two spikes. Consider the possibility that this group of two spikes is one cycle of a signal. Measuring the distance between the start of one cycle to the start of the next cycle, the elapsed time or period of the cycle is T $\approx$ 60 to 65 μsec. Using $f = \frac{1}{T}$, we get a frequency of f $\approx$ 15.4 to 16.6kHz. Thus, it is very likely that the group of two spikes does represent the PWM frequency,

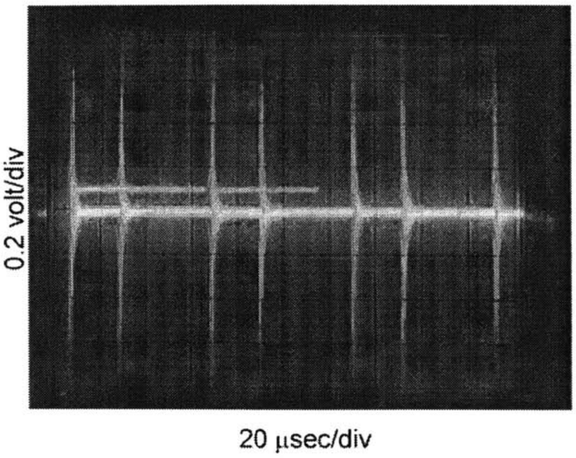

Figure A-4: Noise on encoder power under the original setup

which is 16kHz. The first of the two spikes is the rising edge, and the second is the falling edge of the PWM square wave. Each edge perturbs the system and the system settles quickly before the next edge perturbs it once again. Depending on the current demand, the time elapsed between rising and falling edges changes. On the contrary, the time between two leading edges is fixed, and this is the PWM frequency. This was enough evidence to pursue this hypothesis further.

If this new hypothesis were true, the RFI filter would have no effect. In fact, the experiment, which verified that magnetic coupling was taking place, demonstrates the inability of the RFI filter to decrease this type of noise. The experiment was set up as follows. An external DC power supply was plugged in on a separate circuit of the building power to assure that the AC supply of the robot was not coupled to the DC supply. A small load (50 Ω resistor) was driven with this power supply at 5 volts. This experiment was set up to simulate powering the encoder, which requires a 5 volt supply and draws around 100 mA. When connecting the scope leads across the load powered by the external supply, a noise signal was observed. This noise signal was nearly identical to that seen in Figure A-2. This shows that filtering of the AC power upstream of the DC supply will have no effect on reducing this magnetically coupled noise experienced at the encoder. What's more, this shows that a simple system with no ground loops can be affected by magnetic coupling. Remember that in order for voltage spikes to show up across the resistor, as in this experiment, a

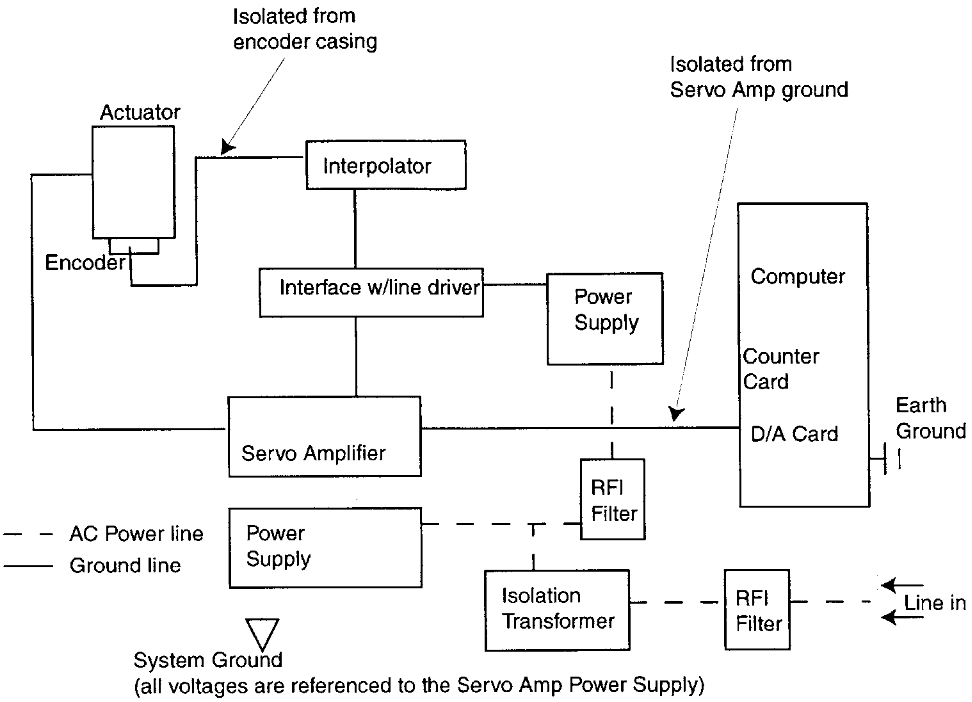

Figure A-5: Modified ground and power connections. Note: The actuator is constructed in the delta configurtion.

current must be induced. And, in order for a current to be induced, a loop must be present. The loop in this case was that created by connecting the resistor across the leads of the DC power supply. This creates a closed loop because the power supply does not have infinite output impedance. It could be argued that the loop created by the scope and the resistor is that in which the induced current appears. This is highly unlikely because the input impedance of the scope is 1MΩ/20pF. To further reduce this effect, the scope leads were twisted reducing the area enclosed by the scope/resistor loop nearly to zero. The noise was then clearly being induced on the larger loop, which was demonstrated as reducing or increasing the area enclosed by the DC power supply/resistor loop changed the noise level.

This led to another simple experiment involving just the scope and a 50 ohm resistor. The resistor was clipped between the two scope leads that created a small loop in which current could be induced. In this experiment, the scope leads were not twisted as some area was needed to induce current. In this case, the loop enclosed approximately the area of a $2\frac{1}{2}$ inch diameter circle. This loop could then be held in the vicinity of different parts of the system to identify the areas broadcasting the most noise. Figures A-6 through A-9 below show noise measured using this technique at several different locations in the system. This information is difficult to quantify as the information displayed is the voltage level corresponding to a current induced on a loop external to the system. However, it is true that the voltages measured are strongly correlated to the currents in the system as the current is creating a magnetic field, which in turn induces the current on the oscilloscope/resistor measurement device.

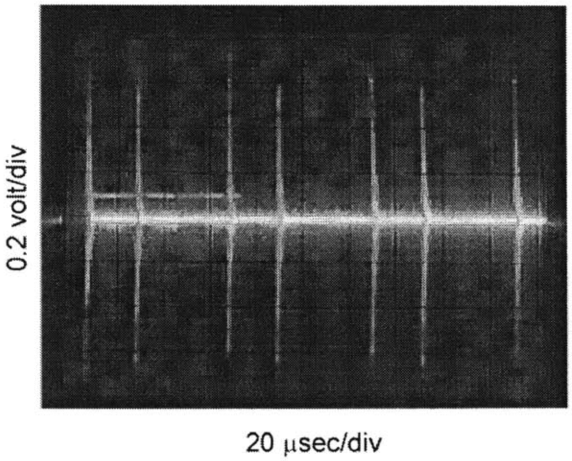

Figure A-6: Noise at Servo-Amp Output

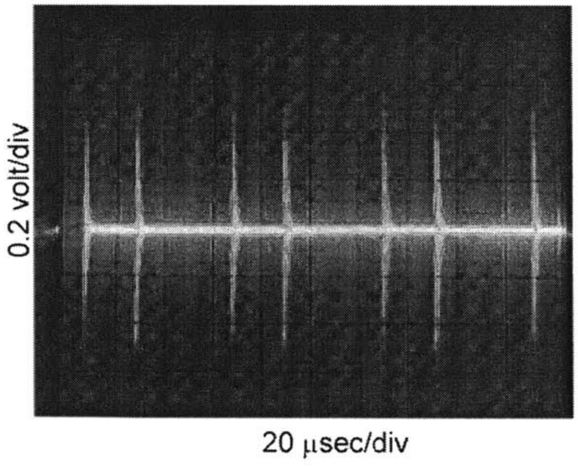

Figure A-7: Noise along Servo-Amp to Motor Power Cable

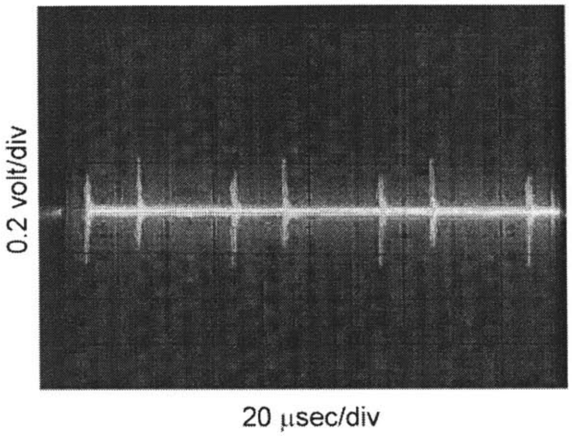

Figure A-8: Noise at Actuator

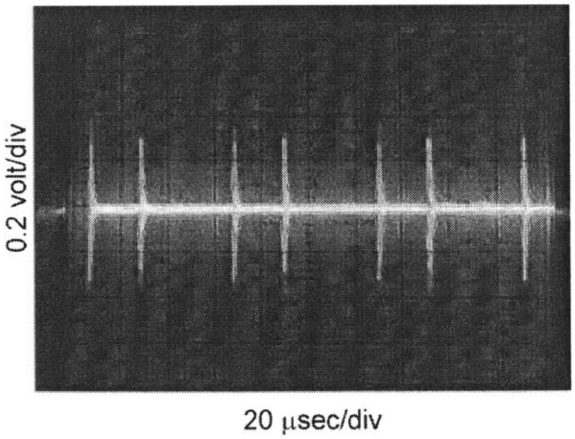

Figure A-9: Noise along Actuator to Interface-Card Cable (Carries all feedback signals from actuator to interface-card)

A.7 The Filter

As the signal wiring had been completed using the twisted pair wiring described earlier, there was little possibility to further reduce the area enclosed by any closed loops in the system. The fact that the cable transmitting power to the actuator was a major contributor to broadcast noise, eliminated the possibility of moving the source further away from the signal circuitry. This left but one alternative, filter the output of the amplifier to reduce noise generated by the pulse width modulation. After all, the PWM frequency is 16 kHz, which is well above the bandwidth of the actuator. What's more comforting is that the power sent to the motor is three phase, but just one PWM signal creating noise. This means that the noise is present at the same frequency and phase angle on all of the three lines while the three intended signals have 120° phase difference relative to one another. This type of noise is called common mode noise and can be combated using a common mode filter sometimes called a common mode choke.

After some discussion with Kollmorgen engineers, a Schaffner common mode choke (Part # RD7137-36-0M5) was selected. This choke design starts with a ferrite toroid. Ferrite is a metal with a very high magnetic permeability. Around this common core three separate conductors are wrapped, one for each of the three phases. The coils of each conductor cover one third of the toroid's surface with no overlap. The filter is connected to the system such that positive current in each individual phase travels in the same direction around the toroid. Figure A-10 below shows a simplified model of the filter and the signals that pass through it.

The inductance pointed out in Figure A-10 is due in large part to the current attempting to induce a magnetic field in the high permeability ferrite core. When considering the three phase power, the essence of the filter becomes evident. The three phases are 120° apart; that means the net (sum of the three phases) current at any point in time is zero. To the filter, this means that no magnetic field is being induced, and therefore the filter offers little inductance to the intended three phase power. In fact, according to Schaffner engineers, the inductance realized by the three

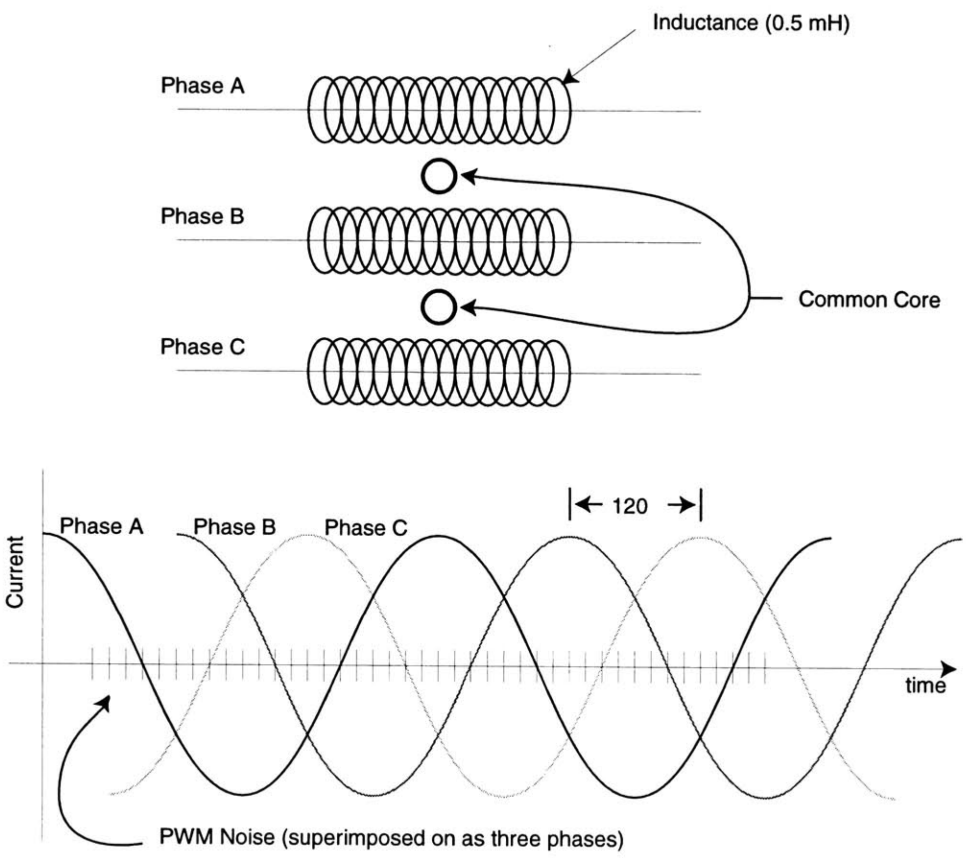

Figure A-10: Filter Model and 3 Phase Signals

phase power is the value given in the data sheet (0.5mH; the actual inductance along a single conductor in the filter). The PWM noise on the other hand is at the same phase on all three of the lines. Thus, it induces a magnetic field in the ferrite core and the filter acts as a large inductance. According to Schaffner engineers, the inductance realized by such "common mode" signals is on the order of 100 times (i.e., 50 mH) the value given in the data sheet.

Now the results: Figure A-11 shows the noise measured on the index signal with the filter in place. Compare this to the noise seen in Figure A-2, but keep in mind the scales are different for each signal. The noise has been reduced from around 2 volts zero-to-peak to about 0.3 volts zero-to-peak. This is quite nice. Now look to Figure A-12 (compare to Fig. A-4) to see how the noise on the encoder power has been reduced as well. Figures A-13, A-14, A-15 and A-16 are measures of noise recorded using the scope and resistor as mentioned before. These figures show noise broadcast levels in the system with the filter in place and can be compared to their non-filtered counterparts in figures A-6, A-7, A-8, and A-9.

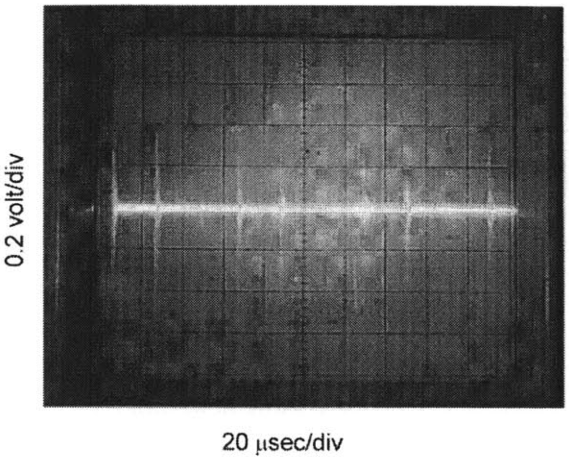

Figure A-11: Noise on index signal with the filter installed

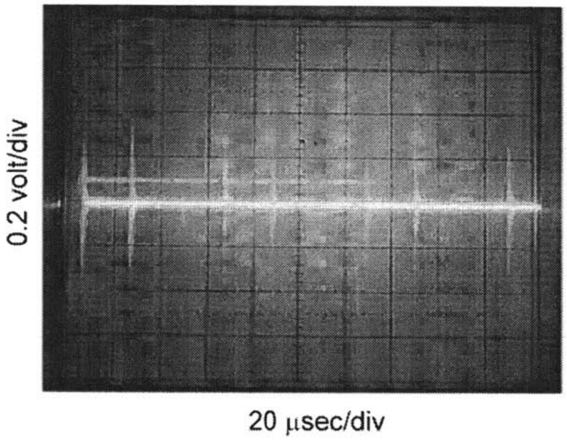

Figure A-12: Noise on encoder power with the filter installed

Figures A-2 and A-11 are probably the most important since these measurements are easier to quantify. The scope is actually connected across the index signal and ground wires of the encoder. In comparing these plots, the improvement is around a factor of 6 to 7. This is respectable, but further improvement is certainly more desirable. Schaffner does make other models of this common mode choke, and other models would attenuate the noise even further. The difference would be that the conductors would be of a much smaller gage thus increasing both the inductance and the resistance of the filter. The conductors in the model currently installed are 10 gage.

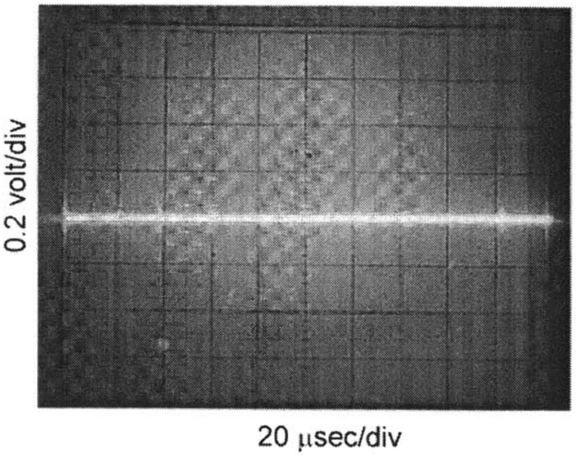

Figure A-13: Noise at Servo-Amp Output (with filter)

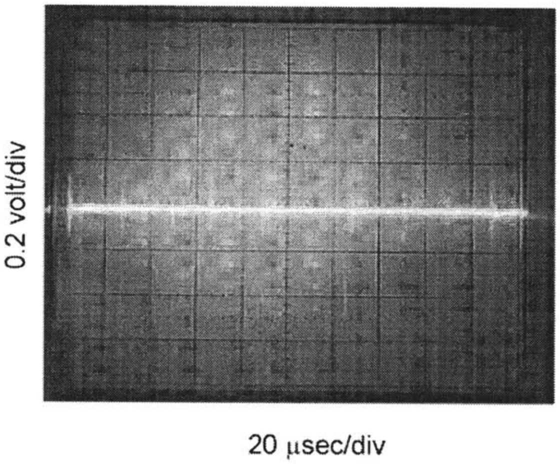

Figure A-14: Noise along Servo-Amp to Motor Power Cable (with filter)

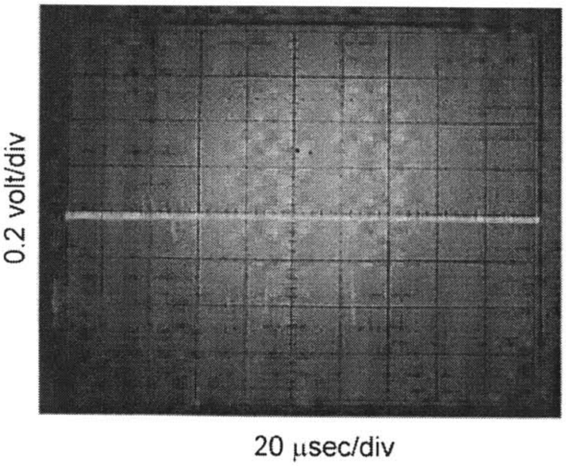

Figure A-15: Noise at Actuator (with filter)

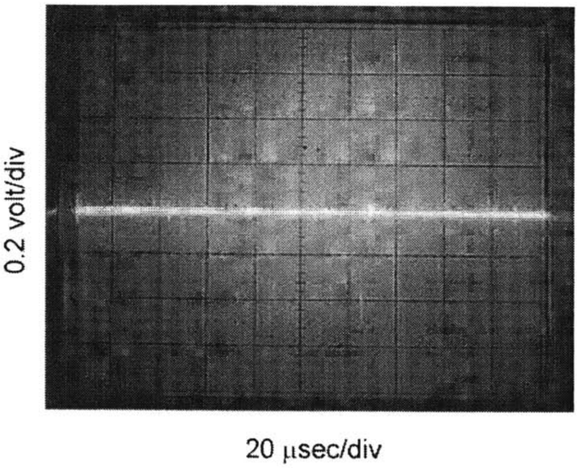

Figure A-16: Noise along Actuator to Interface-Card Cable with filter installed (Carries all feedback signals from actuator to interface-card)

Measuring the resistance of this model from the input to the output of one phase, the value is R_F=2.75mΩ and as displayed in Figure A-10, the inductance is L_F=0.5mH. In considering models with better attenuation, values upwards of R_F=60mΩ and L_F=12mH would be encountered. So, the issue is to discover the maximum values of R_F and L_F that can be encountered without negative effects on the performance of the system. Of course, this would require an analytical model and possibly some experiments. The filter being used was chosen because it has the lowest available values for R_F and L_F and thus the least likely chance of having negative effects on the system. A speculation is that the values of R_F and L_F will need to remain much lower than the values for the motor winding resistance and inductance which are R_M=7.7Ω and L_M=27mH respectively. Therefore, it may be possible to achieve higher attenuation without disrupting performance.

As previously mentioned, the filter is designed to have little effect on the intended three phase signals. Kollmorgen engineers assured that the filter would not have an effect on the bandwidth of the amplifier.

A.8 Analytical Model

As mentioned in the previous section, an analytical model would be very useful in understanding exactly what is going on in the system. It is important to verify that the filter is functioning in the desired manner. The filter should not affect the dynamics of the system (i.e. the bandwidth). A means of checking the filters effect on the system is the construction and manipulation of an analytical model. This model would include the amplifier, the filter, the motor, and possibly some load.

To this point, no model has been derived, but some thought has been afforded to this idea. There are some issues that must be understood in order to create the model. First, the filter acts differently for common mode and non-common mode signals. Also, the fact that the amplifier is a three phase source, and that the motor is a three phase load, complicates things even more. Techniques for reducing three phase systems to single phase equivalents do exist; however, in this case, reduction is not possible because the filter requires the three separate phases to fully describe its function. At this point, more research will need to be done before a model can be developed.

A.9 Open Loop Control

The data in this section will demonstrate that the system is commutating correctly and that feedback signals are indeed sent back to the control computer with no corruption.

After lowering the noise level, some simple experiments were completed to demonstrate that the system was working correctly. In the first experiment, an analog voltage of 0.2 Volts was sent to the servo amp that in turn generates a corresponding constant current (0.10 amps in this case). This constant current should correspond to a constant torque at the actuator for the duration of the five second test. The test was completed for both positive and negative angular displacement. The following plots show the results of this test in the positive direction:

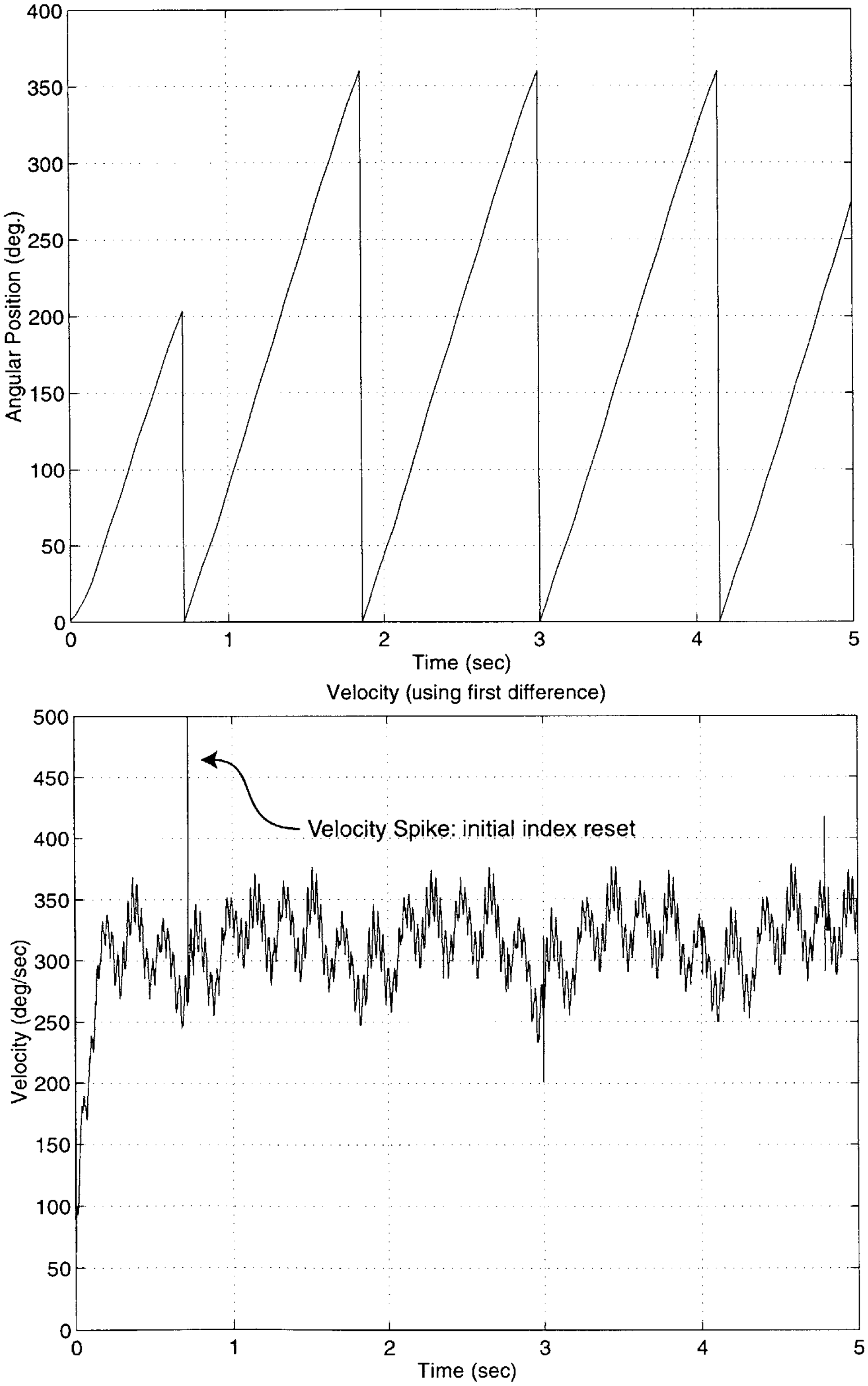

Figure A-17: Angular Displacement and Velocity (input of 0.2 V DC)

Notice, in the displacement plot, that the actuator does not complete the first full revolution before the position resets. This is because upon startup, the counter is reset, and then the counter is reset again when it sees the index pulse. After the index pulse has been triggered, the position measurements are absolute. Next notice the noise on the velocity signal. Upon examining this noise, three frequencies become apparent. One vibration component at one cycle per revolution is most likely due to some form of mechanical friction that is position dependent. The second component at 6 times per revolution is the ripple torque effect seen in most brushless drives. And the third component at 39 times per revolution is due to cogging. Cogging is a function of how many teeth or cogs there are in the motor. This motor has 39 cogs and the permanent magnets have an attraction to the cogs.

Appendix B

Force Transducer Calibration

During the course of the many experiments conducted for this thesis, a six axis force transducer was used. The ATI Gamma FT3733-30/100 transducer was chosen for the experiments requiring force or torque measurements. The experiments conducted in this thesis required only three of the six available axes, and therefore only these three axes were calibrated. Static calibrations were completed for the z torque axis as well as the x and y force axes. An additional experiment was conducted to determine if the response of the transducer exhibited any time delay.

B.1 Static Calibration

B.1.1 Z Torque Axis

Torques of known magnitude were applied to the transducer using a lever arm and calibrated weights. First, the transducer was mounted with the xy-plane oriented vertically. The lever arm was rigidly attached to the force transducer and the weights were hung from a hole drilled in the lever arm. The distance between the center of the hole and the center of the transducer was measured using calipers and was known within +/- 0.005". Figure B-1 summarizes the results of this calibration experiment. Note: the sensing range for torque in the z-direction for this transducer is -100 to 100 in.-Lbs.

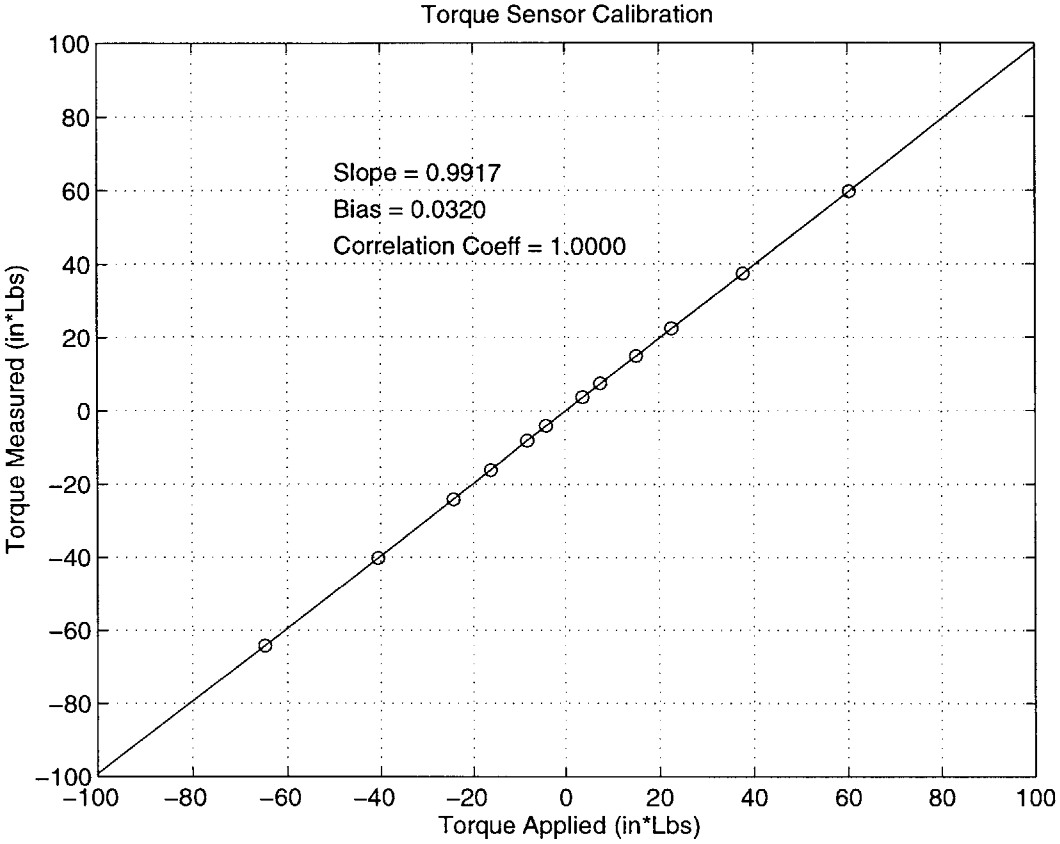

Figure B-1: ATI Force Transducer Calibration: Z Torqe axis

B.1.2 X and Y Force Axes

Much like in the torque experiment, calibrated weights were used to apply known forces to the transducer. The transducer was first mounted with the x-axis oriented vertically. Weights ranging from 3 to 21 Lbs. were then applied creating force in the positive x-direction. This process was repeated for the negative x-direction as well as both the positive and negative y-directions. The results for both directions came out exactly the same, and are summarized in B-2. Note: The sensing range for forces in the x and y-directions is -30 to 30 Lbs.

B.2 Dynamic Calibration

The final force transducer calibration experiment was designed to determine if there was any time delay between the actual force being applied and the force recorded

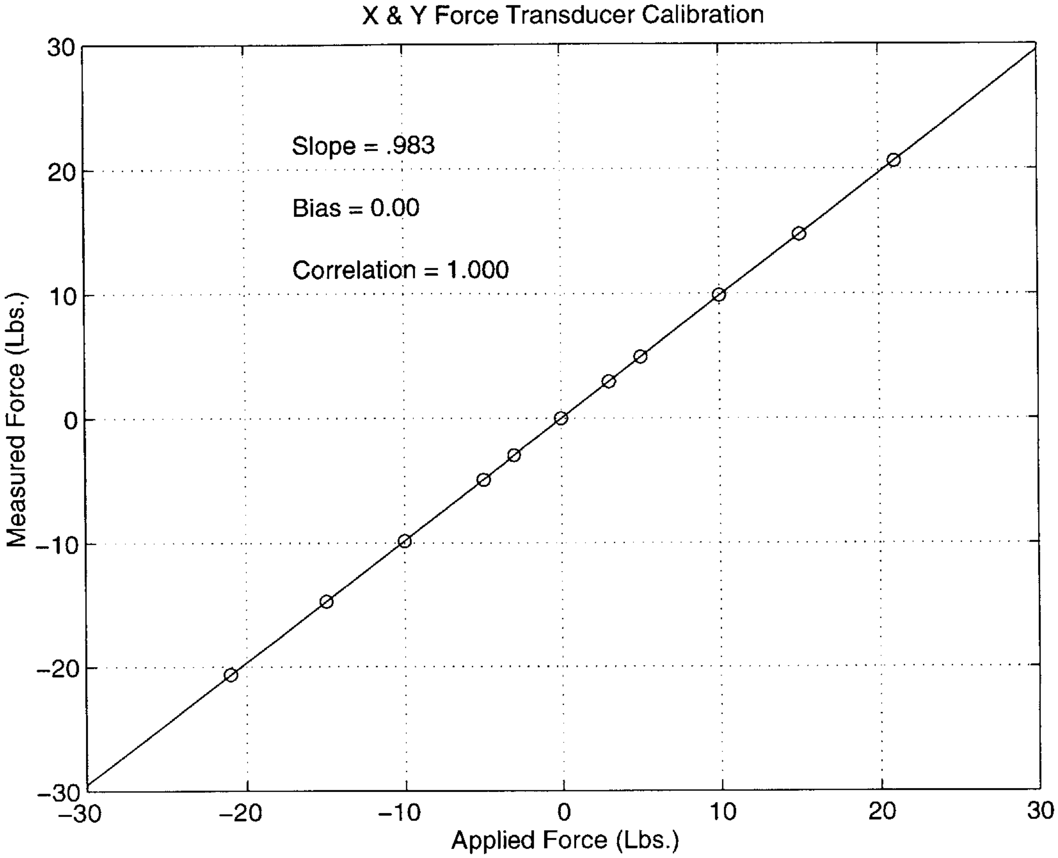

Figure B-2: ATI Force Transducer Calibration: X and Y Force Axes

using the force transducer. To accomplish this, the force transducer was mounted on the endpoint of the robot. The position sensors in the robot allow for the coordination of an event involving both position and force. In this case, the event chosen was an impact event. The idea was to move the arm of the robot such that the endpoint contacted a rigid surface. To create a solid surface for the force transducer to contact, a block of aluminum was mounted to the table. With position and force being recorded simultaneously, the sharp changes in position upon impact should correspond with peaks in the force. The forces and the displacements were all recorded at 1000 Hz during this experiment. Figure B-3 illustrates the time history of this experiment.

It appears that the spikes in force do indeed correspond with the peaks in position. Figure B-4 shows a close up view of the time history during the impact of the force transducer with the surface. This plot demonstrates that there is no delay in the force transducer as the force spike corresponds with the earliest peak in position. The table

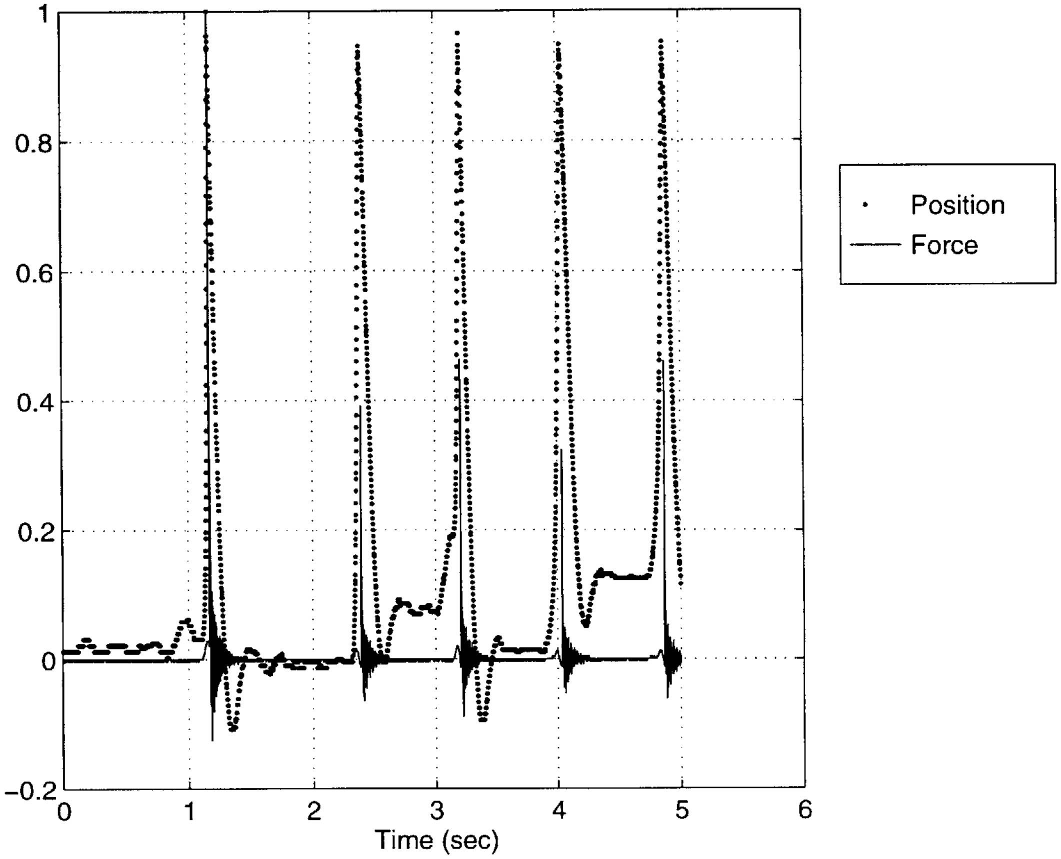

Figure B-3: ATI Force Transducer Calibration: Dynamic Response

below indicates the times of peak position and peak force for all five impacts recorded in this test. All but one of the force peaks correspond to the position peaks. This again is strong evidence that there is indeed no delay in the force transducer.

Time of Peak	
Position	Force
1.169	1.169
2.398	2.399
3.208	3.208
4.037	4.037
4.868	4.868

Table B.1: Times of peak position and peak force

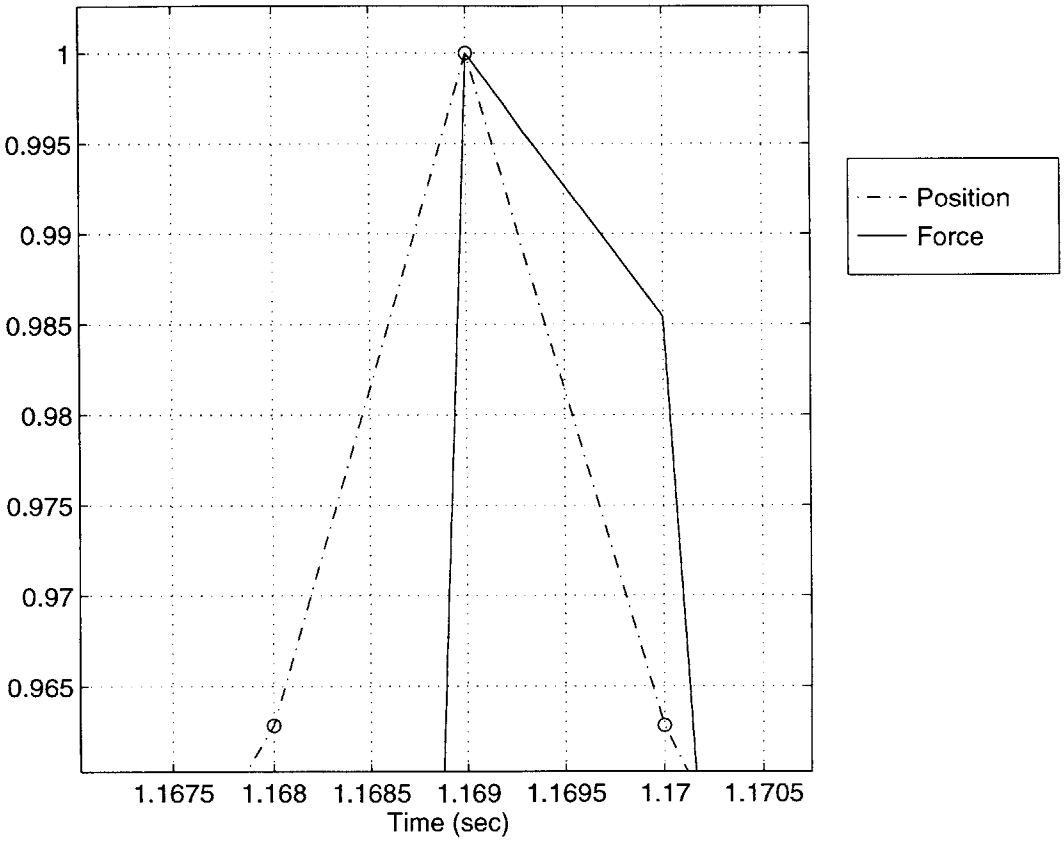

Figure B-4: ATI Force Transducer Calibration: Dynamic Response (Close up)

Appendix C

Adaptive Control: A Physical Implementation

Abstract

The purpose of this paper is to report the discoveries made during the implementation of an adaptive controller on a physical system. An adaptive controller was designed and implemented on a two degree of freedom manipulator. Some modeling assumptions were made, and the implications of these assumptions are discussed. The performance of the adaptive controller is also discussed. The parameter estimates from the adaptive controller are shown to converge more quickly with more complex trajectories. Furthermore, the parameter estimates agree with those obtained in the System Identification section of this thesis.

C.1 Dynamic Model & Adaptive Controller

C.1.1 Dynamic Model

This section gives an overview of the dynamic modeling of the manipulator system and the design of the adaptive controller.

Two major modeling assumptions were made. First, the four-bar-linkage was modeled as a simple two link assembly as shown in figure C-1. Next, the dynamic model does not account for any viscous damping or coulomb friction at the joints. This second assumption follows with that of Slotine and Li [1] in their case study involving a two degree of freedom manipulator.

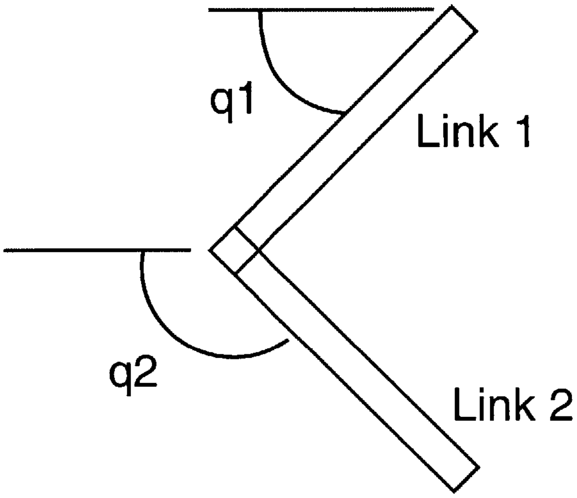

Figure C-1: The 4-Bar-Linkage was treated as a simple 2-Link Mechanism

Using these two modeling assumptions, the following dynamic equations of motion can be derived for the two link manipulator using absolute joint angles.

$$\tau_1 = (m_1c_1^2 + I_1 + m_2l_1^2)\ddot{q}_1 + (m_2l_1c_2\cos(q_2 - q_1))\ddot{q}_2 - m_2l_1c_2\sin(q_2 - q_1)\dot{q}_2 \qquad (C.1)$$

$$\tau_2 = (m_2l_1c_2\cos(q_2 - q_1))\ddot{q}_1 + (m_2c_2^2 + I_2)\ddot{q}_2 + m_2l_1c_2\sin(q_2 - q_1)\dot{q}_1 \qquad (C.2)$$

Where I_j denotes inertia of a link, l_j is the length of the link, c_j is the distance from the joint to the center of mass of the link, and m_j is the mass of the link.

---

[1] **Slotine, J.-J. E. and Li, W.**, Adaptive Control, A Case Study, *I.E.E.E Transactions on Automatic Control*, Vol. 33, No. 11, November 1988

C.1.2 Controller Design

For the design of the adaptive controller, the equations of motion will be written in the form of an unknown parameter vector a and the matrix $\mathbf{Y}$ which is independent of the unknown parameters. From the equations of motion, three unknown parameters can be identified.

$$a_1 = m_1 c_1^2 + I_1 + m_2 l_1^2 \tag{C.3}$$

$$a_2 = m_2 l_1 c_2 \tag{C.4}$$

$$a_3 = m_2 c_2^2 + I_2 \tag{C.5}$$

Thus, $a = [a_1 \; a_2 \; a_3]^T$

Also coming directly from the equations of motion is the definition of the $\mathbf{Y}$ matrix. The components of $\mathbf{Y}$ are shown below.

$\mathrm{Y}_{11} = \ddot{q}_{1r}$

$\mathrm{Y}_{12} = \cos(q_2 - q_1)\ddot{q}_{2r} - \sin(q_2 - q_1)\dot{q}_{2r}^2$

$\mathrm{Y}_{13} = 0$

$\mathrm{Y}_{21} = 0$

$\mathrm{Y}_{22} = \cos(q_2 - q_1)\ddot{q}_{1r} + \sin(q_2 - q_1)\dot{q}_{1r}^2$

$\mathrm{Y}_{23} = \ddot{q}_{2r}$

$$\mathbf{Y} = \begin{bmatrix} Y_{11} & Y_{12} & Y_{13} \\ Y_{21} & Y_{22} & Y_{23} \end{bmatrix}$$

Where $\dot{q}_r = \dot{q}_d - \mathbf{\Lambda}\tilde{q}$ and Λ is a positive definite diagonal 2 × 2 matrix. This $\dot{q}_r$ is the "reference velocity" and is based on the desired velocity $\dot{q}_d$ and the tracking error $\tilde{q}(t) = q(t) - q_d(t)$.

Note:

$$\mathbf{\Lambda} = \begin{bmatrix} \Lambda_1 & 0 \\ 0 & \Lambda_2 \end{bmatrix}$$

Having defined the **a** vector and the **Y** matrix, the adaptation law can be written as suggested by the course text [2].

$$\dot{\hat{a}} = -\mathbf{\Gamma}\mathbf{Y}^T s \tag{C.6}$$

$$\mathbf{\Gamma} = \begin{bmatrix} \Gamma_1 & 0 & 0 \\ 0 & \Gamma_2 & 0 \\ 0 & 0 & \Gamma_3 \end{bmatrix}$$

Where $\mathbf{\Gamma}$ is the positive definite diagonal matrix above, and the vector s is a measure of the tracking acurracy and is defined as

$$s = \dot{q} - \dot{q}_r = \dot{\tilde{q}} + \mathbf{\Lambda}\tilde{q}. \tag{C.7}$$

Likewise, the course text suggests the following control law.

$$\tau = \mathbf{Y}\hat{a} - \mathbf{K_D}s \tag{C.8}$$

Where K_D is a positive definite diagonal gain matrix.

$$\mathbf{K_D} = \begin{bmatrix} K_{D1} & 0 \\ 0 & K_{D2} \end{bmatrix}$$

Because the vector a and the matrix $\mathbf{Y}$ have been defined, control law can be written explicitly in the form of the following two equations:

$$\tau_1 = Y_{11}\hat{a}_1 + Y_{12}\hat{a}_2 - K_{D1}s_1 \tag{C.9}$$

---

[2] Slotine, J.-J. E. and Li, W., **Applied Nonlinear Control**, Prentice Hall Inc., New Jersey, 1991.

$$\tau_2 = Y_{22}\hat{a}_2 + Y_{23}\hat{a}_3 - K_{D2}s_2 \tag{C.10}$$

The above adaptation and control laws can be implemented on the manipulator system via the computer and the C++ software mentioned earlier. The specifics of the software are not necessary for understanding how the experiment was conducted and are therefore not mentioned in this paper.

C.2 Experimental Results & Discussion

For all of the experiments performed, the same strategy was followed. This strategy was to use the first second of a five second trial to move the endpoint of the manipulator to the center of the workspace ($q_1 = 0.464$ rad., $q_2 = 2.409$ rad.). Then the remaining 4 seconds of the trial were used to implement a sinusoidal trajectory.

For both of the trajectories described below the following parameters were set in the adaptive controller:

$$\begin{aligned} \Gamma_1 &= 0.2 \quad \Gamma_2 = 0.2 \quad \Gamma_3 = 0.5 \\ \Lambda_1 &= 5.0 \quad \Lambda_2 = 5.0 \\ K_{D1} &= 5.0 \quad K_{D2} = 5.0 \end{aligned}$$

The Γ_j were selected by maximizing parameter convergence during the complex trajectory discussed below. The Λ_j and the K_{Dj} were chosen by increasing their values as long as no instability was observed. In this case, instability arose in the form of high frequency vibration (on the order of 200 Hz) when the Λ or K_D parameters were set too high.

C.2.1 Parameter Convergence

At first, a fairly benign trajectory was selected to observe that adaptation was taking place. This benign trajectory was defined by the equations presented below (angles are in radians). This trajectory is requesting that the joint angles of the robot follow sinusoidal paths at a frequency of 0.5 Hz and amplitude of 0.1 rad.

$$q_{d1} = 0.464 - 0.1(1 - \cos(\pi t)) \tag{C.11}$$

$$q_{d2} = 2.409 + 0.1(1 - \cos(\pi t)) \tag{C.12}$$

Figures C-2 and C-3 show the tracking errors, command torques, and the parameter estimates for this trajectory. From the plots, the tracking errors (± 0.2 rad.) remain low which indicates that the controller is working properly. Also, the parameters are changing, which suggests that they are indeed being updated in attempt to reduce the tracking error. As expected, the parameters do not converge to constant values at any point during the trial. This is expected because the trajectory is not complex enough to require the parameters converge to their actual values.

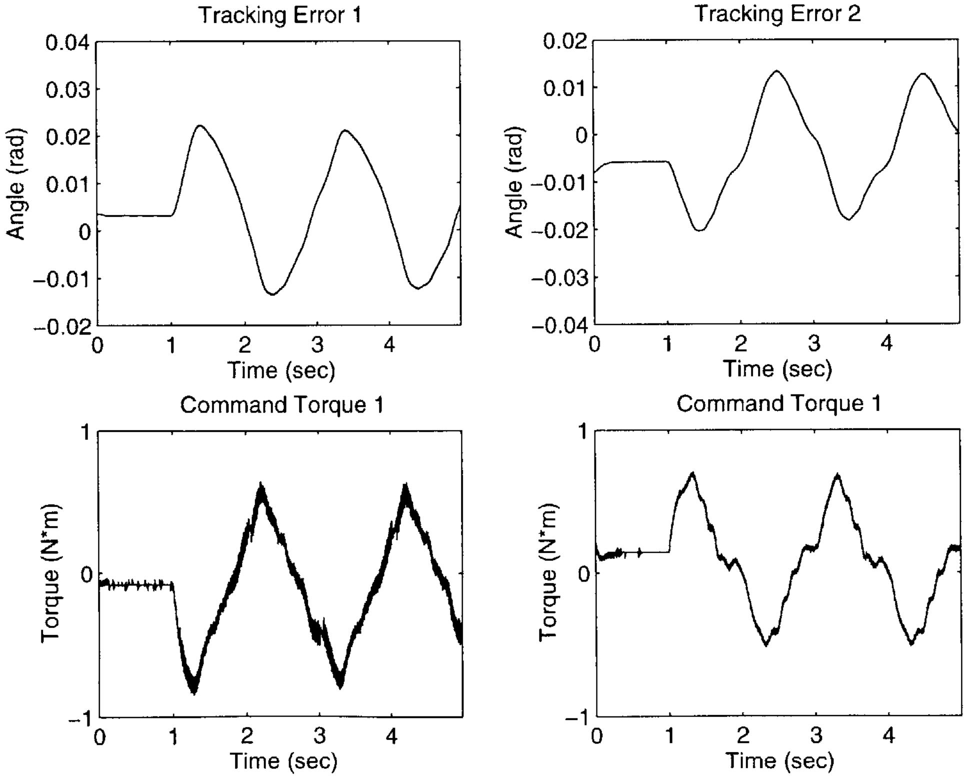

Figure C-2: Tracking errors and Command Torques during a benign trajectory

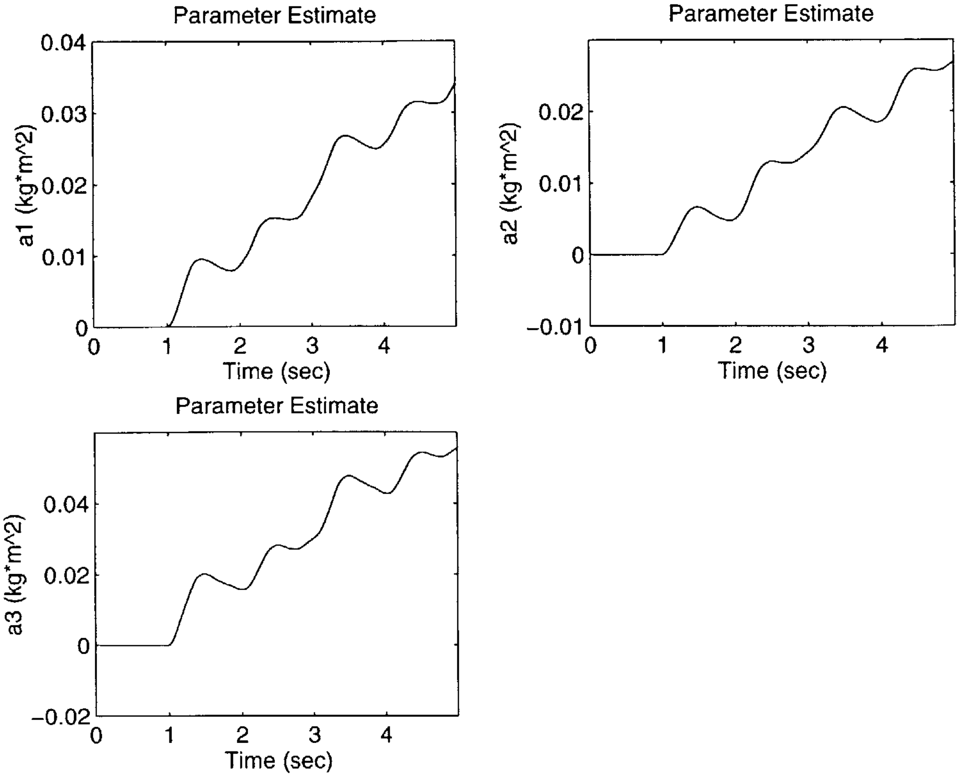

Figure C-3: Parameter Estimates during a benign trajectory

Next, a more complex trajectory was implemented to see if the parameters would converge to their actual values. In this trajectory, the frequency was increased to 2 Hz for q_1 and 1 Hz for q_2 while the amplitudes were 0.1 rad. and 0.2 rad. respectively.

$$q_{d1} = 0.464 - 0.1(1 - \cos(4\pi t)) \tag{C.13}$$

$$q_{d2} = 2.409 + 0.2(1 - \cos(2\pi t)) \tag{C.14}$$

The results for this "complex" trajectory are shown in figures C-4 and C-5. This tracking error is somewhat higher than expected, but ± 0.03 rad. is still reasonably small. The parameters are changing more rapidly at the onset of the trajectory than at the end which indicates that they indeed are converging. There is some oscillatory behavior and possibly some drift to the parameter estimates. These problems undoubtedly arise from one or more of the many sources of error in this experiment.

These sources of error will be addressed later.

This section has shown that with more complex trajectories, the parameters do converge, and that the adaptive controller has generally good behavior.

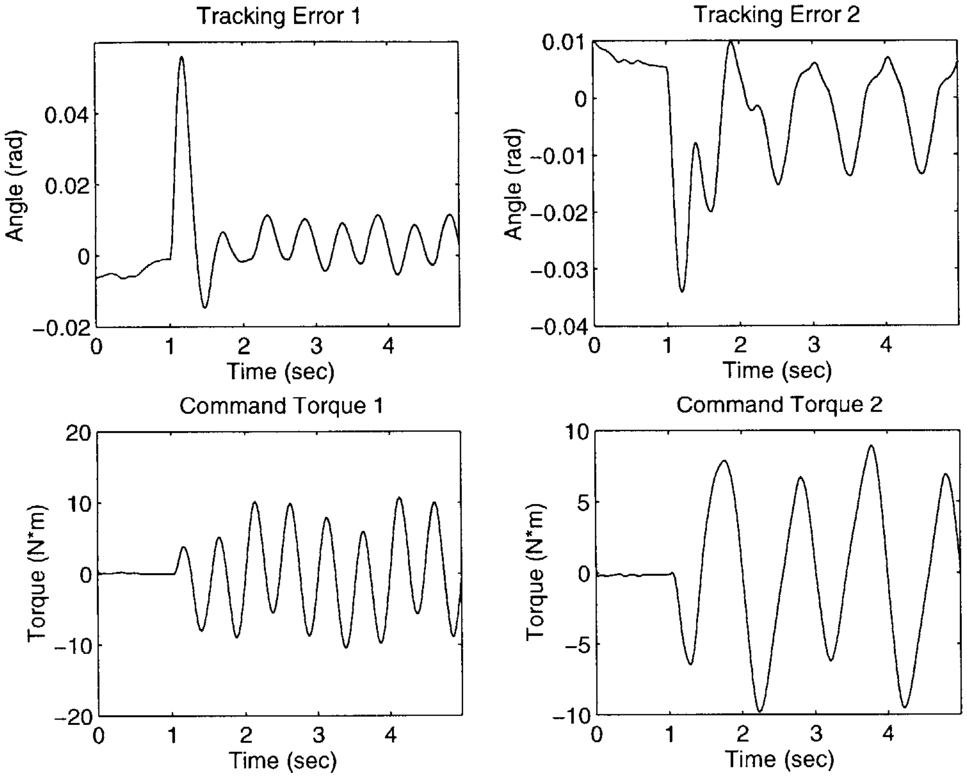

Figure C-4: Tracking errors and Command Torques during a complex trajectory

C.3 Sources of Error

This section is designed to highlight some of the more obvious sources of error involved in the experiments conducted.

Recall the modeling assumptions made in the development of the dynamic equations of the manipulator. One was to neglect the coulomb and viscous friction in the actuators, and the other was to treat the 4-bar-linkage as a simple 2 link mechanism. The first assumption is believed to account for the majority of the tracking error in the experiments. The second assumption is also a source of error, but most likely contributes far less error than neglecting the losses in the system.

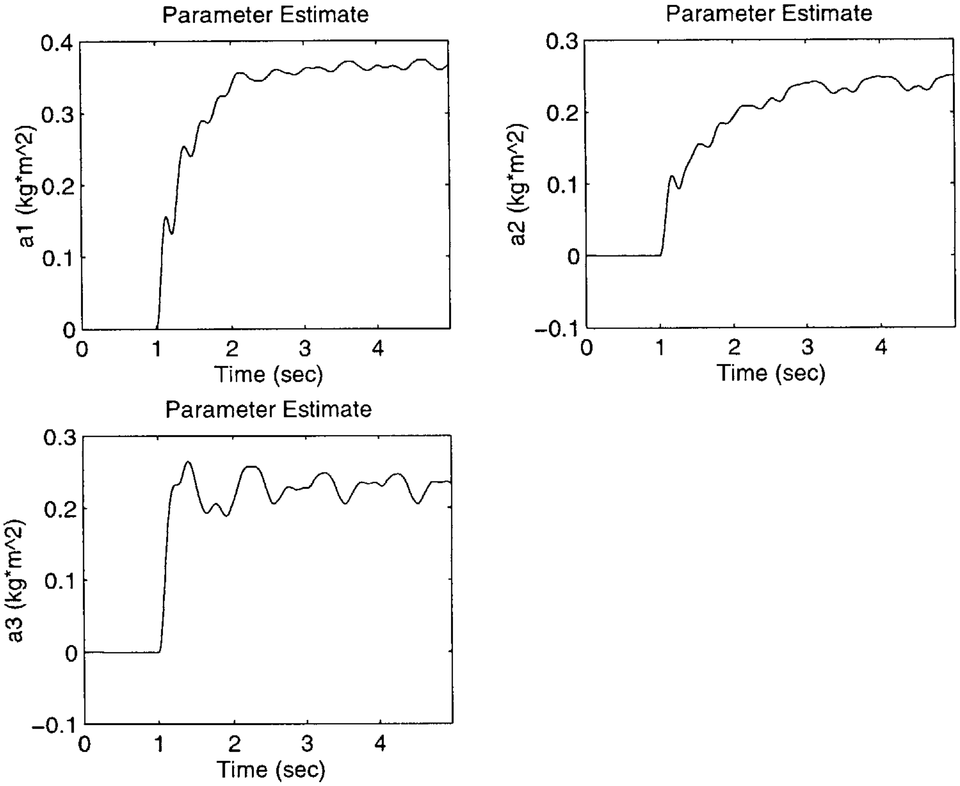

Figure C-5: Parameter Estimates during a complex trajectory. Note, these estimates agree with those given in chapter 3

Another possible source of discrepancy is actuation error. In this system, the actuators have been calibrated, and the torque constants determined experimentally. Therefore, it is assumed that the actuators attribute very little error.

Velocity estimation and sampling rates also attribute error in these experiments. The data is taken at a sampling frequency of 1000 Hz and the velocity is estimated using a first difference. This means that quantization error can become a problem especially at low velocities.

Finally, the PWM amplifiers have a known time delay of 1 msec. This delay can cause problems with tracking trajectories. In fact, previous experiments have shown this delay to be a limiting factor on the maximum gain settings of PD controllers implemented on this manipulator. This may be the case for the gains of the adaptive controller as well.

C.4 Conclusions

An adaptive controller was designed and implemented on a 2 degree of freedom manipulator. This adaptive controller was shown to perform well despite the many sources of non-parametric error. Using a "complex" trajectory, paramater convergence was demonstrated.

Appendix D

Low Sampling Frequency Stability Testing

As discussed in chapter 4, the sampling frequency of 1000 Hz was sufficiently high to render the variable spring aparatus useless in destabilizing the robot. Colgate's research [7] claimed that a spring environment should have destabilized the robot. This can be easily demonstrated by using a much lower sampling frequency and repeating the stability tests described in chapter 4. Three tests were conducted using a sampling frequency of 100 Hz ($\frac{1}{10}$ the previous rate). The tests used the same parameters as test 3 in table 4.1. The first test was conducted with the robot **not** coupled to an environment. The second and third tests were conducted with the robot coupled to the variable spring aparatus using stiffnesses of $1050\frac{N}{m}$ and $3826\frac{N}{m}$ respectively.

The results of the three tests are shown in figures D-1 through D-3. These figures clearly demonstrate the ability of the spring to destabilize the robot. The model data shown in these plots was the best fit achieved using the model for type 1 instability discussed in chapter 4. Also note that these tests did not cover as large a range (of controller damping) as the previous stability tests. This is because larger discrete time steps allow for larger velocity changes between steps. These larger velocity changes resulted in noticable discrete jumps in endpoint position (as felt by the operator) when using large values of controller damping.

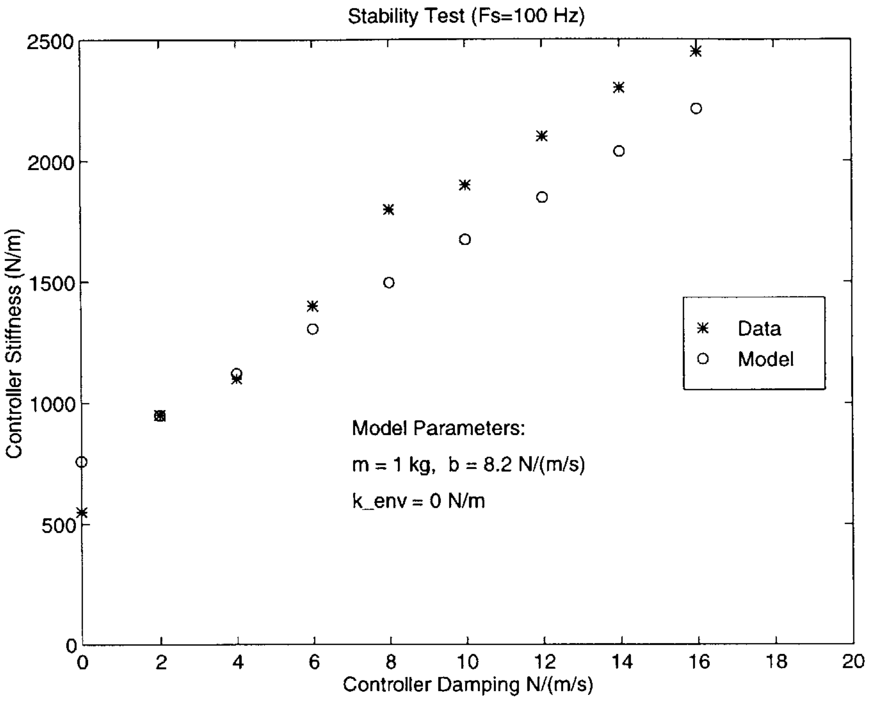

Figure D-1: Uncoupled Stability: Fs=100 Hz

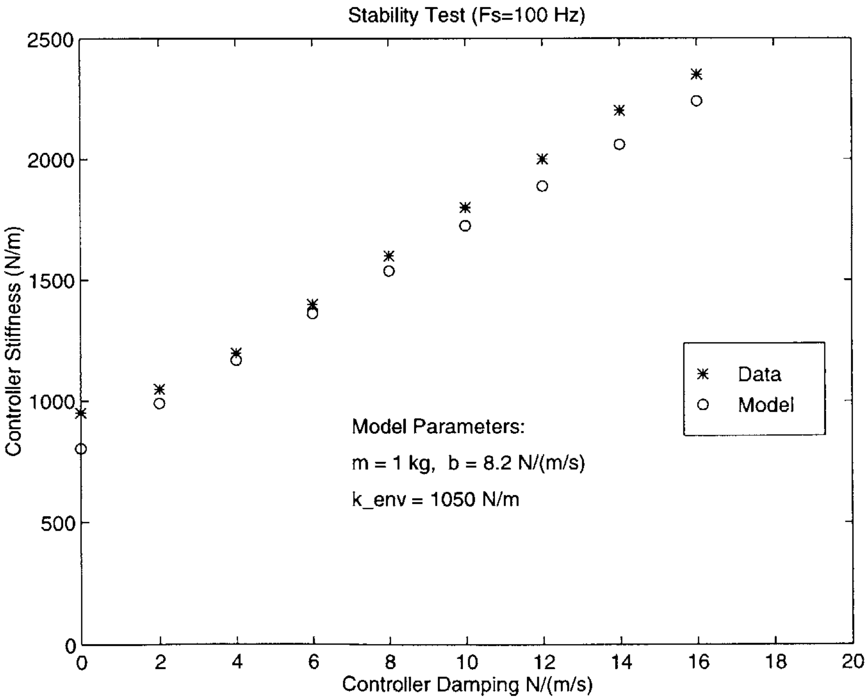

Figure D-2: Coupled Stability: Fs=100 Hz, $k_{env} = 1050\frac{N}{m}$

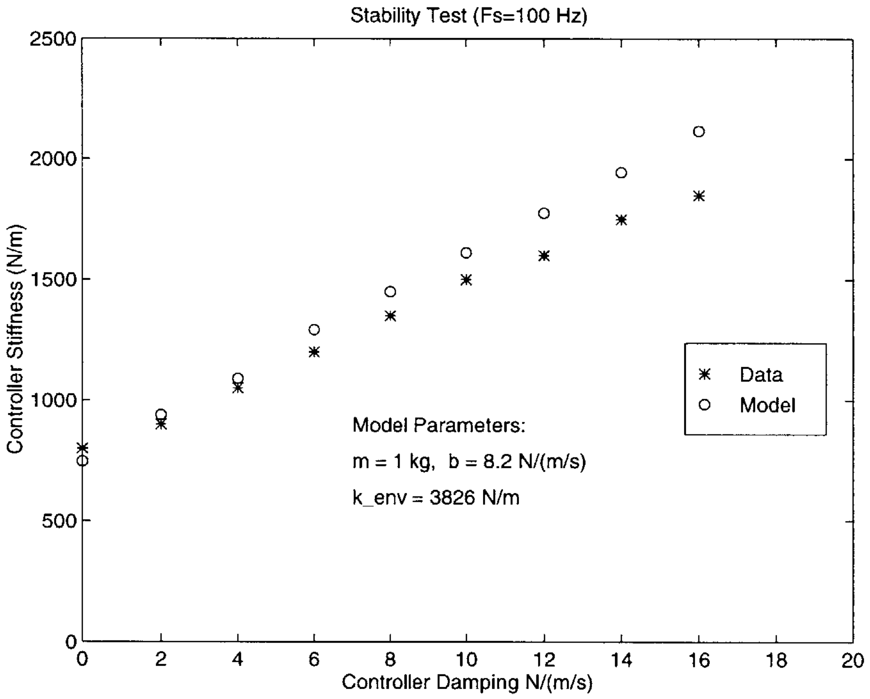

Figure D-3: Coupled Stability: Fs=100 Hz, $k_{env} = 3826\frac{N}{m}$

Bibliography

[1] Debo Adebiyi. Fabrication and characterization of beta-prototype mit manus: an intelligent machine for upper-limb physical therapy. Master's thesis, Massachusetts Institute of Technology, 1998.

[2] National Stroke Association. Brain attack statistics. *http://www.stroke.org*, 1998.

[3] J. Micheal Brown. A theoretical and experimental investigation into the factors affecting the z-width of a haptic display. Master's thesis, Northwestern University, 1995.

[4] Jain Channarong. The design of an intelligent machine for upper-limb physical therapy. Master's thesis, Massachusetts Institute of Technology, 1998.

[5] Jim D. Chapel. Coupled stability characteristics of nearly passive robots. In *IEEE Int. Conf. on Robotics and Automation*, pages 1342–1347, May 1992.

[6] J. Edward Colgate and Neville Hogan. Robust contol of dynamically interacting systems. *International Journal of Control*, 1988.

[7] J. Edward Colgate and Gerd G. Schenkel. Passivity of a class of sampled data systems: Application to haptic interfaces. *Journal of Robotic Systems*, 1997.

[8] James Edward Colgate. *The Control of Dynamically Interacting Systems.* PhD thesis, Massachusetts Institute of Technology, 1988.

[9] Ernest D. Fasse and Neville Hogan. Control of physical contact and dynamic interaction. In *Seventh International Symposium of Robotics Research*, 1995.

[10] Neville Hogan. Impedance control: An approach to manipulation. *Journal of Dynamic Systems, Measurement and Control*, 107:1–24, March 1985.

[11] Neville Hogan. On the stability of manipulators performing contact tasks. *IEEE Journal of Robotics and Automation*, 4(6):677–686, December 1988.

[12] Jin Jiang. Preservations of positive realness under discretizations. *Journal of the Franklin Institute*, 330(4):721–734, 1993.

[13] Hermano Igo Krebs, Neville Hogan, Mindy Aisen, and Bruce T. Volpe. Robot aided neurorehabilitation. *IEEE Transactions on Rehabilitation Engineering*, 6(1):75–87, March 1998.

[14] Dale A. Lawrence. Impedance control stability properties in common implementations. In *IEEE Int. Conf. on Robotics and Automation*, pages 1185–1191, April 1988.

[15] Dale A. Lawrence. Measuring the effects of computation delay in manipulator control architectures. *IEEE Transactions on Robotics and Automation*, 1990.

[16] Dale A. Lawrence and Jim D. Chapel. Qualitative control of manipulator/task interaction. In *IEEE Int. Conf. on Robotics and Automation*, pages 14–25, April 1994.

[17] F. A. Mussa-Ivaldi, N. Hogan, and E. Bizzi. Neural, mechanical, and geometric factors subserving arm posture in humans. *The Journal of Neuroscience*, 5(10):2732–2743, 1985.

[18] Jean-Jacques E. Slotine and Weiping Li. *Applied Nonlinear Control.* Prentice Hall, 1991.

[19] Justin Won. The control of constrained and partially constrained arm movements. Master's thesis, Massachusetts Institute of Technology, 1993.

[20] Justin Won, Brandon Rohrer, and Neville Hogan. The stability and control of physical interactions. *International Journal of Intelligent Mechatronics*, 1998.